Master's thesis

NTNU
Norwegian University of Science and Technology
Faculty of Engineering
Department of Marine Technology

Sofie Helene Råen Wettre

Numerical and Experimental Investigation of a Floating Offshore Wind Turbine Foundation with a Moonpool and Inner and Outer Skirts

Master's thesis in Marine Technology
Supervisor: Trygve Kristiansen
June 2022

NTNU
Norwegian University of
Science and Technology

Sofie Helene Råen Wettre

Numerical and Experimental Investigation of a Floating Offshore Wind Turbine Foundation with a Moonpool and Inner and Outer Skirts

Master's thesis in Marine Technology
Supervisor: Trygve Kristiansen
June 2022

Norwegian University of Science and Technology
Faculty of Engineering
Department of Marine Technology

NTNU
Norwegian University of
Science and Technology

Preface

This thesis is the final contribution to my Master of Science degree in Marine Technology, conducted at the Department of Marin Technology, Norwegian University of Science and Technology (NTNU), in Trondheim, Norway. The work have been carried out during the spring semester of 2022, with a workload corresponding to 30 ECTS.

The motivation for this thesis and the chosen subject have been the growing potential for renewable energy sources, where floating offshore wind has presented itself as key technology when it comes to cleaner energy. The concept investigated is developed by Sevan SSP, and it has been motivational that the work in this master might contribute to their development.

During the autumn of 2021, the concept was investigated as part of the project thesis, and the work have been continued in this thesis. The literature review performed have been included in its full length, and parts of the introduction, theory and numerical and experimental chapter have been further developed.

The theory presented in this master assume a certain knowledge within hydrodynamic aspects, and it is expected that the reader is familiar with the basic hydrodynamic concepts.

Sofie Wettre

Sofie Helene Råen Wettre

Trondheim, 15th June 2022

Acknowledgements

This thesis have been carried out with the supervision of Professor Trygve Kristinsen at the Department of Marine Technology, NTNU. His guidance have been fundamental throughout the semester, and I am grateful for all his advice. His ability to pass on his knowledge of hydrodynamics have been highly appreciated, and it has been very educating working with him.

I would like to thank Sevan for the collaboration, and thank both Lars Mikkel Reiersen and Even Sandøy Nærum for all the information and help they provided.

I would also like to give my appreciation for the lab technicians, Trond Innset, Robert Opland, Terje Rosten Ole Erik Vinje and Torgeir Wahl. Without them and and their ingenuity there would have been no model, and the experiment would not have been as successful without the help I received form them throughout the experiment. They have also been a pleasure to work with, and for all their hard work they deserve a special recognition.

Finally I would like express my gratitude for my family and friends, who have supported me throughout this thesis.

Abstract

Floating offshore wind has the potential to become a major contributor for reaching the goal of net zero-emissions. However, the offshore wind industry still depends on subsides to be viable, and innovative and cost-efficient concepts need to be developed for the industry to be profitable. In this thesis, a concept developed by Sevan SSP for floating offshore wind has been investigated. The floating foundation examined is a circular cylindrical hull with a large central moonpool and inner and outer skirts.

The concept has been investigated through numerical analyses and a model experiment in the Small Towing Tank at NTNU, where the aim was to study the effect of baffles on the rigid body motions. The numerical analyses were executed using WAMIT, where the effects of the skirts and draught were examined, and the results showed that the model was highly sensitive to changes in the draught. Analyses replicating the model experiment were also conducted to capture the tank wall reflections and the added mass effects of the baffles.

Two types of baffles were tested during the model experiment, one solid and one with a perforation ratio of 35 %. The baffles were placed at three different positions inside the moonpool, with N1 being the shallowest position. Both regular and irregular waves were tested for all the configurations, and the results from the experiments have been presented using RAOs.

The experimental results were compared to the numerical, and the same trends could be seen in the RAOs in surge, heave and pitch. The piston and 1^{st} sloshing mode were identified through measurements of the free surface, and the motions were connected to the heave and surge response. The solid plate at N1 caused a shift in the 1^{st} sloshing mode, leading to a reduction in surge motion. Other than that, the neither the solid nor perforated baffle resulted in a significant reduction in the rigid body motions as hoped.

Sammendrag

Flytende havvind har muligheten til å bli stor bidragsyter for å nå målet om et karbonnøytralt samfunn. Så langt er havvind avhengig av subsidier for å være konkurransedyktig, og innovative og kostnadseffektive løsninger trengs for at industrien kan bli lønnsom. I denne avhandlingen har et konsept for flytende havvind, utviklet av Sevan SSP, blitt undersøkt. Det flytende fundamentet består av en sirkulær sylinder med et stort moonpool og indre og ytre skjørt. Konseptet har blitt evaluert gjennom numeriske analyser og modellforsøk i Lilletanken på NTNU, hvor målet har vært å undersøke effekten dempeplater kan ha på bevegelsene i jag, hiv og stamp. De numeriske analysene ble gjennomført i WAMIT, hvor effekten av skjørtene og dypgangen ble undersøkt, og resultatene viste at modellen var svært sensitiv til endringer i dypgangen. Analyser som etterligner modellforsøket ble også gjennomført, hvor effekten av tankveggene og tilleggsmassen fra de solide dempeplatene ble evaluert.

To typer dempeplater ble testet under modellforsøket, en solid og en perforert med en perforeringsgrad på 35 %. Platene ble testet i tre forskjellige posisjoner inni moonpoolen, hvor N1 refererer til den grunneste av dem. Både regulære og irregulære bølger ble kjørt for alle de mulige konfigurasjonene, og resultatene fra forsøkene har blitt presentert gjennom RAO-er.

Resultatene fra eksperiment har blitt sammenlignet med de numeriske, og de samme trendene i RAO-ene for jag, hiv og stamp kunne sees. Både stampbevegelsen (piston mode) og den første sloshing moden ble indentifisert gjennom målinger av den frie overflaten, og bevegelsene har blitt knyttet til bevegelsene i hiv og jag. Den solide dempelaten i N1 førte til et skifte i den første sloshing perioden, som igjen førte til en reduksjon i jag. Borsettfra det, så førte ikke den solide platen eller den perforerte platen til en tydelig reduksjon av jag, hiv eller stamp som ønsket.

NOMENCLATURE

$\phi(x, y, z, t)$	Velocity potential
$\zeta(x, y, t)$	Wave elevation
ζ_a	Wave amplitude
ω	Wave frequency
k	Wave number
ρ	Water density
$\mathbf{M}$	Mass matrix
$\mathbf{A}(\omega)$	Frequency dependent added mass matrix
$\mathbf{B}(\omega)$	Frequency dependent damping matrix
$\mathbf{C}$	Restoring matrix
$\mathbf{F_{exc}}$	Excitation forces matrix
η_j	Motion in mode j
η_{ja}	Motion amplitude in mode j
p_d	Dynamic pressure
F_j^{exc}	Excitation force in mode j
F_j^{rad}	Radiation force in mode j
$H_j(\omega)$	Transfer function (RAO)
$S_\zeta(\omega)$	Wave spectrum
$S_x(\omega)$	Response spectrum
$\lvert H(\omega)\rvert$	Transfer function for irregular waves
F_D	Morison drag force
C_D	Drag coefficient in Morison's equation
u_r	Relative velocity
u_w	Undisturbed incident flow velocity
$B_{kj}^{(1)}$	Linear damping coefficient
$B_{kj}^{(2)}$	Quadratic damping coefficient
$B_{kj}^{(eqv.)}$	Equivalent damping coefficient
$f_{i,j}(x, y)$	3D standing wave profile
$T_{i,j}$	Natural sloshing period
$J_m(k_r r)$	Bessel function
$l_{m,i}$	Nondimensional roots of the Bessel function
x_1	Damping ratio
L^m, L^n	Length scale used in WAMIT
Λ	Froude scale ratio
τ	Perforated ratio of plates
F_{tot}	Total pre-tension force
F_H	Horizontal pre-tension force
k_x	Spring stiffness component in x-direction
k_y	Spring stiffness component in x-direction

ω_0	Undamped natural angular frequency
ϵ	Wave steepness
H	Wave height
Hs	Significant wave height
T	Wave period
Tp	Peak period
λ	Wave length

Table of Contents

CHAPTER 1

Introduction

The global demand for electricity is growing faster than renewable energy sources, resulting in an increase in production of electricity from fossil fuels [1]. Offshore wind has already proven itself as a key technology for reaching net-zero emissions, and it will have a major role in the energy market in the future. Especially floating offshore wind has presented itself as a significant tool in the transition into cleaner energy, with a huge growth potential. DNV estimates that the technology is predicted to grow worldwide, with an increase up to 10 GW in 2030 and 250 GW in 2050, compared to today's production of only 100 MW [2]. Nonetheless, the technologies needed to provide this growth are still under development, substantiating the need to further investigate and develop new concepts.

1.1 Motivation and background

Offshore wind have been estimated by the Global Wind Energy Council to have the biggest growth potential of any of the renewable energy sources, but only 2 % of the the offshore wind the world needs to get by 2050 have been built [3]. Furthermore only a small part of the predicted growth in offshore wind installations will come from floating offshore wind turbines, with only 6.1 % of the new installations in 2030 estimated to be floating [3]. This in spite of that 80 % of the offshore wind potential are located at places with water depths over 60 m, making floating options more feasible than bottom fixed. The floating wind market still depends on subsidies to be viable, furthermore showing the need for new innovative and cost-efficient concepts to be developed.

In addition to the lack of floating offshore wind installations, the offshore wind market is moving out to deeper and harsher water at the same time as the wind turbines are increasing in size. As a results, the floating offshore wind turbines, from now FOWT, have to withstand rougher conditions whilst still be cost-efficient enough to be competitive on the energy market. Nevertheless, more and more companies are rising up to the challenge, and coming up with new designs for FOWTs.

Sevan SSP are one of those companies, who are now adopting their knowledge from the oil industry, to create a concept for floating offshore wind. The Sevan SSP hull has been proven a credible alternative to conventional offshore floating designs [4], and the cylindrical hull, well implemented in the oil industry, has now been modified to suit a wind turbine. The concept can be seen in Fig. 1.1, where the hull now has been adapted with a large central moonpool and inner and outer skirts. The design denoted a small waterplane area cylindrical hull, SWACH, and has shown improved motions compared to traditional hulls. However, the concept is still under development, and the a further investigation into the foundation has been found necessary.

Figure 1.1: The SWACH Wind foundation concept illustrated by Sevan SSP [5]

Moonpools have mostly been used in ships or other types of offshore structures, where the moonpool is only a small part of the hull. In the SWACH wind concept, the moonpool takes up a significant part of the hull, and can contribute to both increases and decreases in the rigid body motions. The liquid resonant motions such as piston- and sloshing-modes can be excited by the waves, resulting in enlarged motions inside the moonpool. However, these liquid motions can introduce cancellation effects, that subsequently might lead to a reduction in the rigid body motions. Nonetheless, all the effects of moonpools are still to be discovered, substantiating the need to further investigate structures with moonpools.

1.2 Literature review

A thorough literature review was performed as a part of the earlier work with the project thesis. The review lists the theory development around moonpools and shows how the effects are still not fully understood. Thus, the whole review from the project thesis have been included here to illustrate the need for further investigations into concepts using moonpools.

Moonpools are vertical openings in offshore structures that provide access to the free surface, and can experience liquid resonance effects. These liquid resonant effects can also be seen in closed tanks and when two vessels are working in close proximity, such that a part of the water is trapped between them and resulting in a moonpool like confinement. When analysing ships with moonpools and vessels operating side by side using potential flow theory, the responses have been highly overpredicted at resonance, causing a lot of frustration in the past decades, as no clear explanation for the overprediction compared to experiments could be found.

A breakthrough was made about 20 years ago, when Molin [6] was able to come up with an approximated theory that provided estimates for the natural modes and frequencies for piston and sloshing resonant effects using a barge with a rectangular moonpool. They were developed with the assumptions that the length of the barge was infinite compared to the length of the moonpool. Thus, the relevance of these formulas should be taken into account when implementing them on other structures with moonpools.

After Molin's breakthrough, several others have studied the effects of moonpools. Rognebakke and Faltinsen [7] investigated the piston mode resonance effects of a 2D moonpool in forced heave oscillations, where they compared linear theory with experimental results. Their findings showed that the linear theory agreed well with the experimental results for the piston mode frequencies, but overpredicts the piston mode amplitudes. Furthermore they compared the piston mode frequencies with Molin's formulas [6], where the disparity was lager for smaller moonpool draughts. However, the reason for the additional damping was only discussed and no clear explanation for the discrepancy between theoretical and experimental results were found.

The question of where the damping came from was later solved by Kristiansen and Faltinsen [8]. They applied a nonlinear numerical wavetank with a vortex tracking

method to the moonpool problem and compared the results to an experiment. The investigation showed that the main reason for the discrepancy for the piston mode amplitude between experimental results and potential flow theory is the additional damping from flow separation at the edges of the moonpool. This was also shown in another study by Kristiansen and Faltinsen [9] where they showed that the damping from flow separation has a much larger effect than the wave radiation damping. Molin [10] studied 2D moonpools with recesses, where he also found that the dominating damping in proximity to the first sloshing mode was due to flow separation, and he discussed that the radiation damping was more prominent around the first piston mode compared to the first sloshing mode.

The number of studies on the effects of sloshing in tanks and in moonpools have increased over the past years, but the majority of the studies on moonpools have focused on 2D structures that are either fixed or forced to oscillate. The coupling effects of moonpools in freely floating structures have also been investigated, but not to the same extent. Fredrisken et al. [11] investigate the wave-induced response of a 2D body with a moonpool. They showed that the moonpool behaviour has an effect on the rigid body motions, and that around resonance the response is clearly amplified compared to the incoming wave amplitude. They also showed that the damping from flow separation contributes to reducing the response compared to potential flow theory. Ravinthrakumar et al. [12] investigated the coupled interaction between a 3D vessel and different moonpool sizes, where the second and third one will be commented here. They compared the RAOs for the different configurations, and found that the hydrodynamic coupling between the vessel and the moonpool causes a shift in the natural piston mode period. They also conclude that the dominant damping comes from flow separation, and that the wave radiation damping is in general small for the piston, and first and second sloshing modes. For the case with the moonpool length being 50 % of the overall length, the rigid body motions are found to be highly affected by the moonpool responses. In addition, they found that for structures where the moonpool dimensions are large enough relative to the structure, the nonlinear higher modes can be excited by the irregular waves and that such effects have to be accounted for.

Reiersen et al.[13] investigated moonpools as a pitch motion reducing device, and found that the cancellation effect can contribute to smaller pitch motions. However, the moonpools also introduce a drawback to this cancellation by increasing the response in periods close the the cancellation period. Another aspect of moonpools is that they can have a large impact the decay of motions. Reiersen et al.[13] also

performed decay tests in heave and pitch to investigate this effect and found that due to piston-mode resonance the decay was not monotone. As a result, performing decay tests to evaluate the natural periods of structures with moonpools may not be possible.

Molin have later developed the formulas derived in [6], and Molin et al. [14] investigated the effect of bodies with finite depth and finite length and width, and compared the new estimates for the piston mode periods to results from WAMIT. In general, the newer model was found to give correct estimates for the first piston and sloshing modes for finite water depth, and adequate results for the cases with finite outer dimensions, as the frequencies were slightly overestimated. One of the bodies studied was circular barge with a circular moonpool, and Fig. 1.2 shows how the natural frequencies for the first piston mode varies with the water depth c, where it converges towards the results from the first model for increasing water depth.

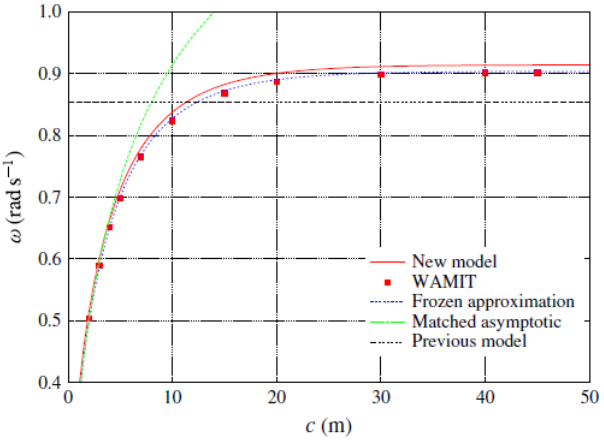

Figure 1.2: Circular moonpool. Natural frequency of the piston mode for a = 10 m, d = 5 m, b = 30 m, and varying c (water depth) [14]. a and d gives the dimentions of the circular barge

The effect of sloshing and piston modes in tanks have also been studied by several, and Faltinsen and Timokha [15] derived the natural sloshing modes and frequencies for various types of closed tanks. The results correlated nicely with the findings by Molin [6]. Baffles have been used to reduce the sloshing in tanks containing liquid, and have been found practical in several studies. The effect of installing baffles in partly filled cylindrical tanks have been investigated by Wang et al. [16] where they tried various types of baffles at different water levels. Moreau et al. [17] investigated the installation of baffles in an upright bottomless vertical cylinder floating in waves. The work is highly relevant for the concept investigated in this project, and a more through elaboration of the study can be seen in Sec. 1.2.1.

Moonpools implemented in FOWTs are not well known, and to the author's knowledge there only exists two concepts so far; The Sevan SWACH Wind concept to be investigated in this project, and BW Ideol. The BW Ideol is a barge formed structure with a central moonpool, and two demonstration concepts have been installed, with one in France and one in Japan. Several studies have been conducted in the barge foundation [18, 19, 20, 21], and compared to a conventional barge foundation the implementation of a moonpool have shown to have several advantages, such as improving the seakeeping performance and reducing the construction costs. A cylindrical dock with a moonpool have also been investigated for a spar wind turbine installation by Jing et al. [22], where the piston and sloshing effects were shortly discussed.

1.2.1 Work by Moreau et al.

This section recites and show some of the findings done by Moreau et al. [17]. All the figures and equations presented here are taken from *An upright bottomless vertical cylinder with baffles floating in waves* [17].

Moreau et al. investigated the rigid body motions of a freely floating circular cylinder with a moonpool, an outer skirt, and the effect of implementing baffles inside the moonpool [17]. The structure is similar to the one investigated in this thesis, and the result have influenced and inspired this thesis, as the effect of installing baffles were found to have a significant impact on the motions. During the study both a model test and a semi-analytical approach was performed to investigate the response.

Moreau showed that baffles introduce two main effects; additional damping and a shift in the natural sloshing frequencies. They implemented the fact that the eigenfunctions are assumed unchanged by the baffles, to estimate the shifted natural sloshing periods.

Moreau et al. [17] showed that when the perforated ratio increases, the added mass of the baffle tends to 0, and for increasing submergence the the fluid velocity decreases. The damping ratios for baffles with different perforated ratios were estimated using the energy dissipation, and through an iterative scheme the damping ratio ξ_1 was computed. It was found to reach "local" maximum at the coupled sloshing resonance where, $|\beta_1|$ is also maximum [17]. The damping ratio as a function of nondimensional frequency of the incident waves are given in Fig. 1.3, and it can be seen that the damping decreases with perforated ratio and level of submergence.

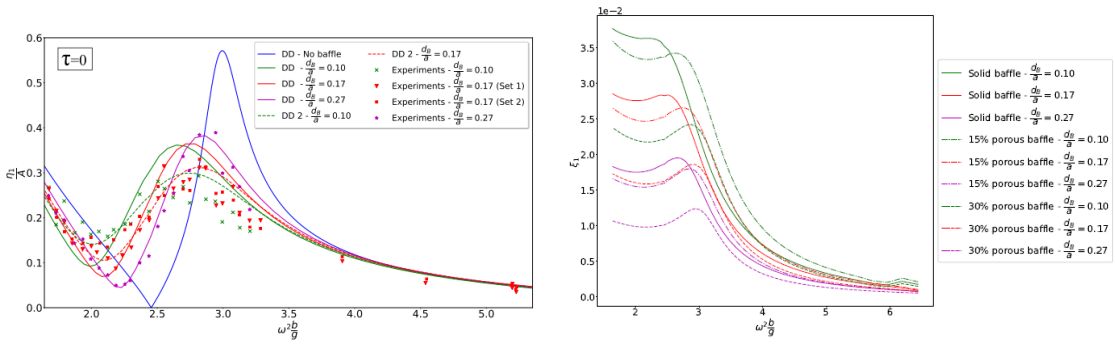

(a) Nondimensional surge η_1 (b) Linear equivalent damping ratio ξ_1

Figure 1.3: Surge RAO for different baffle configurations and linear equivalent damping ratio from [17] by Moreau et al. Given as a function of the nondimensional frequency and with a constant wave steepness $\epsilon = 1/60$.

In Fig. 1.3 (a) the surge RAO from [17] is shown, where the different baffles can be seen to effect the rigid body motions. The baffle showing the largest effect on the surge motion can also be recognised as the baffle with the best damping efficiency on the sloshing waves. These results have been a huge inspiration for the work done in this thesis, and additional results will also be used for comparison later.

1.3 Aims and objectives

The aim of this master thesis have been to investigate a simplified version of the Sevan SWACH floating offshore wind foundation, and how implementing baffles might affect the rigid body motions in surge, heave and pitch, with extra focus on the pitch motion. In addition, the effects of sloshing on the rigid body motions have been of interest. The preliminary examinations conducted by Sevan have shown undesired pitch motions for periods around 12 - 14 s, and a reduction of these would help contribute to a further development of this concept.

The objectives and scope of work have been as follows:

1. Obtain a better understanding of moonpools and the effect they can have on rigid body motions
2. Numerically investigate the effect of the skirts and draught of the model to acquire a better understanding of the concept and how it behaves
3. Preparations and planning of an experiment with focus on the effects of baffles
4. Conduct regular and irregular wave tests of the model without baffles, and for the two types of baffles tested
5. Process the experimental results to obtain RAOs of the rigid body motions and surface elevations
6. Discuss the effect of baffles based on the numerical and experimental results

1.4 Structure of master thesis

The master thesis have the following structure.

In the introduction the motivation and background for the thesis and concept are presented, and a literature review reciting some important aspects of moonpool theory is included.

In Ch. 2 hydrodynamic theory from know authors have been recited, and the necessary quantities have been established. Through Ch. 3 the numerical solver used for this thesis have been presented, including all the aspects from meshing the model to the numerical analyses conducted. Ch. 4 present the experiment and the set-up, in addition to a short discussion of the possible error sources and the post-processing methods.

In Ch. 5 the results from the numerical parameter studies have been presented and discussed, and in Ch. 6 experimental results are given and discussed. Lastly, the conclusion and further work are presented in Ch. 7.

CHAPTER 2

Theory

In this chapter already established theory from several well known authors and books are recited, and parts of this section have been taken from the project thesis. The concepts concisely described here are included to provide a short summary of some of the quantities necessary for discussing the numerical and experimental results. However, the reader should be familiar with basic hydrodynamic theory, and some of the concepts are only briefly mentioned here to provide the framework.

2.1 Potential flow theory

The numerical solver used for this thesis is WAMIT, and a more thorough introduction to the solver is given in Ch. 3. As many other numerical solver it uses potential flow theory to procure a solution for the hydrodynamic problems. Thus, as short presentation of the theory implemented have been included to better understand the possibilities and limitations of the solver.

Potential flow theory can be used to describe the interaction between bodies and surface waves. The theory implements several simplifications to describe the environment and following responses, and the fluid is assumed inviscid and incompressible, and the flow irrotational. The assumptions makes it possible to solve the linearised boundary value problem to obtain the first order potential flow theory solution. The velocity potential (ϕ) is used to express the linear wave solution for a wave propagating in positive x-direction, and in finite water depth the following expressions are obtained. Eq. 2.3 gives the finite water depth linear dispersion relation, which is of high relevance for the linear wave description of the waves in the experiment.

$$\phi(x,y,z,t) = \frac{g\zeta_a}{\omega}\frac{\cosh(k(z+h))}{\cosh(kh)}\cos(\omega t - kx) \tag{2.1}$$

$$\zeta(x,y,t) = \zeta_a \sin(\omega t - kx) \tag{2.2}$$

$$\omega^2 = gk\tanh(kh) \tag{2.3}$$

The velocity potential can be used to find the response of a body in linear waves. Another consequence of the linearity is that the frequency domain approach can be used, since the velocity potentials, pressure and loads all oscillate with frequency ω. Thus, the steady-state response for each frequency can be solved for to find the response amplitude operators for each rigid body mode.

2.2 Rigid body motions

The rigid body motions considered in this thesis have been surge, heave and pitch, as the structure is symmetric about the xz- and yz-plane.

The rigid body motions of a body floating freely in waves are found by solving the matrix-vector system given in Eq. (2.4).

$$(\mathbf{M} + \mathbf{A}(\omega))\ddot{\eta} + \mathbf{B}(\omega)\dot{\eta} + \mathbf{C}\eta = \mathbf{F_{exc}} \tag{2.4}$$

A rigid body in waves seldom respond one degree of freedom alone and the motions will generally be coupled in two or more rigid body modes. The inertial coupling is included in the mass-matrix $\mathbf{M}$ for the DOFs where $j \neq k$. When the body is symmetric by one or two symmetry planes the mass matrix can be simplified, and for the symmetrical SWACH foundation, the mass matrix is reduced to the one shown in Eq. 2.5.

$$\mathbf{M} = \begin{pmatrix} m & 0 & 0 & 0 & mz_g & 0 \\ 0 & m & 0 & -mz_g & 0 & 0 \\ 0 & 0 & m & 0 & 0 & 0 \\ 0 & -mz_g & 0 & I_{44} & 0 & 0 \\ mz_g & 0 & 0 & 0 & I_{55} & 0 \\ 0 & 0 & 0 & 0 & 0 & I_{66} \end{pmatrix} \tag{2.5}$$

The symmetry of the body will also affect the added mass, damping, and restoring terms in Eq. (2.4), and the terms are found by looking at the linear hydrodynamic loads.

2.3 Linear hydrodynamic loads

The linear wave-induced motions and loads are found by solving the two sub-problems; the radiation problem and the diffraction problem. Through the diffraction problem, the wave excitation loads F_j^{exc} consisting of the Froude-Kriloff and diffraction forces and moments, can be found for each body mode j by solving Eq. 2.6, with ϕ_0 and ϕ_7 being the velocity potentials for the diffraction problem.

$$F_j^{exc} = \int_{S_{0B}} p_d n_j dS = \underbrace{\rho \int_{S_{0B}} \frac{\partial \phi_0}{\partial t} n_j dS}_{Froude-Kriloff} + \underbrace{\rho \int_{S_{0B}} \frac{\partial \phi_7}{\partial t} n_j dS}_{Diffraction} \tag{2.6}$$

In the radiation problem, the hydrodynamic loads are found, and expressions for the added mass (A_{kj}), damping (B_{kj}) and restoring (C_{kj}) terms are obtained. The added mass and damping loads for a body mode j are defined by Eq. 2.7, providing the loads for mode k.

$$F_k = -A_{kj} \frac{d^2 \eta_j}{dt^2} - B_{kj} \frac{d\eta_j}{dt} \tag{2.7}$$

A_{kj} and B_{kj} are frequency dependent, and will also be affect by the water depth.

For a structure with six DOFs there are a total of 36 added mass and damping coefficients. However, for a symmetrical body, without forward speed or current, it can be shown that $A_{kj} = A_{jk}$ and $B_{kj} = B_{jk}$. The non-zero cross-terms are a result of coupling, and for a structure with a moonpool the coupling of surge and pitch might cause significant coupled added mass terms $A_{15} = A_{51}$.

For the body investigated in this project the non-linear damping will be significant due to the skirt, moonpool and baffles. This term have not been included in Eq. (2.4), and it will be introduced later.

The linear restoring coefficients are not frequency dependent, and are a result of change in the hydrostatic pressure and change in displaced volume as the body

is taken out of its equilibrium floating position. Without mooring, several of the terms in terms **C** will become non-zero as the motions do not create any variations in the displaced volume. The structure investigated here will be moored during the experiment, and the additional restoring the mooring lines introduces have to be included in the numerical analyses to best capture the same response.

$$F_k = -C_{kj}\eta_j \tag{2.8}$$

2.4 Regular waves

Regular waves are known as waves with constant amplitude, period and wave length, and can be characterised by the wave period and wave steepness $\epsilon = H/\lambda$. The wave length λ is related to the wave frequency through the wave number k, by $k = 2\pi/\lambda$, where k is found through the dispersion relation, shown for a finite water depth in Sec. 2.1. The response from regular waves are often expressed by a response amplitude operator, from now RAO.

2.4.1 RAO - Response Amplitude Operator

The RAO gives the ratio between the response and the incident waves, and is commonly found from using the frequency domain and complex notations. The RAO, or often also called transfer function, is given by Eq. 2.9.

$$H_j(\omega) = \frac{\eta_{ja}}{\zeta_a} \tag{2.9}$$

η_{ja} is the response in mode j and the incident wave amplitude is give by ζ_a. For the rotational modes, such as pitch, the measured motions also have to be divided by the wave number k, resulting in the expression

$$H_j(\omega) = \frac{\eta_{ja}}{\zeta_a k} \tag{2.10}$$

By using heave as an example and the rearranging the equation of motion, the RAO for heave can be expressed as demonstrated in Eq. 2.11

$$\frac{\eta_{3a}}{\zeta_a} = \frac{f_{3a}}{-\omega^2(M + A_{33}) + i\omega B_{33} + C_{33}} \tag{2.11}$$

2.4.2 Finite water depth

The shift from deep water to finite or shallow water depends on the ratio between the wave length λ and the water depth. Several definitions of this shift can be found, but in this thesis the definition used is taken from the *Marine Dynamics compendium* [23]. For $h/\lambda \leq 0.5$, the water condition becomes finite, and for the experiment conducted this shift occurs for wave periods larger than 0.1 s with a water depth of 0.8 m.

2.5 Irregular waves

The waves seen on the ocean surface is not realistically described by regular waves. Nonetheless, the linearity linearity of regular wave theory makes is possible to express irregular waves as a sum of regular waves with different wave lengths, amplitudes and propagation direction. Eq. (2.12) gives the surface elevation for a two-dimensional case with long-crested waves coming from the same direction.

$$\zeta(x,t) = \sum_{n=1}^{N} \zeta_{An} \cos(\omega_n t - k_n x + \epsilon_n) \tag{2.12}$$

ϵ_n is a random phase, k_n the wave number and A_n is the amplitude. Irregular wave theory is based on the theory of a random process, with ϵ_n at t= 0 considered as a stochastic variable. As a result the total amount of energy within a sea stet can be given as a sum of N wave components (Eq. 2.13).

$$\frac{E}{\rho g} = \sum_{n=1}^{N} \frac{1}{2} \zeta_{An}^2(\omega_n) \tag{2.13}$$

The total energy within a sea state is commonly described by a wave spectrum $S(\omega_n)$, leading to the relation given in Eq. (2.14) [23].

$$\frac{E}{\rho g} = \frac{1}{2} \sum \zeta_{An}^2 = \int_0^\infty S(\omega) d\omega \tag{2.14}$$

where the wave amplitude can then be expressed by Eq. (2.15),

$$\zeta_{An}^2 = \sqrt{2S(\omega_n)\Delta\omega} \tag{2.15}$$

By inserting the term for the wave amplitude into Eq. 2.12, the expression for the surface elevation at a given time t becomes

$$\zeta(x,t) = \sum_{n=1}^{N} \sqrt{2S(\omega_n)\Delta\omega}\cos(\omega_n t - k_n x + \epsilon_n) \tag{2.16}$$

Through the the wave spectrum all the necessary statistical properties of the wave elevation $\zeta(t)$ can be expressed. Several types of standardised wave spectrum exists, and in this thesis the JONSWAP spectrum have been used to create the irregular sea states.

2.5.1 Response spectrum

The response spectrum can be obtained from a given wave spectrum by using a transfer function, or RAO. The transfer function connects the wave elevation to the response, where the wave elevation for one component coming from x = 0 can be expressed as $\zeta_n(t) = \zeta_{An}\cos(\omega_n t + \epsilon_n)$ using Eq. 2.12. The response amplitude from a given wave amplitude can be expressed by the transfer function as shown in Eq. 2.17.

$$x_{An}(\omega_i) = |H_x(\omega_n)|\zeta_{An}(\omega_n) \tag{2.17}$$

All the terms in the above equation are real and positive, and thus by rearranging Eq. 2.17, and using the relation between the wave amplitude and the wave spectrum shown in Eq. 2.15, a general relationship between the wave spectrum and the response spectrum can be obtained, as the first part of Eq. 2.18 shows.

$$S_x(\omega) = H(\omega)^2 \cdot S_\zeta(\omega) \qquad \longrightarrow \qquad |H(\omega)| = \left(\frac{S_x(\omega)}{S_\zeta(\omega)}\right)^{\frac{1}{2}} \tag{2.18}$$

The response and wave spectrum from measured time-series can be obtained by using spectral analysis, where the Fast Fourier Transform (FFT) is commonly used.

Thus, the transfer function, or RAO, shown in the the second part of Eq. 2.18, can be acquired to give the response per wave amplitude for an irregular sea state.

2.5.2 JONSWAP Spectrum

The JONSWAP spectrum is a result of a multinational measuring project, which was executed in the south-east part of the North Sea between 1968 and 1969. The "Joint North Sea Wave Project", i.e JONSWAP, is developed based on the other well-known Pierson-Moskowitz spectrum, and is characterised by a rather sharp peak. The spectrum is constructed by introducing the peak frequency ω_p into the PM-spectrum, and thus removing the relation to the wind speed.

The following relation $\omega_p = 0.87g/V$ between the peak frequency and the wind speed inserted into the PM spectrum, and by multiplying the spectrum with a factor and introducing the peakedness parameter the JONSWAP spectrum can be expressed by the frequency f as shown in Eq. 2.19.

$$S(f) = \alpha g^2 (2\pi)^{-4} f^{-5} exp\left[-\frac{5}{4}\left(T_p f\right)^{-4}\right] \gamma^{exp\left[-\frac{(f/f_p-1)^2}{2\sigma^2}\right]} \tag{2.19}$$

The spectrum is deemed as a fairly good model for wind generated seas within the JONSWAP region, which is limited by

$$3.6\sqrt{H_{m0}} < T_P > 5\sqrt{H_{m0}}$$

where $H_{m0} = 4\sqrt{m_0}$.

The limits in combination with Eq. 2.19 can then be used generate an irregular sea state, for a given significant wave height Hs and a given peak period Tp.

2.6 Second order effects

In linear potential flow theory the higher order effects are not regarded, and only the terms proportional to $\epsilon = k\zeta_a$ are included. However, the higher order terms can have a significant impact on the loads and motions, and should be taken into account.

2.6.1 Viscous loads

In potential flow theory the loads from viscous effects are not accounted for as the fluid is assumed inviscid and the flow irrotational. In reality viscous loads contribute to the added mass, damping and excitation loads, and can have a significant effect on the response. When the viscous loads are small compared to the potential flow loads, they can be neglected, and for many marine structures it is enough to only account for the viscous damping alone.

For the SWCAH Wind concept, the viscous loads are significant, and the viscous added mass and excitation loads have to be accounted for. The theory around these effects are meager, and a reliable way to account for these effects have yet to be found. However, one way is to include a Morison type quadratic drag load term given in Eq. (2.20).

$$F_D = 0.5\rho C_D D u_r |u_r| \tag{2.20}$$

The drag coefficient C_D, diameter D and relative velocity u_r are well known for 2D circular cylinders. However, for other geometries the quantities are not as defined, and for a cylindrical structure with skirts, the diameter to use and where the drag coefficient and relative velocity shall be defined is not easy to determine. Sevan have tried using Morison types loads around the circumference to model the quadratic damping, added mass and excitation loads, which might be a good approximation.

Nonetheless, there are complications with defining the relative motion of the body as it is given by the incident wave particle velocity and the velocity of the coupled motions. By using the heave and pitch coupling, the relative motion will be given by the incident wave particle velocity, heave velocity and coupled pitch velocity. The relative velocity can be expressed as the undisturbed incident flow velocity at the

tip of the skirt minus the velocities of the body motions, resulting in Eq. (2.21). b is distance the load is taken over.

$$u_r = u_w - \dot{\eta}_3 + \dot{\eta}_5 b \tag{2.21}$$

The expression for the relative velocity can be inserted in the Morsion load equation, yielding Eq. (2.22), where

$$F_{D3} = 0.5\rho C_D D(u_w - \dot{\eta}_3 + \dot{\eta}_5 b)|(u_w - \dot{\eta}_3 + \dot{\eta}_5 b)| \tag{2.22}$$

The Morison loads in heave will have a non-trivial coupling between heave and pitch and the wave particle velocity. Thus, the excitation loads depends on u_w and the quadratic damping on the body motions. In addition, there will be viscous effects from pitch loads, which also have to be addressed. As demonstrated, the viscous loads are not easy to calculate and are difficult to model in numerical analyses. The struggles with including viscous loads illustrate the need for experiments, where the viscous effects can be attempted to be estimated, or CFD analyses.

2.6.2 Viscous damping

For the SEVAN wind concept with both inner and outer skirts, and additional baffles installed the viscous damping from flow separation will be significant. The quadratic damping term can be added to the potential flow loads to reduce the over prediction of the motions around resonance. The "new" equation of motion can then be written as shown in Eq. (2.23).

$$\sum_{j=1}^{6}[(M_{kj} + A_{kj}\ddot{\eta}_j + B_{kj}^{(1)}\dot{\eta}_j + B_{kj}^{(2)}\dot{\eta}_j|\dot{\eta}_j| + C_{kj}\eta] = F_j e^{i\omega t} \tag{2.23}$$

$B_{kj}^{(2)}$ is denoted the quadratic damping coefficient, and have to be found using CFD analyses. Another approach is to linearise the term by using equivalent linearisation, where $B_{kj}^{(1)}$ and $B_{kj}(2)$ are expressed as one equivalent term $B_{kj}^{(eqv.)}$, which can be expressed as:

$$B_{kj}^{(eqv.)} = b_1 + b_2|\dot{\eta}| \tag{2.24}$$

The linear and quadratic damping coefficients can be estimated by a PQ-analyses on a decay test. The damping will cause the energy in the system to reduce over time, and using that he mean amplitude for a given cycle is $\bar{x}_i = (x_i + x_{i+1})/2$, the following equations can be derived

$$\frac{(x_i - x_{i+1})}{\bar{x}_i} = \frac{\pi\omega_d}{k} b_1 + \frac{8\omega_d^2 \bar{x}_i}{3k} b_2 \tag{2.25}$$

$$\frac{(x_i - x_{i+1})}{\bar{x}_i} = P + Q\bar{x}_i \tag{2.26}$$

However, not all structures can achieve a clear decay due to the body geometry, making it difficult to estimate the quadratic damping from a PQ-analyses. Moonpools are one type of such geometries that might influence the decay tests, and for the SEVAN concept this procedure is expected to be strenuous. Another approach to estimate the quadratic damping is through the energy dissipation, which Moreau et al. have done [17].

2.7 Moonpools

An introduction to moonpools was given in Sec. 1, and through the litterateur review in 1.2 it was established that moonpools can have a significant effect on the rigid-body motions. Natural resonant liquid motions, know as sloshing and piston modes, can be excited by the external waves, and through several studies estimates for these modes and periods have been found, see [6, 10, 14, 15]. Nevertheless, they all have their limitations, and for a structure with a large moonpool relative to the body, the estimates will not give accurate results for the sloshing and piston modes. However, they can be implemented to obtain an idea of where the resonant motions might occur.

One way of attaining the first piston mode is through evaluation of the added mass coefficient in heave from numerical analyses. When the first piston mode occurs, the added mass coefficient will show a clear minimum in the graph. This can be seen in the example provided in Fig. 2.1, which is a result developed for a structure with two concentric moonpools [24]. *a33* is the added mass for the entire structure and *a77* is for the inner moonpool alone. In Fig. 2.1 two resonant piston modes can be seen.

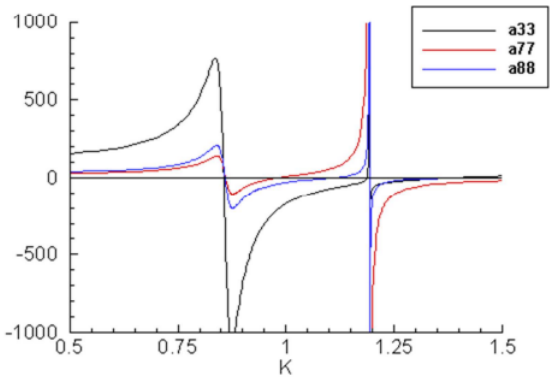

Figure 2.1: Added masse coefficient for a structure with two concentric moonpools. a33 is the added mass coeff. for the whole structure, and a77 for the inner moonpool alone [24]

2.8 Sloshing

Sloshing can be defined as a resonant excitation of a liquid with a free surface confined in a tank or by another form of walls. It can exist in various forms or modes, where the confinement of the liquid defines the sloshing modes natural frequencies. The sloshing modes can be described by standing waves, and are categorised as symmetric or antisymmetric. For a 2D rectangular tank the fist sloshing mode corresponds to an antisymmetric standing wave, where the wave length is twice the tank length. Faltinsen and Timokha [15] illustrated the first six natural sloshing modes for a 2D-tank, as shown inn Fig. 2.2 where $i = 1$ corresponds to the first mode, and it can be seen that half a wave fits across the 2D-tank.

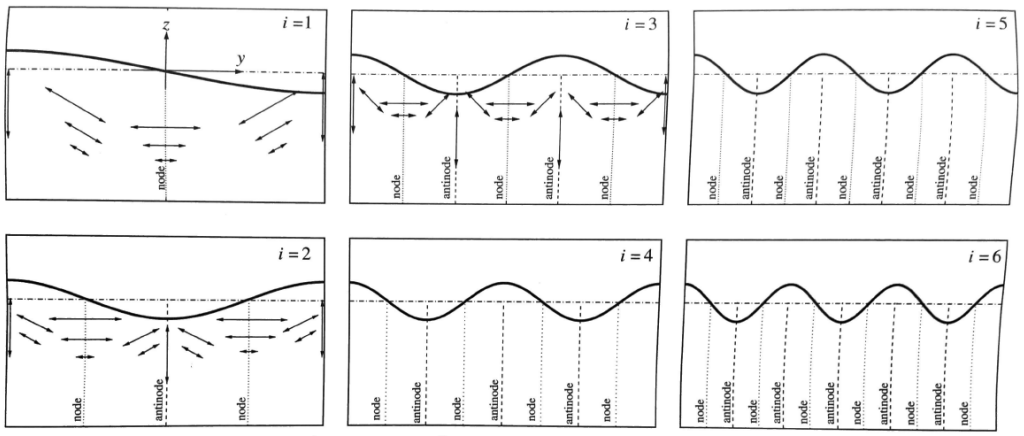

Figure 2.2: Standing waves corresponding to the natural sloshing modes for a 2D rectangular tank [15], where i equals odd numbers provides antisymmetric modes and i equals even numbers provide the symmetric ones.

The first sloshing mode is also the one of highest relevance, as the sloshing force decreases with increasing mode number. In addition, the first sloshing mode can excite higher non-linear sloshing modes, known as secondary resonance, showing its importance. For a circular moonpool the theory is not as defined as for a 2D-tank, nonetheless the theory can be used to find expression for a 3D cydlindrical tank.

The solution for a 3D cylindrical tank is found by firstly solving for a 3D rectangular tank and then implement cylindrical coordinates. The standing wave pattern for a 3D cylindrical tank can then be expressed as shown below:

$$f_{m,i}(r,\theta) = J_m(l_{m,i}\frac{r}{R_0}) \cdot \begin{cases} \cos(m\Theta) \\ \sin(m\Theta) \end{cases}$$

Applying the expression for the standing wave patters, the natural sloshing periods can be expressed by Eq. 2.27.

$$T_{m,i} = \frac{2\pi}{\sqrt{gl_{m,i}\tanh(l_{m,i}h/R_0)/R_0}} \tag{2.27}$$

To obtain the periods from Eq. (2.27), the Bessel function $R(r) = J_m(k_r r)$ have to be solved first to obtain the nondimensional roots $l_{m,i}$, by using $J'_m(l_{m,i}) = 0$. The first sloshing mode for a circular tank can then be expressed as shown below:

$$T_{1,1} = \frac{2\pi}{\sqrt{gl_{1,1}\tanh(l_{1,1}h/R_0)/R_0}} \tag{2.28}$$

To obtain an estimate of the first natural sloshing period $t_{1,1}$, Fig. 2.3 from the book *Sloshing* [15] can be used, when the solution to the Bessel function have not been found. R_0 wil then be the radius of the moonpool.

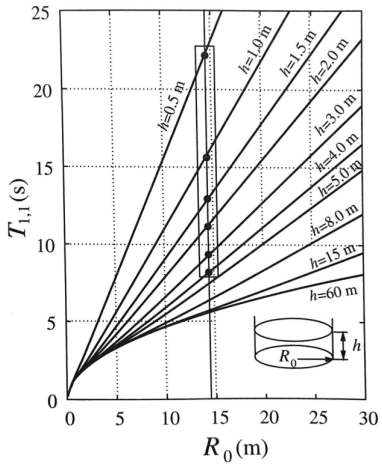

Figure 2.3: The first natural sloshing period as a function of radius R_0, for a cylindrical tank with varying heights h [15].

A nonlinear sloshing mode may occur in both a rectangular and a cylindrical 3D tank, known as a three dimensional swirling wave. Swirling is defined as a progressive wave motion in the angular direction, and occurs when two antisymmetric standing waves are combined into one swirling motion [15]. However, the swirling motion is difficult to capture, as two standing waves can occur without initiating swirling whilst visually look like swirling. If swirling actually do occur it can cause significant loads inside the moonpool and on the structure.

It should be noted that these formulas have been derived for closed tanks, with no mass flux, and the periods derived from these expression should only be used as estimates.

2.8.1 Piston mode

The liquid resonant motion known as piston mode is often referred to as the zeroth sloshing mode. The name comes from the motion of the liquid which nearly moves in one dimension as a rigid body [15], up and down like a piston, and the mode is a result of non-zero net mass flux. Fig. 2.4 shows and example of the piston motion inside a moonpool in a cylindrical dock given in [22].

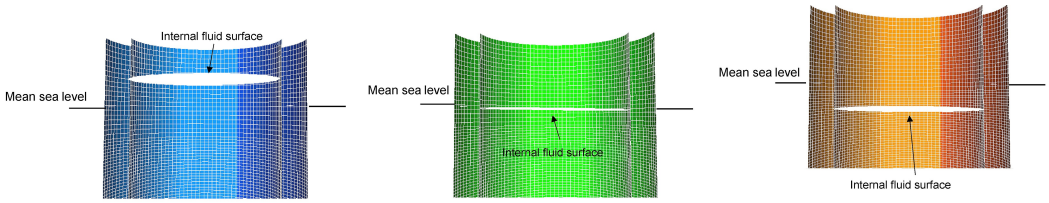

(a) Time instant I during a piston-mode cycle

(b) Time instant II during a piston-mode cycle

(c) Time instant III during a a piston-mode cycle

Figure 2.4: Visualisation of the piston mode in a moonpool of a cylindrical floating dock [22]

As mentioned in 2.7, the first piston mode period might not be calculated correctly by the expression given in Eq. (2.27), and should be evaluated by looking at the added mass coefficients from numerical analyses.

CHAPTER 3

Numerical analyses

In this section a description of the numerical analyses conducted in this thesis are given. WAMIT was chosen as the numerical solver to evaluate the SWACH wind concept, and version 7.4 was used for the analyses. The various parameter analyses conducted were aimed to investigate the different aspects of the floating foundation, and the numerical replicas of the experiments should hopefully coincide with the experimental results.

3.1 WAMIT

WAMIT is a panel code program that solves the diffraction and radiation problem in potential flow, and has been developed to solve the linear interaction problems between surface waves and various types of structures in water. The program consist of two sub-programs, named POTEN and FORCE. POTEN solves the radiation and diffraction velocity potentials, given in Sec. 2.1, on the body-surface. The FORCE sub-program calculates the hydrodynamic coefficients, the motions, and the first- and second-order forces, in addition to the velocities and pressures on the body surface. The input files required by WAMIT confines the problems to be solved, and a total description of all the possibilities within WAMIT and the required input files can be found in the *WAMIT User Manual* [25]. For the analyses in this thesis, the traditional lower-order panel method was chosen, and the following input files were adapted to suite the analyses.

The *.pot*-file defines the environmental parameters, such as the the water depth and wave periods. In addition, the number of DOFS to solve for, and a *.gdf* mesh-file

had to be specified here. The FORCE subprogram requires a force control file *.frc*, where the hydrodynamic parameters to be evaluated have to be listed. The possible options in the *.frc*-file are given in Fig. 3.1.

Option	Description	Filename
1	Added-mass and damping coefficients	*frc*.1
2	Exciting forces from Haskind relations	*frc*.2
3	Exciting forces from diffraction potential	*frc*.3
4	Motions of body (response amplitude operator)	*frc*.4
5p	Hydrodynamic pressure on body surface	*frc*.5p
5v	Fluid velocity vector on body surface	*frc*.(5vx,5vy,5vz)
6p	Pressure/ free-surface elevation at field points	*frc*.6p
6v	Fluid velocity vector at field points	*frc* .(6vx,6vy,6vz)
7	Mean drift force and moment from control surface	*frc*.7
8	Mean drift force and moment from momentum	*frc*.8
9	Mean drift force and moment from pressure	*frc*.9

Figure 3.1: Available analysis options in WAMIT v7 [25], where the options can be specified in the *.frc*-file.

As mentioned the body is defined by the *.gdf* mesh file, where the number of symmetry planes have to be specified. The control file *.cgf* provides WAMIT with the parameters and options for the analyses, and if a necessary parameter is not included, WAMIT will use the default value. The *fnames.wam* specify the names of the aforementioned files, and the configuration file *config.wam* and the license file *userid.wam* also have to be included in the directory to be run.

The output from WAMIT is given in nondimensional forms, and the body geometry, hydrodynamic loads and forces are given using Cartesian coordinates. The added mass and damping coefficients, the body motions η_j (RAO), and free-surface elevation are made nondimensional the relations given below:

$$\bar{A}_{kj} = \frac{A_{kj}}{\rho L^m} \qquad \bar{B}_{kj} = \frac{B_{kj}}{\rho L^m \omega} \qquad \bar{\eta}_j = \frac{\eta_j}{\zeta_a / L^n} \qquad \bar{\zeta} = \frac{\zeta_{fp}}{\zeta_a}$$

L is defined as the *ULEN*-parameter, which have been set to 1. Thus, the term L^m and L^n becomes unity.

3.1.1 Limitations

The assumptions made in linear potential flow theory makes it possible to describe linear induced wave motions and forces, as stated in Sec. 2.1. However, the assumptions, and specially the one concerning inviscid fluid, creates noteworthy limitation when it comes to describing the "real world". For structures with both moonpools and skirts, as the one investigated here, the viscous effects such as flow separation, will contribute to significant damping, and these effects can not be captured by WAMIT. As a result the motions will be overestimated around resonance periods, and this consequence should be taken into consideration when analysing the numerical results.

In WAMIT version 7 and higher, the option of including channel walls have been added, making it possible to better replicate the experimental tests. The channel walls are assumed to perfectly reflect the waves, if no other option for the reflection parameter is given. However, the channel walls can lead to a transverse resonance wave effects, which occur when the width is equal to the wave length λ times and integer. For the SWACH concept, which is symmetric about the centreline of the tank, the wave resonance will occur for $kw = 2n\pi$, with $n = (1, 2, 3..)$ and k being the wave number. Thus, extra care had to be taken during the analyses with channel walls to avoid resonance, and the program struggled to obtain the results with the tank walls.

Another limitation in WAMIT that might have an impact on the result obtained in this thesis concern the field points on the free surface that are close to, or inside, body water lines. As the free surface elevation inside the moonpool of the structure were of high interest, the field points are set as close to the walls of the moonpool as possible to try to capture the sloshing. Thus, some non-physical results from the filed points within the moonpool could be expected, and should be looked out for.

3.1.2 Mesh and convergence study

Mesh

In common with most numerical solvers the body or bodies have to be meshed with an adequate mesh size. Maël Moreau was generous enough to provide a MATLAB script to generate the mesh, and his code implements the meshing program NEMOH. The two codes supplied consisted of *DockMeshing.m*, which defines the cross-section to be meshed, and *nemoh2wamit_01a.m* which generates the mesh to the desired *.gdf* format using NEMOH.

As a result of the xz- and yz-symmetries of the structure, only one forth of the cross-section was necessary to mesh. Fig. 3.2 shows the quarter mesh computed in MATLAB for the SWACH foundation, given by its model scale parameters.

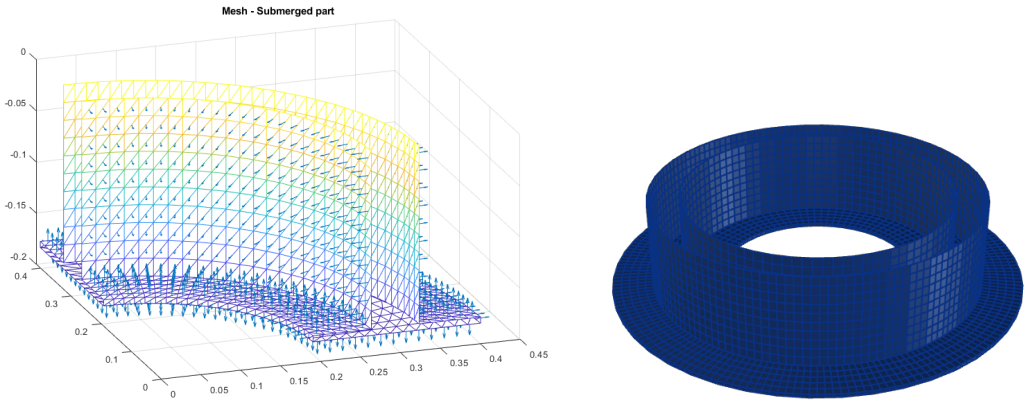

(a) Submerged mesh created in MATLAB (b) Full *gdf*- mesh from NEMOH

Figure 3.2: Mesh with 1400 elements, computed for the lab mode using the provided MATLAB codes. (a) displays the mesh with the elements and its normal vectors, and (b) the full mesh of the model from NEMHO, visualised by Rhino. The symmetry of the structure makes it possible to only mesh one quarter of the structure, and only the submerged part is meshed. The body centre is defined in the centre of the coordinate system, with the sea surface at $z = 0$

Convergence study

A mesh sensitivity study was conducted prior to the analyses, to obtain the necessary number of mesh panels. In Tab. 3.1 the number of elements chosen in MATLAB and the resulting number of panels in the *.gdf*-file are shown. The mesh convergence was evaluated using the added mass and damping coefficients in heave. In addition,

the effect of the mesh size on the motions were examined using a selected number of mesh sizes.

It should be noted that the mesh convergence study was executed before the experimental model was completed, so the dimensions are slightly different as described further on in Ch. 4, and the response here is not representative for the experimental model. However, the comparison of the mesh size are still valid.

Table 3.1: Number of elements for the mesh used in MATLAB and the following number of panels in the *.gfd*-file after the NEMOH mesh has been transformed.

Mesh	1	2	3	4	5	6	7	8
Number of elements MATLAB	600	800	1000	1200	1400	1600	1800	2000
Number of panels WAMIT	552	780	924	1104	1332	1596	1620	1800

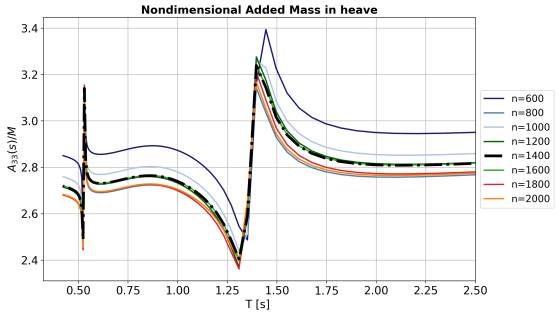

(a) Nondimensional A_{33} for different n

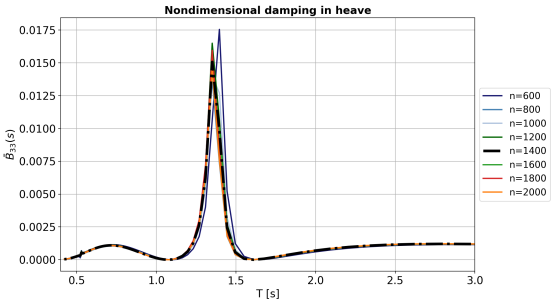

(b) Nondimensional B_{33} for different n

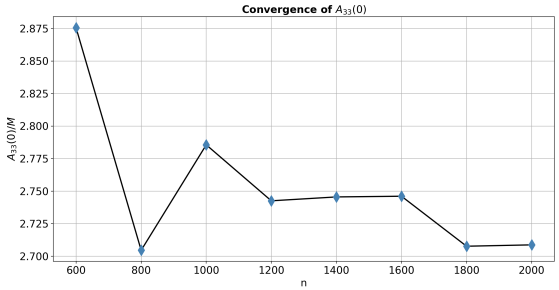

(c) $A_{33}(\omega = 0)$ for different n

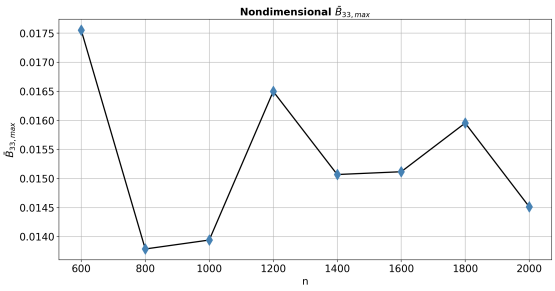

(d) $B_{33,max}$ for different n

Figure 3.3: Convergence study of WAMIT model using the nondimensional added mass and damping coefficient in heave as measuring parameter, plotted against wave period in model scale and the number of elements n.

Based on the $A_{33}(\omega = 0)$ for the different number of elements n, the mesh appear to converge between 1200-1600 number of elements. However, for n = 1800/2000 the added mass decreases slightly. Nonetheless, this difference was found to be approximately 1 %, and was deemed negligible. Thus, based on added mass alone, 1400 elements appears to be a suitable mesh size, as the computational time would only increase with the number of panels, and not necessary provide any better

results. Looking at $\bar{B_{33}}$, the same convergence can not be seen, and the maximum damping fluctuates much more with changing number of elements. However, the maximum damping value appears to occur around the same frequency for $n > 600$. The damping coefficient for $n = 1400$ has a middle value of the ones computed.

It should be mentioned that during the convergence analyses WAMIT struggled to solve the radiation and diffraction problems for $n = 1800$, due to singularities during the integration. This error was bypassed by using the ILOG = 1 option in WAMIT, which is default set to 0. By changing it to 1, the program utilises another option to integrate the logarithmic singularity. Thus, the change in added mass could be a result of change of integration method. This error was not met using $n = 2000$, and WAMIT managed to execute the run without any errors. Thus, the program might a appear to be a bit unstable around such high number of panels, and the result might not be fully trustworthy for such fine meshes.

From evaluating the surge, heave and pitch response shown in Fig. 3.4, the mesh size does not appear to have a huge impact on the motions. The response in surge, heave and pitch were evaluated for only $n = 600, 1000, 1400, 1800$, and the largest difference is the maximum value in heave, which correlates to the results from the damping coefficient. Thus, the motions verify that a mesh size of 1400 elements should be sufficient.

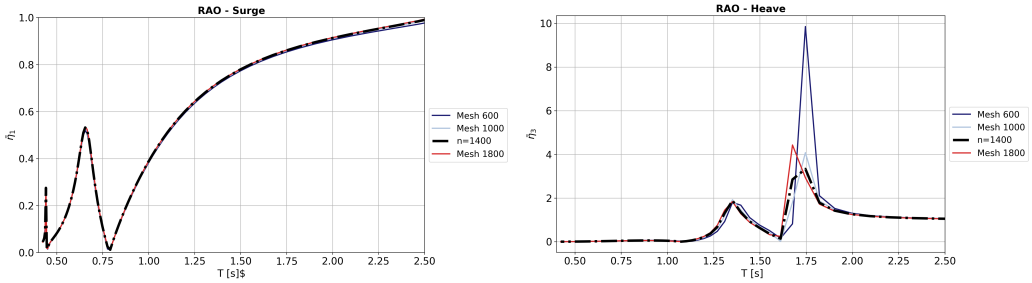

(a) Nondimensional surge for different number of elements n

(b) Nondimensional heave for different number of elements n

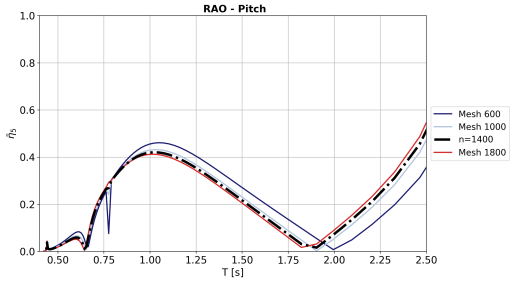

(c) Nondimensional pitch for different number of elements n

Figure 3.4: Convergence study of WAMIT showing the surge (a), heave (b), and pitch (c) motion for different number of elements n.

3.1.3 WAMIT analyses

The effect of the skirts, the moonpool and sloshing modes on the responses of the structure were to be investigated using different models in WAMIT. A short description of each of the models and the following analyses implemented are provided here. The draught study investigated how different draughts effected the response in the three DOFs surge, heave and pitch, the four model study were conducted to examine the impact of the skirts and sloshing the effects, and the experimental reproductions were used to compare the numerical results to the experimental ones.

3.1.4 Draught study

The draught study was conducted using the following models, infinite water depth and no channel walls present. The lab model was changed by increasing the draught, and the mass and vcg was corrected to account for the larger displaced volume.

1. **The lab model:** The 1:100 scale model of the SWACH concept with inner - and outer skirt and a moonpool, having the same dimensions as the model from the experiments.
2. **Draught = Inner diameter:** The draught set equal to the inner diameter of the hull of 0.527 m.
3. **Draught = Outer hull diameter:** The draught is set equal to the outer hull diameter of 0.647 m.
4. **Draught = Skirt diameter:** The draught is set equal to the outer skirt diameter of 0.801 m.
5. **Draught = 2x original draught:** The draught is set equal to twice the original draught, equalling 0.36 m.
6. **Draught = 0.26:** The draught is set equal 0.26 m.

3.1.5 Investigation of skirt effects

To evaluate how the skirt and sloshing effects would impact the response, a comparison study of four different models were conducted. The analyses were run using infinite water depth, and without channel walls. In addition to the lab model, the following models were used for the study.

1. **Model without skirts:** The lab model is without inner- and outer-skirts. The moonpool and outer diameter are kept equal to the lab model.
2. **Model without inner skirt:** The lab model is without the inner skirt. The other parameters are kept equal to the lab model.
3. **Deep cylinder:** The draught is set equal to the moonppool diameter of 0.527, and the skirts have been removed. The the mass and vcg were kept the same.

3.1.6 Experimental reproductions

A numerical replica of the experimental model was created for comparison of the numerical and experimental results. The lab model was adapted with baffles to simulate the effect they would have in the experiment. The solid baffle was modelled at three positions within the moonpool, corresponding to N1, N3 and N6 as defined in Ch. 4. In addition to the lab model, a scaled model from the Sevan concept was included as the model was built on those parameter. The analyses were conducted with both infinite water depth and a finite water depth of $h = 0.8\,m$. A channel with width of $2.5\,m$ were also included in analyses using the lab model and the lab model with baffles, to try to capture the channel reflections from the lab experiment.

The results from all the different analyses are presented in Ch. 5.

CHAPTER 4

Experiments

In this chapter the model tests and post-processing methods are described. The planning of the experiment began during the pre-project, and the chapter have been continued in this thesis. The chapter contains information about the experimental set-up and instrumentation, the model parameters, and the regular wave and irregular wave tests executed. The model experiment was conducted in the Small Towing Tank (Lilletanken) at NTNU, and was carried out during February and the beginning of March, where the last part was finished at the end of April. The aim of the model tests were to investigate the motions of the SWACH foundation, presented in Sec. 1.1, with additional focus on the implementation of baffles. The second order effects were expected to be significant for this type of structure, and the experiment have been necessary to examine these effects. The geometry of the foundation was simplified compared to the Sevan model, and in Fig. 4.2 the model can be seen floating in the tank.

4.1 Experiment set-up

The experiment was conducted in Lilletanken at NTNU in Trondheim. The tank is 25 meters long, 2.5 meters wide and has a maximum water depth of 1 m. The water density can be assumed to be 1000 kg/m^3 for fresh water. For this experiment the water depth was set to 0.8, due to limitations of the wave maker.

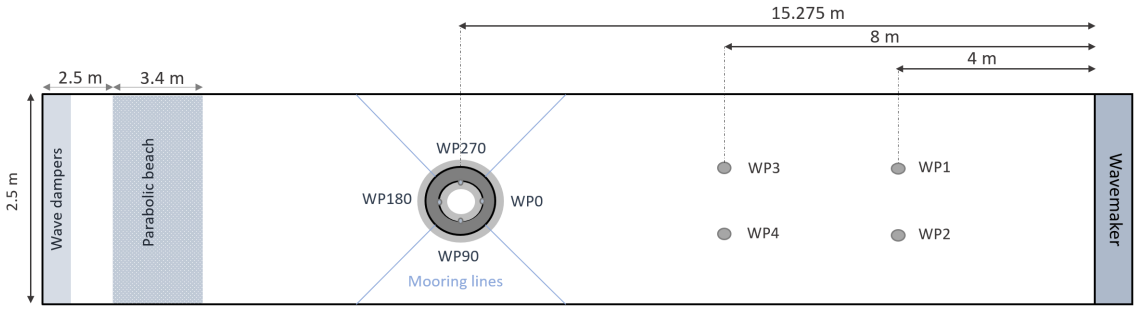

Figure 4.1: Experimental set-up of the model in Lilletanken. WP 1-4 shows the locations of the wave probes, and WP0 - WP270 mark the wave tapes inside the moonpool. Four mooring lines are attached to the model at 45 °, and centre of the model is located at the pit centre, 15.275 m from the wave maker.

Fig. 4.1 shows an overview of the experimental set up in Lilletanken, with the centre of the model corresponding to the pit centre of the tank at 15.275 meters from the wave maker. A perforated parabolic beach was installed approximately 2.5 meters from the end tank wall, and slightly submerged to reduce the wave reflection, found to better the efficiency by [26]. The model was moored with four mooring lines at 45 ° each, and the lines were connected to the model at approximately 1 cm from the top. The draught was set to 0.18 m for the model without additional baffles.

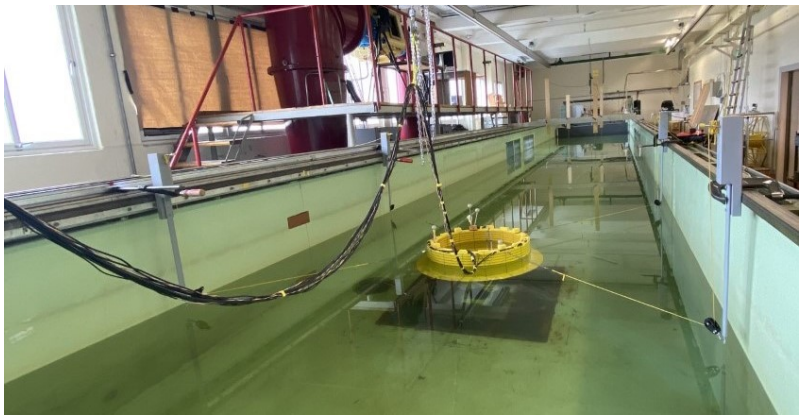

Figure 4.2: Picture taken from the lab showing the model moored in the tank, with the wave maker in front.

Instrumentation

Oqus was used to measure the motions in the six degrees of freedom. Oqus is an optical tracking technology, which can provide the position and motions of fast moving objects with high accuracy using cameras and reflective markers [27]. In addition to Oqus, three accelerometers were included in the instrumentation as contingency in case Oqus should fail. The accelerometers were placed on top of the model, one horizontal located at 0° and two verticals attached to each side, at 90° and 270°. The mooring line forces were measured by force rings implemented between the model and the mooring lines.

Eight wave probes were used to measure the wave elevation. Two pairs of two wave probes were placed at four and eight meters from the wave maker to measure the incident waves. To measure the surface elevation inside the moonpool, wave tapes were attached to the inside wall at 90° intervals, starting at 0°. Tab. 4.1 shows the approximate distance from the wave maker to each wave probe. WP1-4 are wave probes and WP0 to 270 are wave tapes.

Table 4.1: Placement of wave probes for the lab experiment. WP1-4 are wave probes, and WP0-270 are wave tapes.

Wave probes	*WP1*	*WP2*	*WP3*	*WP4*	*WP0*	*WP90*	*WP180*	*WP270*
Distance from wave maker [m]	4	4	8	8	15.01	15.28	15.54	15.28

Prior to the experiment all the measuring devices had to be calibrated, and throughout the weeks of testing the wave probes were calibrated several times to account for changes in the water temperature.

4.1.1 Froude Scaling

When testing offshore structures in waves, the gravitational forces will dominate the formation of the surface waves. The dimensionless Froude number (Eq. 4.1, which show the influence from gravity on fluid motions, are commonly used for scaling structures which are mostly influenced by surface waves [28]. The scaling principle using Froude scaling builds upon the Froude number being the same for the model and full scale, which makes it possible to create similarities between the forces and dimensions in full and model scale. For the experiment performed here, Froude

scaling was found most suitable, and a scaling factor of $\Lambda = 1 : 100$ was used.

$$F_r = \frac{u}{\sqrt{gL}} \tag{4.1}$$

Using Froude scaling the following similarities apply for the model [28]:

Geometric similarity:	$\Lambda = \frac{L_F}{L_M}$
Mass:	$M_M = \frac{\rho_M}{\rho_F}\frac{1}{\Lambda^3}M_F$
Force:	$F_M = \frac{\rho_M}{\rho_F}\frac{1}{\Lambda^3}F_F$
Moment:	$M_M = \frac{\rho_M}{\rho_F}\frac{1}{\Lambda^4}M_F$
Pressure:	$P_M = \frac{\rho_M}{\rho_F}\frac{1}{\Lambda}P_F$
Time:	$T_M = \frac{T_F}{\sqrt{\Lambda}}$
Frequency:	$f_M = \sqrt{\Lambda}f_F$
Velocity:	$V_M = \frac{V_F}{\sqrt{\Lambda}}$
Acceleration:	$a_M = a_F$

The subscripts F and M denotes full scale and model scale, respectively.

4.1.2 Model parameters

Following the Froude scaling with $\Lambda = 1 : 100$, the scaled model dimension could be obtained. The actual model used however, differed a bit from the desired one, and both the scaled model and the lab model parameters are shown in Tab. 4.2. The reason for the discrepancy is discussed in Sec. 4.4.

Table 4.2: Scaled model and lab model parameters given in [cm] for the SWACH Wind foundation, The scaled model is based on the information provided by Sevan SSP, using Froude scaling $\Lambda = 1 : 100$. The lab model information is from measurments.

Parameters	Symbol	Model scale [cm]	Lab model [cm]
Model height	H	25.5	25.5
Draught	T	18	18
Outer skirt diameter	D_s	80	80.1
Hull diameter	D_h	64.5	64.7
Moonpool diameter	D_{mp}	53	52.7
Moonpool opening diameter	D_{mpi}	38	38.1
Hull thickness	R_t	5.75	6
Outer skirt length	L_o	7.5	7.7
Inner skirt length	L_i	7.5	7.3
Skirt height	t	0.5	0.6

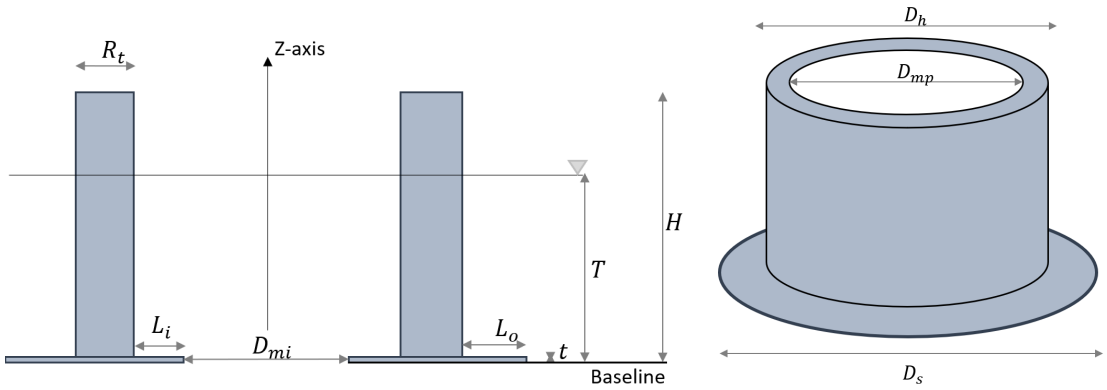

(a) Model cross-section (b) 3D-view of model

Figure 4.3: Model sketch with references to the parameters given in Tab. 4.2.

Baffles

Two different types of annular baffles have been tested inside the moonpool at three different levels below the free surface. The model had the possibility of placing the baffles at six different positions, but due to time limitations only the three shown in Fig. 4.4 were tested. N1 denotes the first position at 1.5 cm below the free surface, and N6 the lowest, which is 8.4 cm above the inner skirt. The baffles' properties are shown in Tab. 4.3, where B_f gives the ring width and τ the perforated ratio.

Table 4.3: Baffle properties, where τ is the perforated ratio and B_f the width of the annular plate.

Type	B_f [mm]	τ	Thickness [mm]
1	50	0.35	1
2	50	1	1

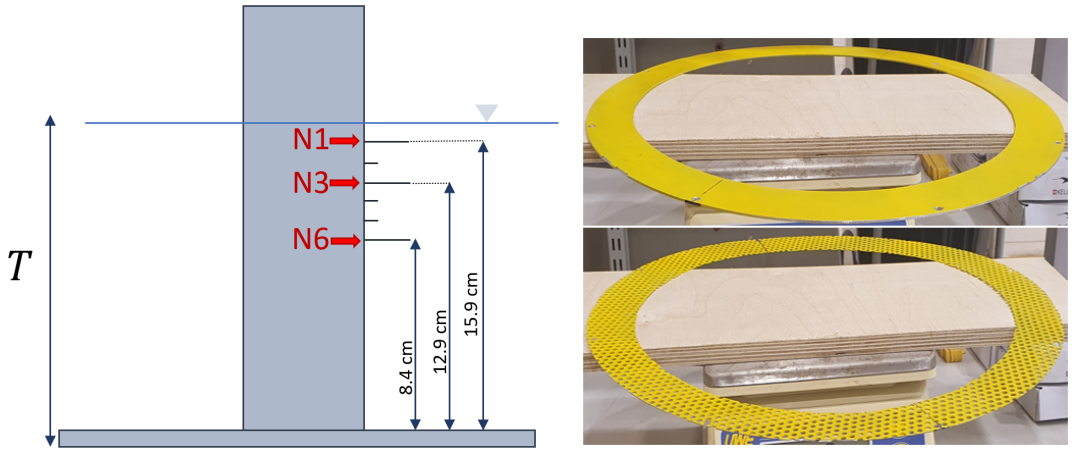

(a) Baffle positions

(b) The two types of baffles

Figure 4.4: Fig (a) shows the three possible baffle positions given by N1, N3 and N6. Fig. (b) shows the two types of baffles implemented, with the solid baffle (top) and perforated baffle (bottom)

Mooring

During the planning of the experiment the pre-tension in the mooring lines was estimated using information provided by Sevan. However, during the set up, the pre-tension calculated was found to be insufficient. Using springs of 10 N/m, the springs were elongated between 27 - 32 cm. and resulting in a pre-tension around 3 N. Due to the set-up and the limitations of the lab, it is quite difficult to obtain the same pre-tension in each mooring line, and this has been discussed in Sec. 4.4.

The model was moored by four lines connected at 45 ° intervals, and were attached to the structure approximately 1 cm below the top. Fig. 4.5 shows the model in Lilletanken with the mooring lines and instrumentation cables.

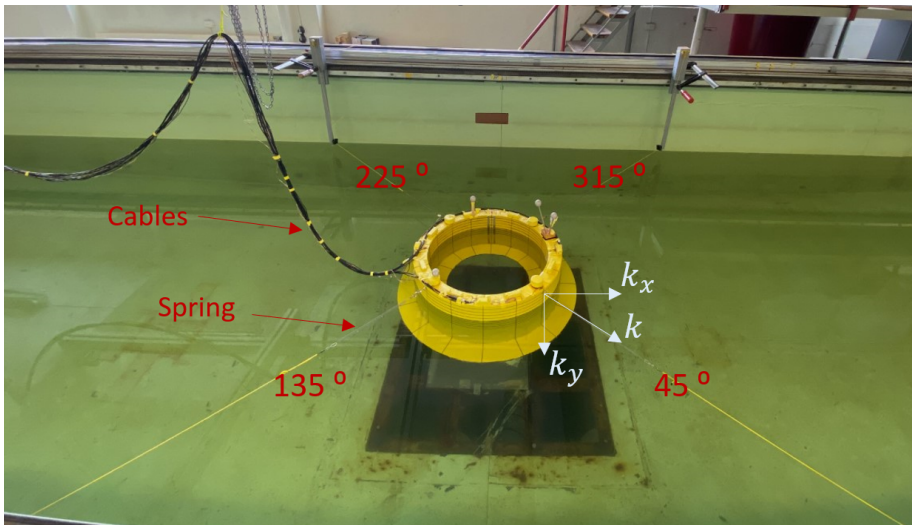

Figure 4.5: Picture taken from the lab showing the mooring lines and instrumentation cable.

The spring stiffness k in each mooring line was $10\,N/m$, and k_x and k_y are the spring stiffness components in x- and y-direction respectively. The mooring lines were connected approximately 6.6 cm above the vertical centre of gravity, resulting in additional restoring for coupled heave and pitch motions, as well as the expected surge and pitch alone.

The additional restoring coefficients from the mooring lines are found using the equations given in Eq. 4.4,

$$C_{11} = 4k_x \tag{4.2}$$

$$C_{55} = F_{pre}D_h \tag{4.3}$$

$$C_{15} = C_{51} = 2k_x a \tag{4.4}$$

with k_x being the spring stiffness component in x-direction, F_{pre} the mooring line pre-tension, D_h the hull diameter, and a the vertical distance from vcg to the mooring lines.

The analytical restoring coefficients were calculated assuming a pre-tension of 3 N for each line.

4.1.3 Decay tests

To evaluate the natural periods of the structure, decay tests in surge, heave and pitch were tried out. However, as mentioned in Sec. 1.2, Reiersen et al. [13] showed that for structures with moonpools, monotone decays can be difficult to obtain, specially for heave and pitch. However, a clear decay of the surge motion was expected as the motion should be slow enough to not be affected by the moonpool. In App. A in A.1, results from the decay tests with the solid baffle at N3 can be seen.

$$T_n = 2\pi\sqrt{\frac{A_{nn} + M}{C_{nn}}} \tag{4.5}$$

The analytical natural period in surge, heave and pitch were found using the relation shown in Eq. 4.5, and they appear to correspond with the results from the decay test. However, there were some discrepancies as expected. Tab. 4.4 shows the natural periods obtained analytically, from the model without any baffles and from baffles at position N3 for the solid and perforated plate.

Table 4.4: Natural periods for the chosen models

	Analytical	No baffles	Solid N3	Perf. N3
Surge T_1	12.54	12.50	12.49	12.51
Heave T_3	1.66	1.64	1.36	1.75
Pitch T_5	2.36	2.33	2.72	2.72

The natural periods from the experimental tests were obtained using PlotMe from MATLAB. The natural periods found for heave and pitch showed the largest discrepancies, and were sensitive to the time windows used. For heave and pitch, no clear decays were obtained, corresponding to Reiersen et al. [13], and the natural periods obtained should not be fully trusted. Nonetheless, the natural periods in heave and pitch can used as estimates, and be compared to the resonance peaks from the numerical analyses. Since the decay test is more likely valid for the surge motion, the estimates for surge are expected to be more accurate.

4.2 Regular wave tests

Three different wave steepnesses were chosen for the regular wave tests, $\epsilon = 1/30$, $\epsilon = 1/40$ and $\epsilon = 1/100$. The wave lengths λ and wave heights H were calculated applying linear wave theory. The table shows the wave heights for the smallest wave, largest wave and for the period where the water depth becomes finite compared to the wave length, using the definition given in Sec. 2.4.2.

Table 4.5: Regular waves info

		$\epsilon = 1/30$	$\epsilon = 1/40$	$\epsilon = 1/100$
T[s]	λ [m]	H [m]	H [m]	H [m]
0.6	0.562	0.0187	0.014	0.0056
1.05	1.712	0.057	0.043	0.017
2.2	5.477	0.183	0.137	0.055

Tab. 4.6 shows the different regular wave sets that have been tested for the three wave steepnesses, showing the minimum and maximum wave period for each set, the period interval (ΔT), the number of periods and rest time between each period.

Table 4.6: Regular waves given in model scale, and divided into test groups.

Nr.	Min period [s]	Max period [s]	ΔT [s]	Nr. of periods	Rest time [s]
1	0.6	2.2	0.1	60	480
2	0.6	2.2	0.05	60	480
3	0.6	2.2	0.025	60	480

The different wave test shown in Tab. 4.6 are a result of adapting the test throughout the experiment. In the initial plan only regular waves with $\epsilon = 1/30$ were to be used for the runs with baffles, however, additional wave test with $\epsilon = 1/40$ and $\epsilon = 1/100$ were carried out for for some of the baffle tests.

4.3 Irregular wave tests

Tab. 4.7 presents the irregular sea states used for the model test, given with the full scale parameters. The JONSWAP spectrum was used to create the wave time series, and the sea states are based on representative data for the northern North Sea provided by the table on page 31 from *Sea Loads on Ships and Offshore Structure* [29], seen in App. A.2. Each realisation lasted for 18 minuets, corresponding to 3

hour realisations in full scale. Between each realisation there was a significant pause to make sure that the system was calm enough before a new realisation.

Table 4.7: Irregular sea states given in model scale. The values for H_s and T_p are representative for the northeren Norst Sea [29].

Sea state	$H_{s,model}$ [m]	$T_{P,model}$ [s]
J-91418	0.09	1.4
J-81218	0.08	1.2
J-61218	0.06	1.2
J-71018	0.07	1.0
J-51018	0.05	1.0
J-4818	0.04	0.8

4.4 Error sources

From lab experiments there are due to be both possible bias and precision error sources which can contaminate the results. Some possible bias errors and a short discussion on their possible effects on the results are listed. Due to time limitations the precision error has not been evaluated.

4.4.1 Bias errors

The bias errors are the results of simplifying the target model, and such errors are often know from the beginning of the experiment. For the experiment conducted as part of this thesis, quite a list of possible bias errors were known in advance, and in this section some of the errors that were deemed most significant have been detailed.

Incident waves

Both the regular and irregular waves used for the experiments were created using provided MATLAB scripts. The correlation between the desired theoretical wave and the measured one where found to correspond nicely for the regular wave periods below 1.1 to 1.3 depending on the wave steepness. This is thought of being a results of going from deep water waves to finite water waves, hence resulting in a larger deviation. However, there is no clear under- or over-prediction of the incident wave heights, which can be seen from Fig. 4.6, the measured wave heights fluctuates around the theoretical ones. Another strange deviation from the theoretical wave

heights are the troughs around 1.8 and 2.0 s. The trend can be seen from most of the regular wave tests, but are most prominent for the wave steepness of 1/30, and might indicate that there are some struggles for the wave maker with these two periods and $\epsilon = 1/30$.

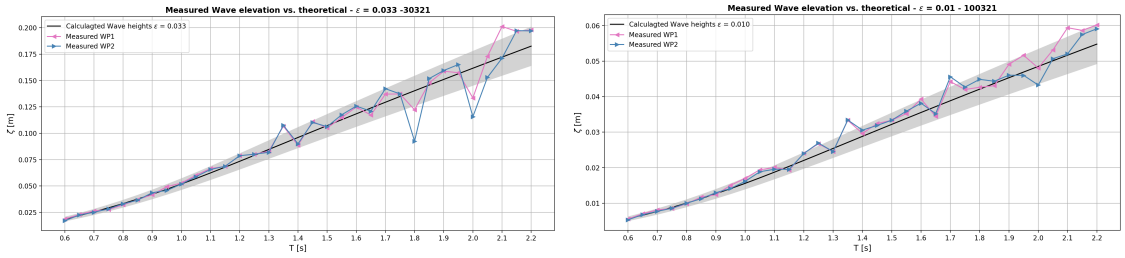

(a) Theoretical vs measured waves from WP1 and WP2 with $\epsilon = 1/30$

(b) Theoretical vs measured waves from WP1 and WP2 with $\epsilon = 1/100$

Figure 4.6: Fig. (a) shows the theoretical vs. measured wave for $\epsilon = 1/30$, and Fig. (b), shows for $\epsilon = 1/100$. The grey area sets the 10 % deviation limit from the theoretical wave. It can be seen that for most periods, the measured wave heights lie within this interval.

The same trend could also be seen from the measurements from WP3 and WP4, substantiating the hypothesis that the wave maker or wave probes struggle with $\epsilon = 1/30$ and wave periods of 1.8 and 2.0 s. The figures for WP3 and WP4 can be seen in App. A.3, Fig. A.3. In App. A.3 additional figures showing the measured wave elevation vs. the theoretical can also be found.

Uncertainties in wave probes and wave maker

The wave probes measure the wave height based on the rise and fall of the water level in the tank, using the conductivity of water. Thus, if the conductivity is influenced either by a change of temperature or some sort of oil spill, the measured wave height might be erroneous. No oil spill was detected during the time, and the change of temperature was continuously monitored. However, a small change of temperature has been found to affect both the density and viscosity of the water, and by using the table made by Faltinsen ([29], page 175), the uncertainty of the viscosity of fresh water is estimate to be $\pm 2.8 \cdot 10^{-8} [m^2/s]$ and $\pm 0.18 [kg/m^3]$ for the viscosity, resulting in possible deviations of 2.8% for ν and 0.018% for ρ for each degree of change in the water temperature. With a notable increase in the water temperature, this could lead to a considerable bias error. Anyhow, it is unlikely that significant changes would occur in the short time between the wave period of 1.8 s and 2.0.

Nonetheless, the importance of the temperature has been taken into consideration, and when the water temperature showed either an increase or decrease, the wave probes were calibrated anew to account for this change.

The wave maker used in the small towing tank is of the piston type, and there are four cylinders that pushes the plate. One of the pumps however, are malfunctioning, which might result in a slightly askew piston motion instead of the fully monotone one. As a result, the change could lead to a bit unsymmetrical wave which again can induce types of tank wall resonances. During the experiment several types of standing waves in the tank were observed, however the period of which these effects were seen were unfortunately not noted at the time. Hence, the deviation form the theoretical wave for periods of 1.8 and 2.0 could be the result of standing waves leading to smaller wave heights being measured.

Leakage into the space behind the piston wave maker is another error source, as the leakage results in a decrease in the water level. Pumps were installed to counteract this leakage, however they operated on a specified timer and not measurements of the water level in the area behind. Hence, the water level could decrease significantly in the tank before the pumps were started. This decrease and increase of the water level could be seen for the longer runs, and the effect had to be accounted for during the post-processing. However, this effect is more likely to result in the general under prediction of the wave heights for several succeeding wave periods.

Uncertainties in water depth

I addition to leakage behind the wave maker, the tank itself also slightly leaks. The water level was measured each morning at the same point in the tank using a folding ruler and visually checking that the water as at the desired depth of 0.8. The water depth was found adequate between 0.78 and 0.82, as the difference this had for the produced waves were found to be insignificant.

Tank wall effects

When doing experiments in a tank, there will be tank wall reflections from both the sides and the tank wall ends. Between each run there was a significant pause to make sure that the water had calmed down before a new set of waves were initiated, and the steady state windows used in the post-processing were taken before the

reflected waves would have reached the model. However, the reflections from the side walls were not possible to account for, and these reflected waves were found in the numerical analyses to affect the heave motion.

Uncertainties in the model

The model was built from parameters provided by Sevan. However, the exact measurements ended up deviating a bit from the desired ones as shown in Sec. 4.1.2. Both the radii of gyration and vcg did not match the scaled model, and the weight ended up being approximately 1 kg heavier. All these parameters are important when it comes to the motions of the structure, and from the numerical analyses comparing the scaled model to the lab model the results show that the motions differ. The inaccuracies in the model geometry were found to be around $\pm 2mm$ for the measurements of the lengths and widths of the model. The thickness of the skirt was $1mm$ thicker than wanted, and so was the solid baffle.

Another possible error source is the instrumentation fastened to the model. All the instrumentation fastened at the model had to be connected to the converters by cables, resulting in a large cable bundle hanging from the back of the model, seen in Fig. 4.7.

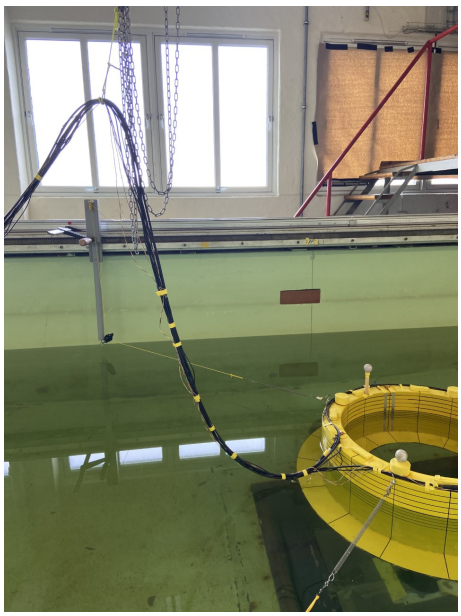

Figure 4.7: Picture from Lilletanken showing the cable bundle attached to the model

It was tried at best to make sure that the cables did not pull the structure when in motion, but despite our best efforts it could be seen during several test that the

cable had a small impact on the structure in pitch and surge. It was also noted that the cable seemed to give the structure a slight initial pitch.

Mooring lines

The mooring lines were connected at 45 ° intervals to the model, and springs were implemented to get the desierd pre-tension. In the small towing tank, the pre-tension have to be achieved by manually pulling and fastening the mooring lines whilst positioning the model at the wanted position. When the positioning took place, on of the lab technicians were standing in the tank holding the model in place, whilst three other stood at the mooring lines. Despite this many people working on trying to obtain an equal pre-tension in each mooring line, that is not possible in this way, and the pre-tension deviated between 2.8 N and 3.1 N for each mooring line. In addition, the model ended up being shifted approximately 0.13 m of the centre of the tank, which had to be accounted for during the post processing.

It was later noted that the mooring lines were not stiff enough, resulting in slow surge motion, and slack in the rearward mooring lines during the most severe wave periods and sea states.

4.5 Post-processing

The post-processing for the regular and irregular wave tests have been quite different, and a short summary of each of the processes have been given her. The processing of data after an experiment can be quite time consuming, and during this thesis a lot of time have been spent obtaining the desired results.

4.5.1 Regular waves

The regular wave tests were either run for three, five or ten hours, where each wave period was repeated 60 times with eight minutes breaks in between. The response for each period were retrieved from the full time series, before any other form of adjustments to the results were made.

A short description of the procedure used for the regular time series is given her:

1. Extracting the correct time windows from the total time-series for each of the respective wave periods. The time series and time windows are shown in Fig. 4.8.

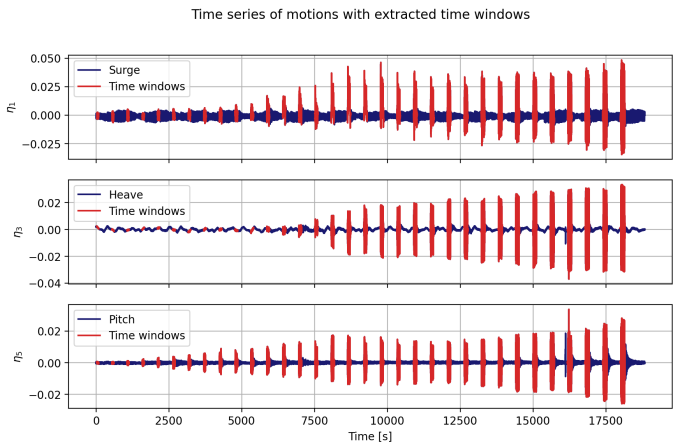

Figure 4.8: Time series of surge, heave and pitch showing the time windows in red extracted for further processing.

2. Filtering the response for each wave period to remove noise and higher-order effects. A Butterworth band-pass filter was used implementing cut-off periods corresponding to ±20% of the first harmonic wave period, to obtain the first harmonic response.

3. Find the steady-state response from the filtered time windows. The steady state interval was chosen after the ramp up periods, and before the wave reflections would reach the model again. The time it would take for the wave reflections to reach the model was calculated using the group velocity, giving the speed of the wave front.

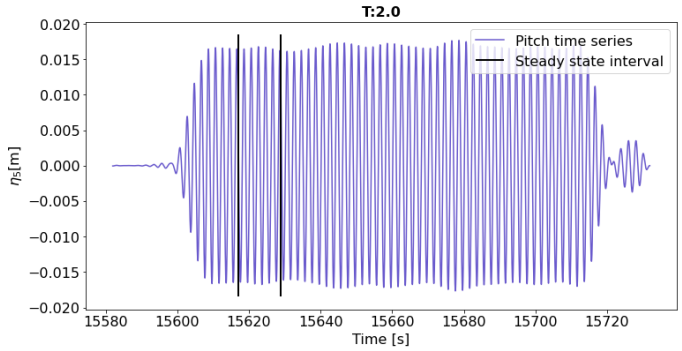

Figure 4.9: Time series of pitch fro a wave period of 2.0 s, showing the steady state interval in black

4. Calculate the mean wave height by finding the wave heights for each peak and trough from the steady state time windows, and then use the mean wave height to obtain the response amplitude.

By calculating both the response wave heights and the incident wave heights, the RAOs could be obtained using the equation Eq. 2.9 from Sec. 2.4.1.

Coordinate system

The wave elevation inside the moonpool from the wave tapes are given in the body fixed coordinate system. From WAMIT all the responses are given by the earth fixed coordinate system, so to be able to compare the numerical and experimental results, the experimental measurements were transformed to the earth fixed coordinate system by Eq. 4.6.

$$W^{EF} = W^{BF} + Z_i \tag{4.6}$$

The superscript EF stands for earth fixed, and BF body fixed. The Z_i represents the vertical displacement s_3 at point i from the body's centre of gravity, given by Eq. 4.7.

$$s_3 = \eta_3 + (\mathbf{R}\, x\, \mathbf{r})_3 = \eta_3 + y\eta_4 - x\eta_5 = \eta_3 - x\eta_5 \tag{4.7}$$

The roll motion was assumed negligible for the experiments, hence no contribution from roll in the vertical displacement at a point z_i have been used.

RAOs

The RAOS were computed using both the theoretical wave and the measured from the wave probes. In Sec. 4.4 the inconsistencies between the measured and theoretical waves were shortly discussed, and the discrepancies found resulted in some inaccurate points in the RAOs. The difference between using the measured wave and theoretical can be seen in Fig. 4.10, where the points around 18 s and 20 s have been marked to show where the largest discrepancy could be found.

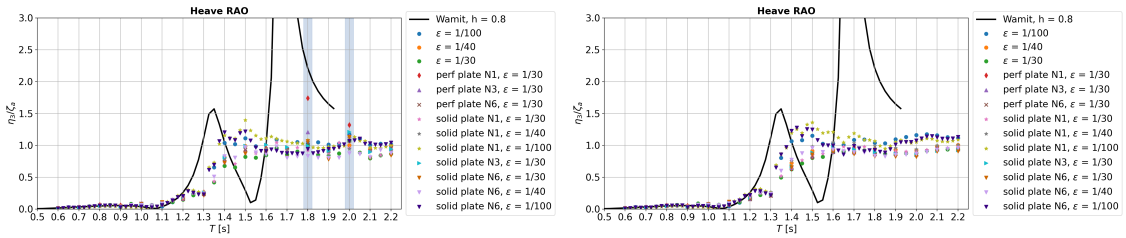

(a) Heave RAO from measured wave heights (b) Heave RAO form theoretical wave heights

Figure 4.10: Comparison of heave RAOs using (a) the measured wave heights from wave probes, and (b) the theoretical wave heights based on liner theory. The

The other points do not appear to show such large inconsistencies, and it was found more practical to use the theoretical wave and not the wave measurements for the regular wave responses.

4.5.2 Irregular waves

The transfer functions for the surge, heave and pitch response were obtained using the method and equations given in Sec. 2.5. The post-processing procedure for the irregular responses are shortly described here.

Smoothing and filtering

The irregular time realisations from the experiment were transformed to the frequency domain using the Fast Fourier transforms. Thus, spectrum presented in this section are shown using the frequency given by $[Hz]$

The raw spectrum data acquired from the irregular wave tests have been filtered before a smoothing method was applied. The filtering process for irregular sea states are not the same as for regular, and a much winder band was necessary to capture the response correctly. The higher-order effects are not filtered out in the same manner, and the goal was to remove the non-physical noise. The Butterworth filter was implemented for the irregular responses as well, and cut-of periods corresponding to 0.1 and 5 of the peak period was used.

The smoothing method applied consisted of averaging over a given interval for each of the frequencies in the spectrum. Hence, a short investigation of the interval limits were executed. For a given spectrum the smoothing process for each frequency f_i follows the relation given in Eq. 4.8. Bw gives the bandwidth for the interval for f_i. Tab. 4.8 shows the different bandwidths $\pm Bw$ tested for the smoothing process.

For the investigation a sea state with $H_s = 5m$, $T_p = 10$ was used.

$$S^{smooth}(f_i) = \text{mean}(S^{raw}(f_{i-Bw} : f_{i+Bw})) \tag{4.8}$$

Table 4.8: Bandwidth for smoothing intervals

Bandwidths; Bw			
10	25	50	100

The surge response spectrum for each of the four bandwidths are shown in Fig. 4.11, where the red curve represents the smoothed spectrum. For $Bw = 10$ and $Bw = 25$, the smoothed spectrum still follow many of the raw data fluctuations, whereas these fluctuations diminish when the bandwidths surpass 50. However, with larger bandwidths, some of the energy is not captured by the smoothed curve, and from Fig. 4.11 it can be observed that the first peak from the raw surge spectrum is not captured at all for $Bw = 50$ and $Bw = 100$. Thus, there have to be a balance between how smooth the spectrum should be, and an acceptable loss of captured energy.

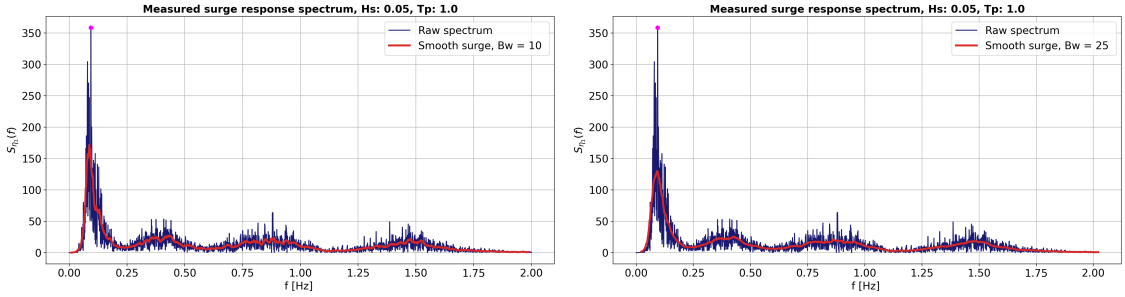

(a) $Bw = 10$

(b) $Bw = 25$

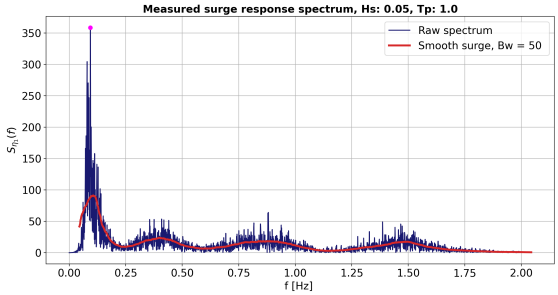

(c) $Bw = 50$

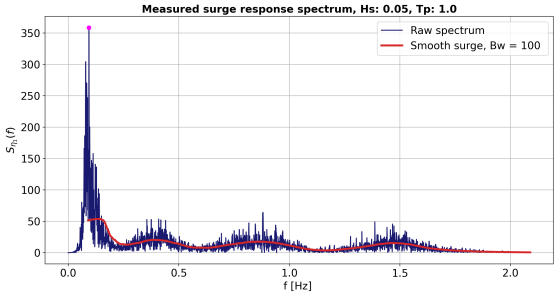

(d) $Bw = 100$

Figure 4.11

By looking at the pitch response for $Bw = 25$ and $Bw = 50$ in Fig. 4.12, the the differences between the smoothed spectrum and the raw are not that significant. Nonetheless the smoothed spectrum using $Bw = 25$ still shows some distinct fluctuations, and the smoother spectrum using $Bw = 50$ appear to be a better fit.

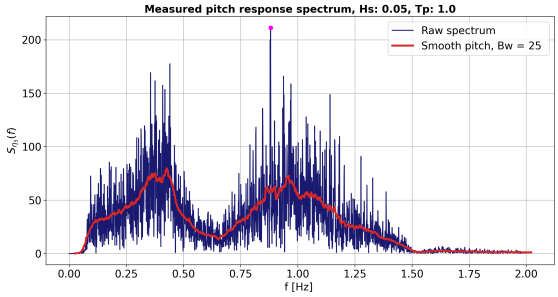

(a) $Bw = 25$

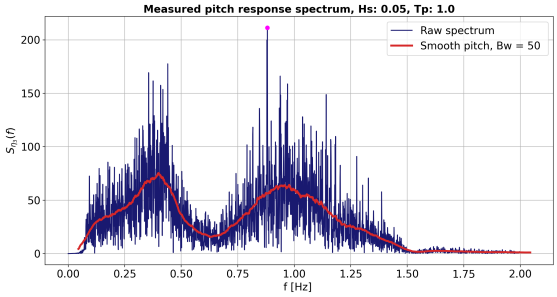

(b) $Bw = 50$

Figure 4.12

Before the transfer functions were computed the effect of the bandwidth on the response were shortly checked, and from Fig. 4.13, the different bandwidths appear to have an inconsequential impact on the transfer functions.

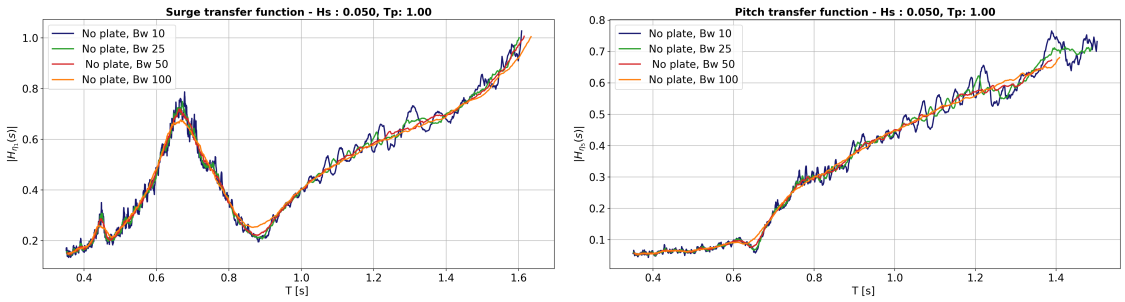

(a) Surge for $Bw = 10, 25, 50, 100$ (b) Pitch for $Bw = 10, 25, 50, 100$

Figure 4.13

A combination of both $Bw = 25$ and $Bw = 50$ was found to be the best solution for the smoothing process, where $Bw = 25$ have been used for the lower frequencies. A result of this combination have been included in Fig. 4.14 where the peak around 0.125 is adequately captured, and the curve appears nice and smooth.

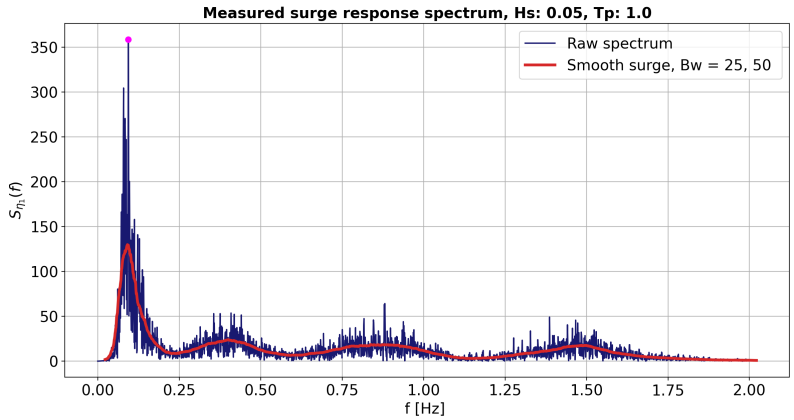

Figure 4.14: Combination of bandwidths

4.5.3 Area extraction

Fig. 4.15 display the process of extracting the correct areas for the transfer functions, where the yellow curves mark the areas collected for the surge and pitch responses. When computing the transfer function from an irregular sea state, the idea is to capture the response triggered by the waves, and not the second order responses, and the area within the energy of the waves, given by the blue curve, is the one of interest.

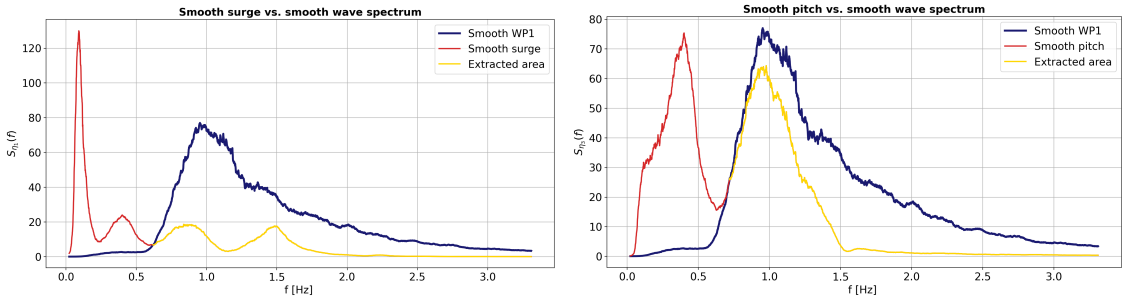

(a) (b)

Figure 4.15: Smooth surge and wave spectrum plotted together in (a). In (b) is the response excited by the wave energy, which is the extracted area used for the computation of the transfer function, shown in yellow.

This procedure had to be done for each of the irregular sea state results, where the area for each response had to be manually chosen. Even tough the response shown outside the wave spectrum are not included in the transfer functions, they are still important to evaluate as it shows how the structure responds to higher order effects.

RAOs

The RAOs or transfer functions were computed using the equations presented in Sec. 2.5, with the measured wave spectrum for each sea state and the response area as described above.

A slight offsets were seen for all the transfer functions, where in Fig. 4.16 the differences have been plotted. The grey graphs show the transfer functions before they have been adjusted, and the colours represent the transfer functions after the adjustment of subtracting the start value from the curve.

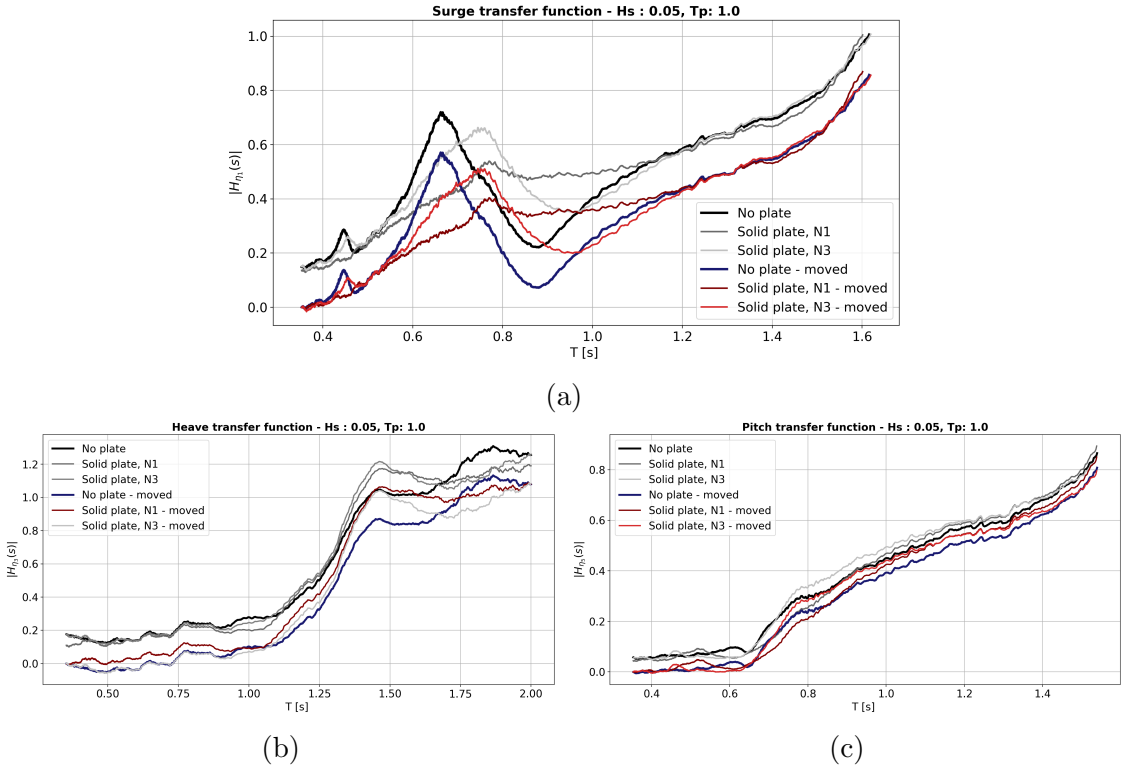

Figure 4.16: Transfer functions in surge (a), heave (b), and pitch (c), before and after they have been shifted subtracting the start value form the graph. They grey curves represent the unchanged transfer functions, and the coloured the shifted.

The transfer functions were expected to begin at zero, and since no apparent reason for the deviations have been found, they are likely a results of some measured noise which have not been captured by the filtering.

From Fig. 4.16 (a) and (c), the adjustment of the RAOs only shift the response such that it begins at zero. For heave on the other hand, the adjustments appear to cause some alterations in the response, and for some of cases the heave motion became negative for periods below 1.0 s. Thus, the adjustments have only been done for surge and pitch where the responses have been compared to the regular wave results, seen in Sec. 6.2.

CHAPTER 5

Numerical parameter studies

In this chapter the numerical results from the different analyses conducted in WAMIT are presented and discussed. Firstly, the results from the investigation into the skirts effect and draught sensitivity study are given, before the results from the numerical replicas are shown. All the analyses have been executed applying the model scale, and the model scale have been used to represent the data as well. The RAOs are given by the non-dimensional outputs $\bar{\eta}_i$ and $\bar{\zeta}$ as defined in Sec. 3.1. Selected numerical results will in Ch. 6 be compared to the experimental results.

5.1 Skirt effects

The investigation into the the skirts and draught were conducted in accordance with the objectives given in Sec. 1.3. The draught and skirt configuration have been set by Sevan, and the results from these analyses are included to provide a better understanding of the concept.

Fig. 5.1 shows the surge, heave and pitch RAOs where the effects of the skirts have been investigated.

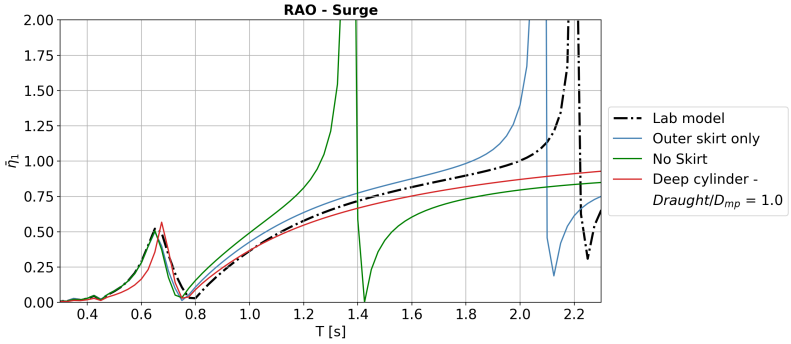

(a) RAO $\bar{\eta_1}$

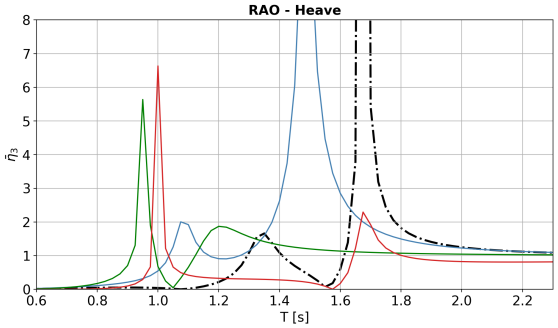

(b) $\bar{\eta_3}$

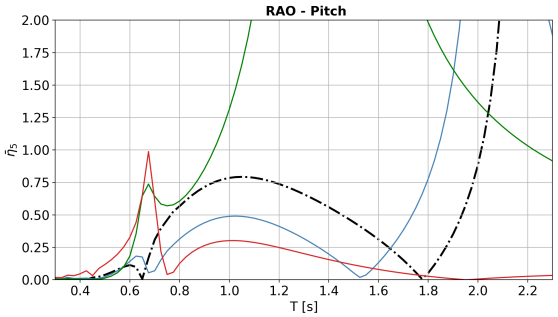

(c) $\bar{\eta_5}$

Figure 5.1: RAOs for surge, heave and pitch for a the lab model, a model with only the outer skirts and a model with no skirts. In addition a deep cylinder with draught equal to the moonpool diameter have been included. The black dashed line represents the lab model.

From Fig. 5.1 it is clear that the skirts affect the rigid body motions, where the the skirts significantly reduced the pitch motion compared to the model without any skirts. The natural period in heave increases, which is a result of the additional added mass effects in heave from the skirts. The surge motion is also slightly influenced, and the resonance peaks occurs at higher periods.

The viscous loads from flow separation around the edges of the skirts will introduce considerable damping effects that are not captured by WAMIT, and the difference can be seen from the comparison to the experimental results in Ch. 6.

5.2 Draught sensitivity

The results from the draught sensitivity analyses are presented in this section. The effect of the draught on the body motions and free surface elevation, was conducted due to the notably different pitch motions displayed by the foundation, compared to pitch motion obtained by Moreau et al. [17] and the results by Sevan. The surge, heave and pitch RAOs from this study are presented in Fig. 5.2.

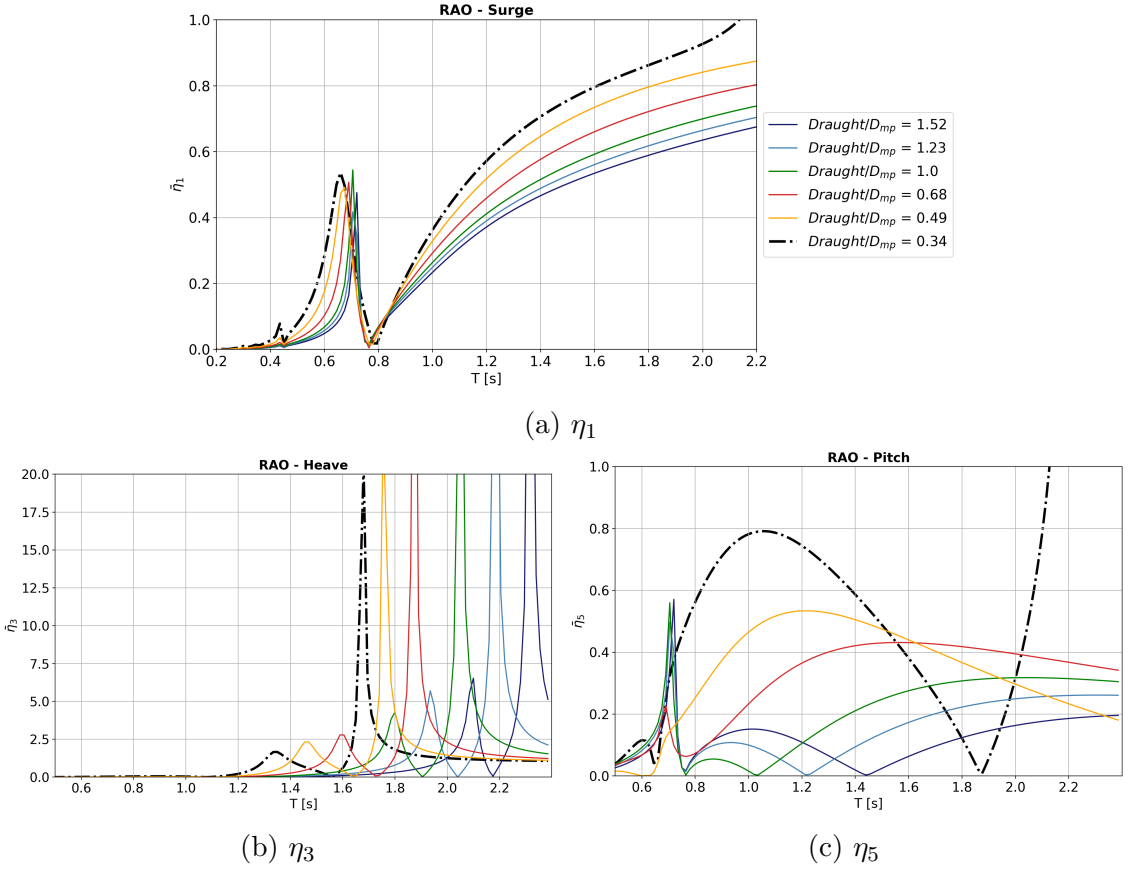

(a) η_1

(b) η_3

(c) η_5

Figure 5.2: Surge (a), heave (b) and pitch (c) RAOs obtained from the draught study where the models are presented buy the ration $Draught/D_{mp}$. The black dashed lines represents the lab model. The draught show a significant impact on the responses, by shifting the heave resonance and reducing the pitch motion.

The pitch RAOs displays a considerable change with the increase in draught, shown in Fig. 5.2(c). The black dashed line has a distinct curvy peak, reaching up to 0.8, whereas the same shape can not be observed for the deeper models. The pitch motion appears to subside with the increasing draught until the draught is equal to the moonpool diameter. When the draught continues to increase beyond the moonpool diameter, the pitch motion actually increases again as shown by the dark blue and light blue lines. The pitch motion found by Moreau et al. [17] for the deeper

floating cylindrical dock is shown in Fig. 5.3, where the pitch and surge motion is plotted against the non-dimensional frequency $\omega^2\sqrt{b/g}$. Despite the difference in x-axis values, the motions are possible to compare, and the peaks can be identified in both plots. The deep cylinder model shown in Fig. 5.1 and the deeper models presented in Fig. 5.2, display the same sharp peak and cancellation in surge and pitch, and generally follow the same shape better.

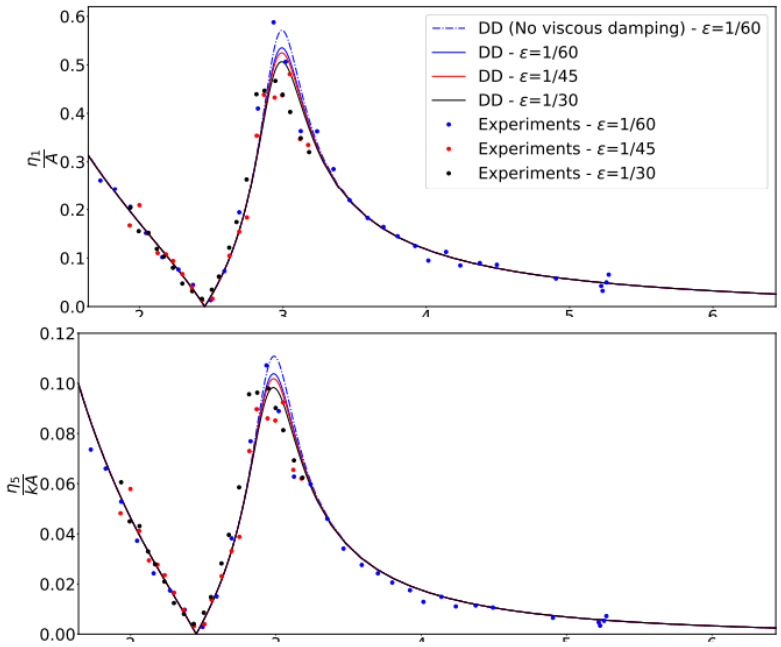

Figure 5.3: Surge and pitch RAO from Moreau et al. [17], where a deeper cylindrical hull with outer skirts was investigated. The RAOs are plotted against the nondimensional frequency $\omega^2\sqrt{b/g}$.

The trend displayed by the draught changes was also found by another master student, Borgar Larsen, investigating the Sevan SWACH wind concept, where a model experiment was conducted using a 2D cross-section of the cylindrical hull [30]. The results from the draught sensitivity study for surge and pitch, from his not yet published master thesis, have been included here for comparison, as shown in Fig. 5.4, where the results demonstrate the same pattern as displayed in Fig. 5.2, and the response from the deeper models correlate better with the results found by Moreau et al. [17].

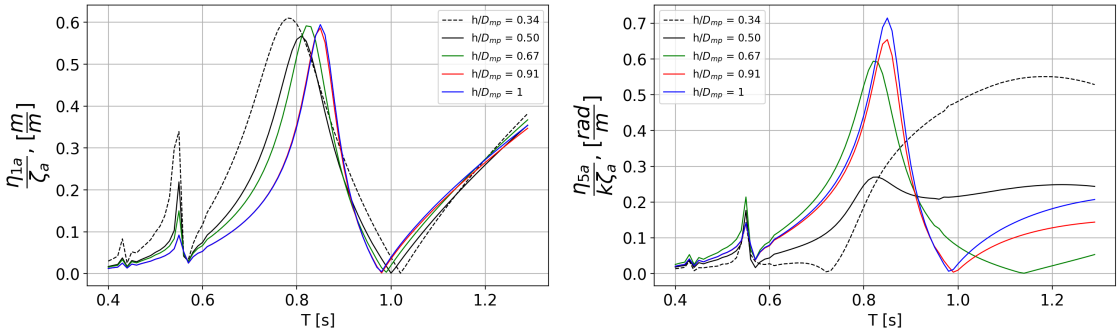

(a) η_1 (b) η_1

Figure 5.4: Surge (a) and heave (b) RAOs from Larsen's draught study from his non-publised Master thesis[30].

Thus, the pitch motion displayed by Sevan concept appears to be significantly affected by the draught and the skirt effects.

The free surface elevation inside the moonpool was expected to be altered by the draught changes, and from the figures in Fig. 5.5, the effects are noticeable.

The first peak form the point corresponding to 0° represents the first transverse sloshing mode, and the increases in draught slightly increases the 1^{st} natural sloshing period, differentiated by the slight changes in peak values. The second peak represent the piston mode resonance, and the shift in this frequency is much more prominent. The deepest model given by $Draught/D_{mpo} = 1.52$ has a piston mode frequency approximately one second higher than the original lab model. These changes in piston mode frequency correlates with the changes in heave, shown in Fig. 5.2 (b).

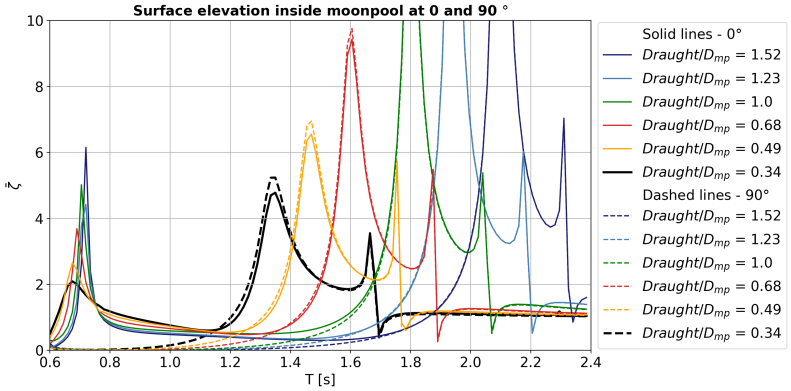

(a) ζ_{mp} *at* $0°$ *and* $90°$

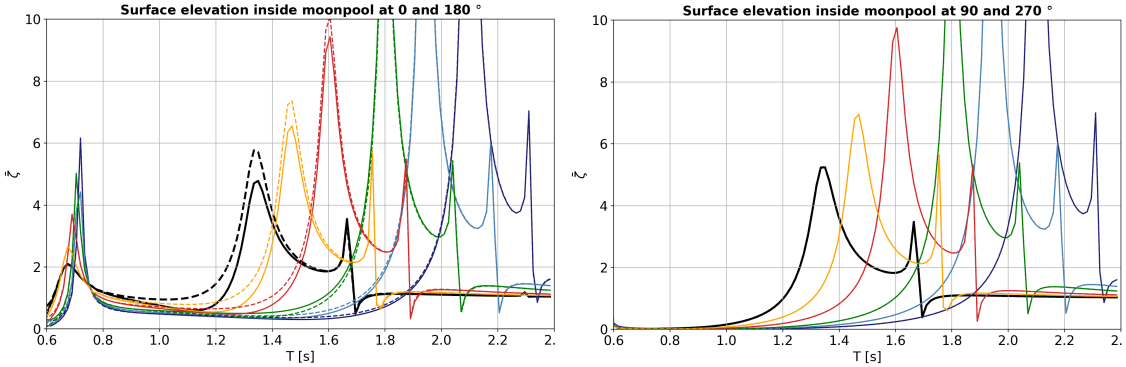

(b) ζ_{mp} *at* $0°$ (Solid lines) and at $180°$ (Dashed lines)

(c) ζ_{mp} *at* $90°$ (Solid lines) and at $270°$ (Dashed lines)

Figure 5.5: Surface elevation inside the moonpool from the draught sensitivity study, where the results are presented using the ratio $Draught/D_{mp}$. The black lines represent the numerical results from the lab model.

5.3 Numerical replicas of experiment

The goal of the numerical analyses was to replicate the experiment to the best extent, and the results from these analyses are presented in this section. Fig. 5.6 shows the surge, heave and pitch RAOs for the replicated analyses described in Sec. 3.1.3.

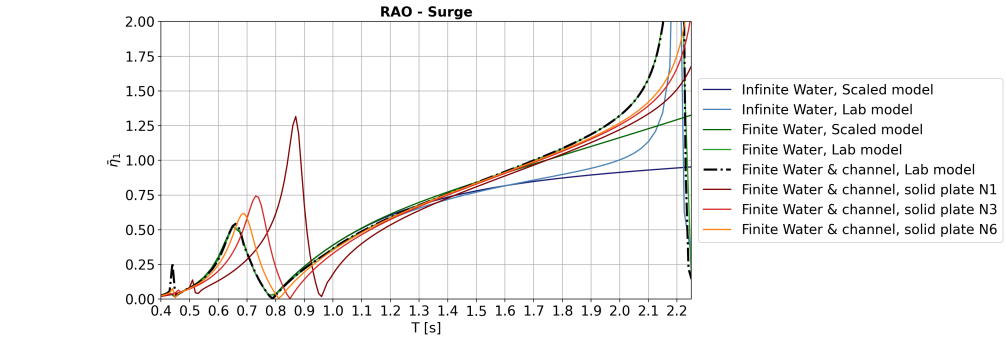

(a)

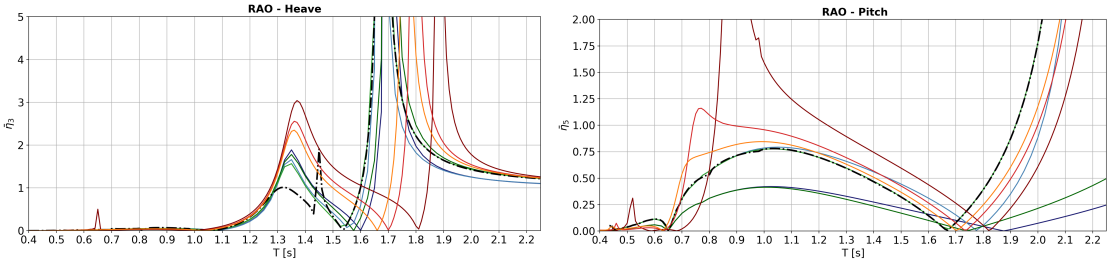

(b) (c)

Figure 5.6: Surge, heave and pitch RAOs from analyses in WAMIT using infinite water depth, finite water depth of 0.8 m and a 2.5 m wide channel. Both the lab model and scaled model have been included, in addition models with a solid baffle at position N1, N3 and N6 have been added to capture the added mass effect introduced by these. The results are given by the model scale periods.

In WAMIT there is an option to include channel walls, and this option was implemented to try and capture the channel wall reflections. The channel wall reflections have the largest impact on the heave motion, corresponding to the results shown in Fig. 5.6, where the channel wall effects can be seen from the black dashed line in plot (b). A little after 1.4 s, there is a significant dip in the heave motion, before a sharp peak. This peak can not be seen for the results with the solid plate modelled, and the model could be less affected by the reflections with the solid plates. The peak could also be a result of a numerical singularity.

The heave motion also differs between the various analyses, and for the peak corresponding to the first piston mode at around 1.35 s, the magnitude varies with the water depth and the baffle positions. Furthermore, both the water depth and baffles change the cancellation period in heave, and contribute to a shift in the natural periods seen from the concealed peaks between 1.65 s and 1.9 s. The baffles introduce an additional added mass effect, which subsequently increases the natural period.

The difference in surge motion between the infinite water depth and the finite for

both the lab model and scaled model are almost non-existing. A small deviation can only be seen for higher wave periods, where the motion increases slightly more for the finite water depth results. The difference between the surge motion with and without the solid baffles are more evident, and the peak and cancellation period in surge both increases in magnitude and shifts towards higher periods with shallower baffle positions, in accordance with [17].

From the surge and heave RAOs, there has been negligible differences in the results between the lab model and the scaled Sevan model. For pitch on the other hand, there is a significant difference, and the pitch motion displayed by the scaled model, dark green line, exhibit a more similar pattern as the deeper models shown in Fig. 5.2, despite having the same draught as the lab model.

This difference was not expected to be that noteworthy, and the reason for this deviation have been hypothesised to be a result of different moments of inertia (I_{55}). Moreover, the mass and vcg differs between these two models, which again can have an impact on the pitch motion. The difference between these two models were found to be more noteworthy than initially thought, but the disparities in the numerical results will not influence the possibility of evaluating the effect of the baffles experimentally. Furthermore the same trend with the solid baffles seen from the surge and heave RAOs is visible in the pitch RAO, where the modelled solid baffle at N1 results in the largest pitch motion. This large increase in pitch for the plate modelled at N1 is slightly conspicuous, but through the investigation of the channel walls neither this effect was possible to find an apparent reason for.

5.4 Added mass and damping coefficients

The added mass and damping coefficients in surge, heave and pitch have been obtained from WAMIT, and they are presented in Fig. 5.7. In addition the coupled surge and pitch added mass and damping coefficient have been plotted, as shown in Fig. 5.8.

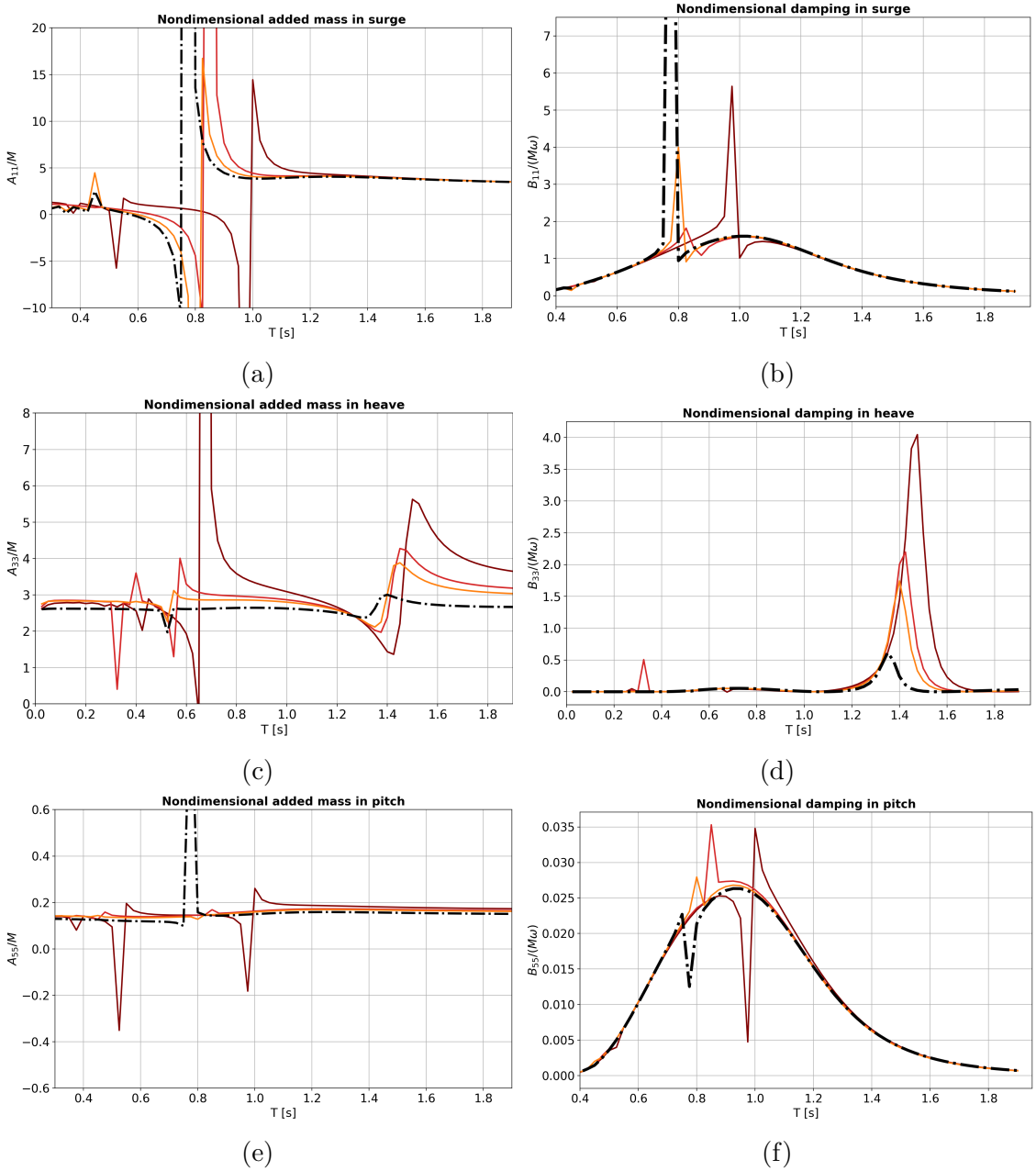

Figure 5.7: Non-dimensional added mass in surge, heave and pitch for the lab model and the models with a solid plate at N1, N3 and N6. The results are given by the model scale periods.

The changes in added mass for surge, heave and pitch substantiates the RAOs, where the added mass changes with the solid baffle and its position. The changes are again more evident for the baffle at the shallowest position N1, and in heave, where the possibility of the plate rising above the free surface is likely, the plate results in larger fluctuations. Furthermore the piston mode can be identified by the added mass in heave, as described in Sec. 2.7, where the minimums around 1.4 s displayed in Fig. 5.7 (c) corresponds to the piston mode seen seen in the heave RAO

in Fig. 5.6. The piston mode have also been detected by plotting the free surface elevation inside the moonpool, which can be seen in Fig. 5.9.

The damping in heave also increases with the ascendance of the plates, and the largest damping can be seen for the model with the baffle at position N1. The surge and pitch added mass and damping display some of the same patterns, where the peak and through values seen for the added mass coincides. The damping display the same curve, with the highest value around 1.0 s, and the correlations displayed contribute to show the importance of the surge and pitch coupling for this structure.

Due to the structures symmetrical geometry, the relation $A_{15} = A_{51}$, shown in Sec. 2.3 apply here. Thus, only the added mass and damping are shown for A_{15} in Fig. 5.8

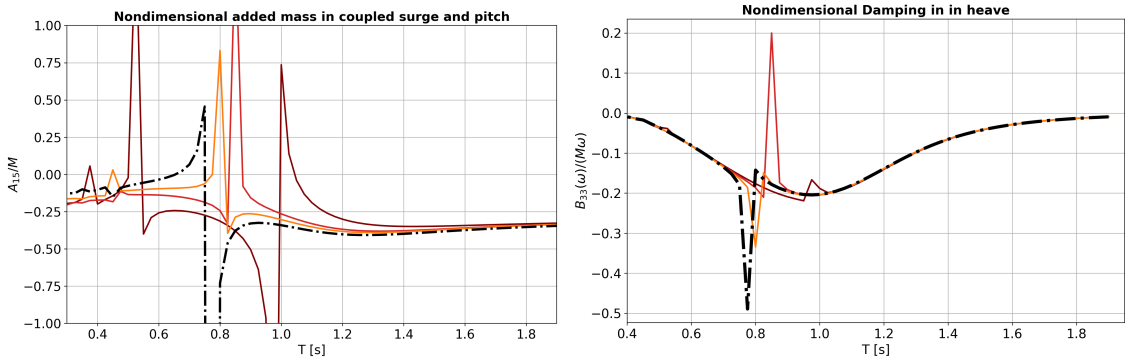

(a) (b)

Figure 5.8: Non-dimensional added mass in coupled surge and pitch for the lab model and the models with a solid plate at N1, N3 and N6. The results are given by the model scale periods.

From the added mass displayed in Fig. 5.8 (a), A_{15} is around the same magnitude as A_{55}, and display the same pattern as the surge and pitch added mass, demonstrating the anticipated coupling effects. The coupled damping is negative, which again shows how the coupling might increase the response of the structure.

5.5 Free surface elevation

The free surface elevation inside the moonpool have been plotted using field points from WAMIT, where each of the points coincide with the same coordinates as the wave tapes placed inside the moonpool in the experiment. In addition, a field point created at the centre of the structure. Fig. 5.9 presents the free surface elevation for

the model without any baffles (a), and the solid baffle modelled at N1 (b), N3 (c), and N6 (d) respectively.

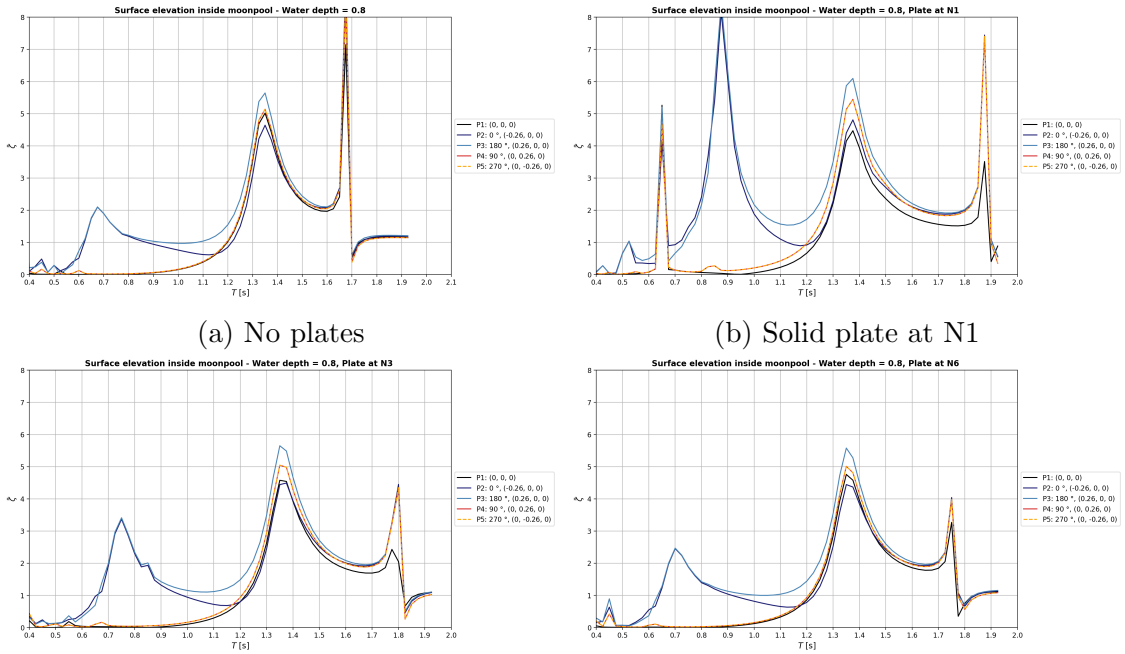

(a) No plates

(b) Solid plate at N1

(c) Solid plate at N3

(d) Solid plate at N1

Figure 5.9: Surface elevation from inside the model given in an earth fixed coordinate system, with P2-P5 providing measurements along the moonpool walls, and point P1 at the centre of the moonpool. Fig. (a) shows the surface elevation for the lab model without ant baffles at a finite water depth. Fig (b) - (d) shows the surface elevation with a solid baffle modelled at position N1, N3 and N6. The results are given by the model scale periods.

From Fig. 5.9 both the first transverse sloshing mode and the piston mode can be identified, where the first sloshing mode occur between 0.65 s and 0.85 s depending on the position of the baffle. The sloshing mode is shown by the peaks in elevation for points at 0° and 180°, given by the blue lines. In addition to the peak displayed by the blue lines, an extra peak can be seen at around 0.65 s for the plate at N1, where the rise in the free surface elevation is the same for all the points. This peak could be a result of another sloshing mode which have been shifted due to the presence of the plate, or a results of a numerical singularity. Nonetheless, the expected shift in the sloshing frequency were found, with the largest effect displayed for the shallowest baffle, corresponding to the findings presented in Sec. 1.2. Furthermore, the first transverse sloshing mode can be linked to the peak and cancellation period in surge, shown in Fig. 5.6 (a).

The piston mode occurs around 1.35, where the free surface elevation inside the

moonpool at this period is approximately the same for all the five point used. The field point from the centre verify the piston mode motion captured by the points along the moonpool walls.

CHAPTER 6

Results and discussion

In this chapter the results from the experiments are presented and discussed. In addition some of the results from the numerical analyses have been included for comparison, where the analysis using finite water depth and channel walls have been used. The experimental results are all presented in model scale, and as a result of the chosen scaling factor of $\Lambda = 100$, the transformation to full scale periods are easily done by following the relation $T_{FS} = \sqrt{\Lambda} T_{MS} = 10 T_{MS}$, where the subscripts *FS* and *MS* denotes full scale and model scale respectively. During this chapter the reader should be aware that the terms RAOs and transfer functions have been interchanged to create a better flow in the text. The term refers to the same concepts, given by the relations presented in Sec. 2.4.1.

Firstly the regular wave results are presented through RAOs of the rigid body motions and free surface elevation. Secondly, the irregular wave results are given by the transfer functions for each sea state, before a short comparison of the regular and irregular RAOS are given.

In addition comments or remarks to other aspects either observed, measured or calculated from the experiments are presented in this chapter.

6.1 Regular wave results

In Fig. 6.1 the surge, heave and pitch RAOs from the experiments have been computed, and plotted together with the numerical replica.

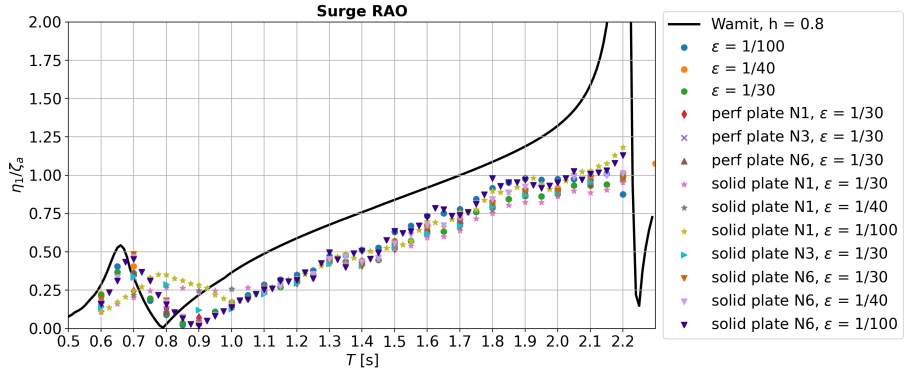

(a) η_1/ζ_a

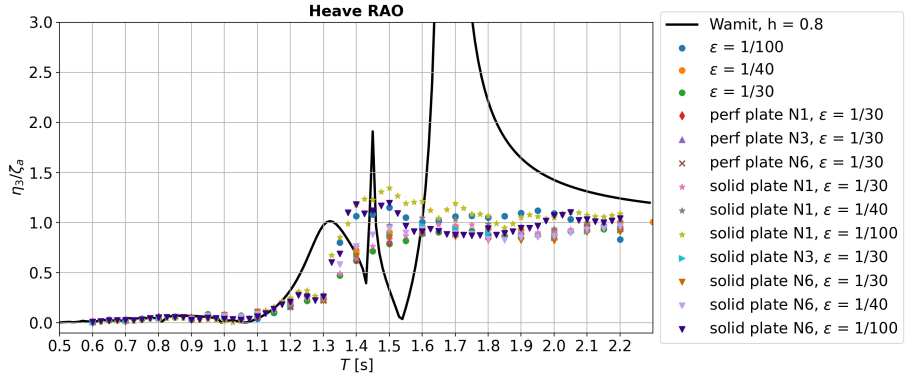

(b) η_3/ζ_a

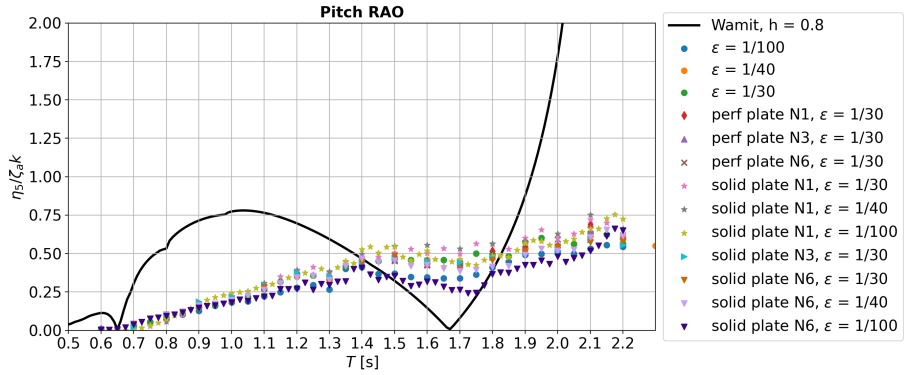

(c) η_5/ζ_a

Figure 6.1: Experimental RAOs plotted together with the numerical result from WAMIT using finite water depth of 0.8 m and a channel with width of 2.5 m. All the experimental results are shown with different markers, where the same plate configurations have the same marker. The numerical results generally overestimates the response compared to the experimental, and the numerical slightly differs from the experimental.

The peak and cancellation periods in surge from WAMIT do not coincide with the the experimental runs as expected. However, the numerical and experimental results follow the same pattern, and the general trend is that WAMIT slightly overestimates the motion, whilst missing the peak and cancellation periods by around 1 s. The results shown by the run $\epsilon = 1/100$ and the solid baffle at position N1, shown by the green stars in Fig. 6.1, diverge the most from the other results around the peak and cancellation periods. The periods are slightly shifted, drawing a parallel to the change in the first transverse sloshing mode frequency, and the results found by Moreau et. al [17]. Thus, by only looking at the surge motion ,the solid plate at N1 appears to affect the rigid body motion in a positive way.

From the heave RAO, the numerical and experimental results coincides well for periods up to around 1.1 s, and again when the RAO converge towards one for the higher wave periods around 2.0 s. The large discrepancy between WAMIT and the experimental around the resonance peak demonstrate how the viscous damping for this structure is paramount, and how the potential flow theory overestimate the motions around the resonance peak. Moreover, around 1.4 - 1.5 s a slight peak in the measured heave motion is visible, which corresponds to the first piston mode. However, neither the first transverse sloshing mode nor the piston mode from the experimental runs corresponds to the periods found in WAMIT.

Another interesting aspect shown by the heave RAO is the slight dip seen at 1.3 s, which does not correspond to the dip found from the numerical analyses with tank walls in WAMIT. Since the numerical and experimental results do not fully coincides as expected, the dip could still be a result of tank wall reflections, however this is only speculations and should be further investigated.

Both the surge and heave motion do in general correlate better with the WAMIT results than the pitch motion, shown in Fig. 6.1 (c). The expected correspondence Moreau et al. [17] found between their experiment and numerical analyses were expected here as well, but the WAMIT results appear to overestimate the response. The non-linear damping introduced from the skirts and baffles are not captured by WAMIT, and these effects could explain the lower pitch response. Nonetheless, the pitch motion measured have been found to correlate with the results provided from the 2D-experiment by Larsen [30], where his results shown in Fig. 6.2[30], validates the measured pitch response, given in Fig. 6.1 (c). In addition, in Sec. 4.4 the possible influence from the electrical cables on the pitch motions were shortly discussed, and this could also have been a contributor to the difference.

Lastly, the improvement of the surge motion with the solid baffle at position N1, were not seen for neither the heave nor the pitch motion, where the plate instead resulted in larger responses compared to the model without any baffles.

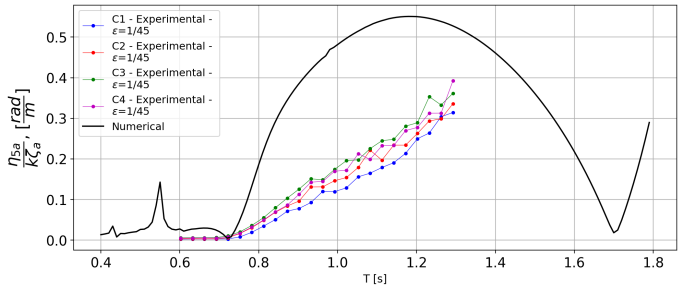

Figure 6.2: Numerical and experimental pitch RAOs from the two-dimensional experiment of the SWACH concept, found and computed by B. Larsen [30]

To better show the effect of the baffles, the RAOs for the cases with solid and perforated baffles have been plotted with the solid plate results from WAMIT. These figures are displayed in Fig. 6.3.

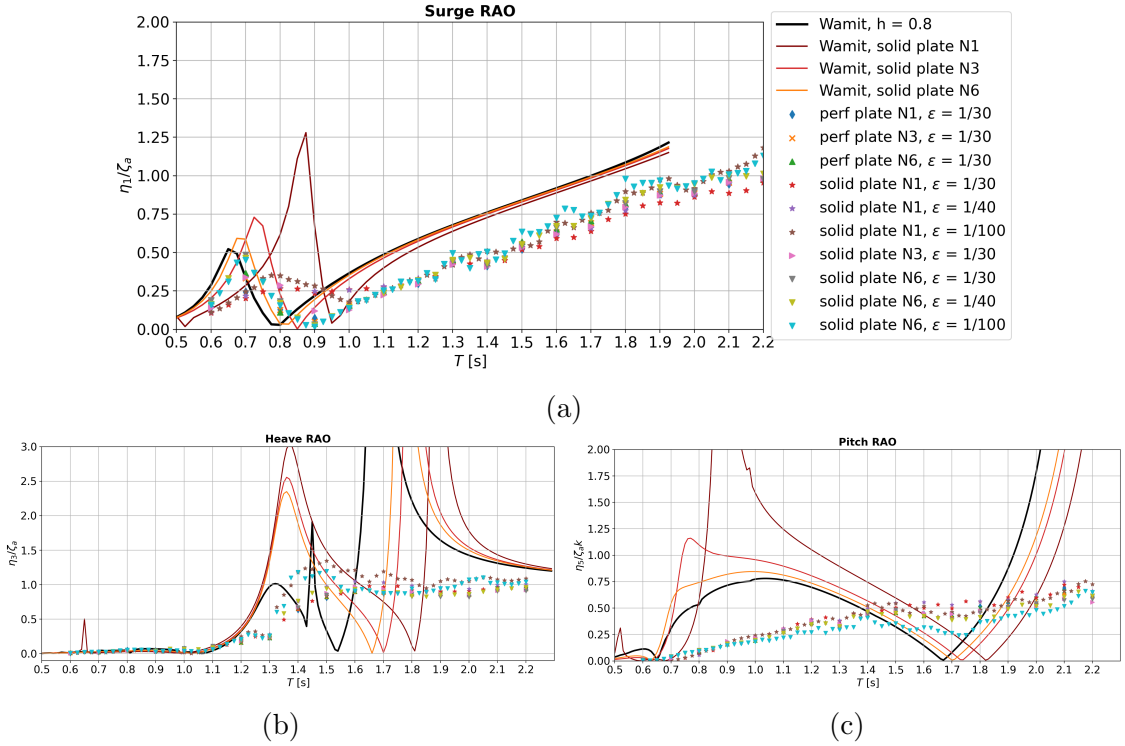

Figure 6.3

In Sec. B.1, RAOs presenting the results for each of the positions N1, N3 and N6 can be found.

6.1.1 Free surface elevation

In Fig. 6.4 the measured free surface elevation, given by the earth fixed coordinate system, has been presented for a wave test without any baffles and $\epsilon = 1/30$. Around 0.7 s there is a peak detected as the first transverse sloshing mode, and round 1.4 - 1.5 s the piston mode can be seen, corresponding to heave motion in Fig. 6.1 (b). For the rest of the figures showing the free surface elevations, the abbreviation WP will be used for the wave tapes at the given points inside the moonpool, where the positions were specified in Sec. 4.1.

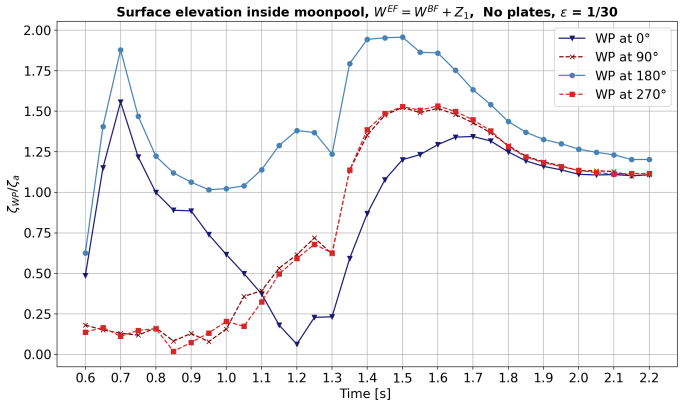

Figure 6.4: Free surface elevation measured from the four wave tapes at 0°, 90°, 180°, 270° inside the moonpool, for $\epsilon = 1/30$, and with no baffles.

From WP 180°, the surface elevation appears to be a bit more prominent than the measurements from 0°, coinciding with the findings from the numerical free surface elevations. Thus, WP 180° and 270° have been chosen for the comparison of the free surface elevation, where the measurements from WP180 are shown in shades of blue, and WP270 in shades of red. Plots showing for 0° and 90° can be found in App. B.2.

The steepest waves resulted in the largest free surface elevations, and have been used for the comparison.

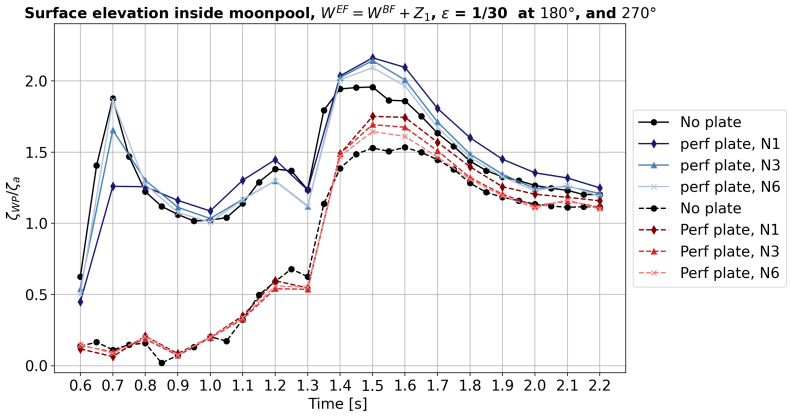

(a) Perforated plates, $\epsilon = 1/30$

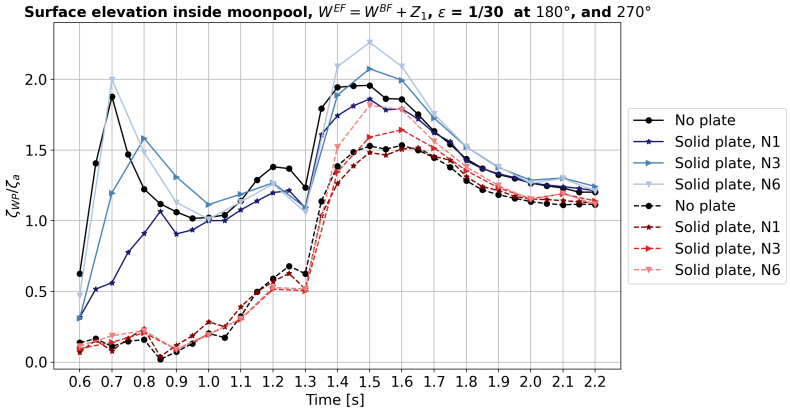

(b) Solid plates, $\epsilon = 1/30$

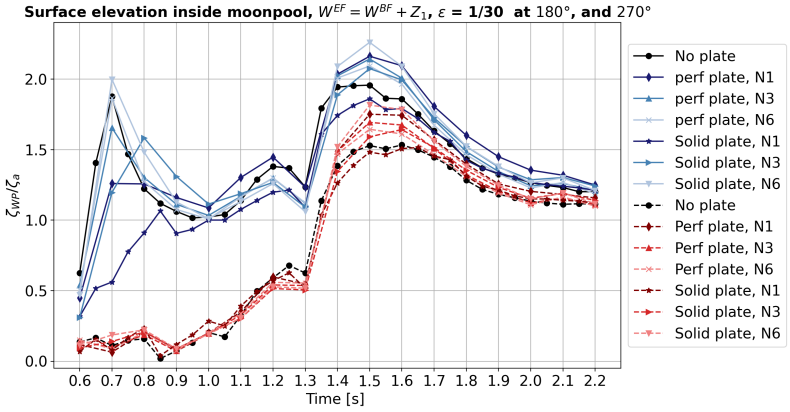

(c) Perforated and solid plates, $\epsilon = 1/30$

Figure 6.5: Free surface elevation measured at 180° and 270° where 180° are given by the blue shades and 270° are given by the red shades. (a) shows the free surface elevation for the perforated plate at the three positions N1, N3, and N6, and no plates, (b) the results for the solid plate configurations and no plates, and (c) shows the combination of (a) and (b). The measurements are from wave tests with $\epsilon = 1/30$.

From Fig. 6.5, the shift in the first sloshing mode for the plate at N1 can be seen from the surface elevation from both Fig. 6.5 (b) and (c), where the peak has been

shifted towards 0.85 s, and is evidently reduced compared to the case without any plates. In addition, the solid plate at N3 appears to introduce a slight change in this motion as well, where the peak magnitude is reduced, and the peak is shifted to 0.8 s.

The piston mode appears to have its highest peak at 1.5 s for all the cases, and a generally larger motion for the periods between 1.4 s and 1.6. In addition, the free surface elevation is generally larger at 180° compared to the measurements from 270°. For periods above 1.8 s the free surface elevation converges towards one, but still shows a slight amplification compared to the incident waves.

The free surface elevation plots corroborate the findings displayed in the RAOs, and the changes to the sloshing periods correlates with the theory presented by Moreau et al. [17]. In addition, the correlation between the rigid body motions and the free surface elevation further shows how the moonpool affects the rigid body motions, in accordance with [13].

In Fig. 6.6 the 1^{st} transverse sloshing mode has been shown for the model without any baffles (a) and (b), and for the case with the solid baffle at N1 (c) and (d). The wave crests and troughs inside the moonpool have been marked in red in an attempt to better show the differences. The wave crest without any baffles reaches higher compared to the crest seen in (c) with the solid baffle at N1, corresponding to the findings presented in Fig. 6.5. The distinct 1^{st} transverse sloshing motions are also more prominent for the case without the baffles, and the disturbances in the free surface seen in (c) and (d) can be linked to flow separation around the edges of the plate.

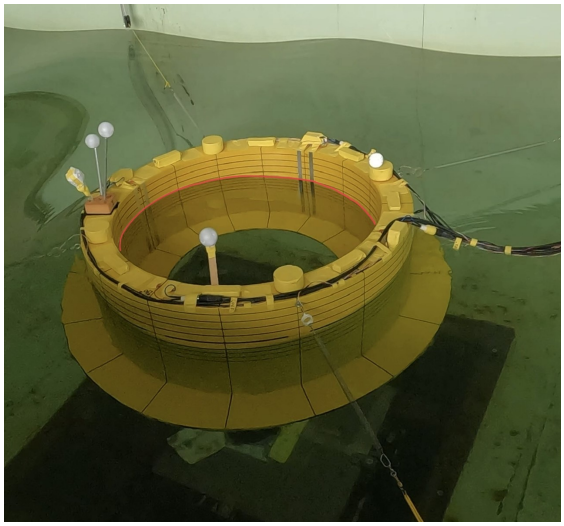

(a) Wave crest at 0° without any plates, T = 0.7 s

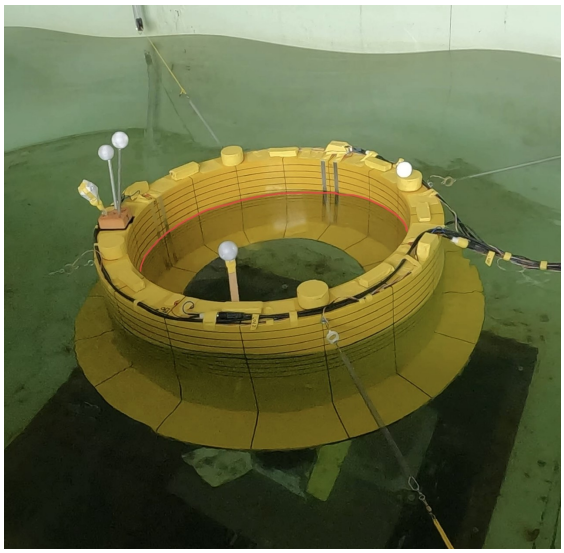

(b) Wave trough at 0° without any plates, T = 0.7 s

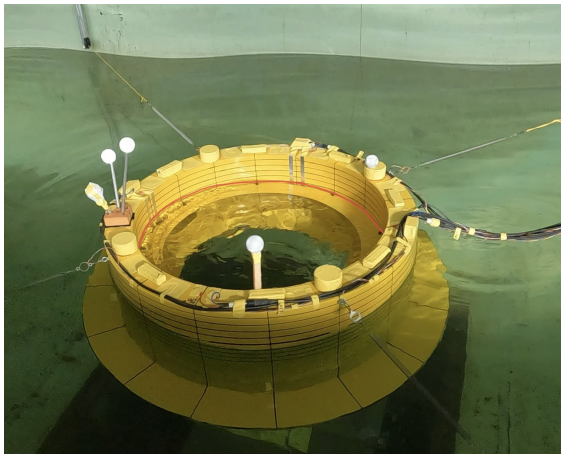

(c) Wave crest at 0° for the solid plate at N1, T = 0.8 s

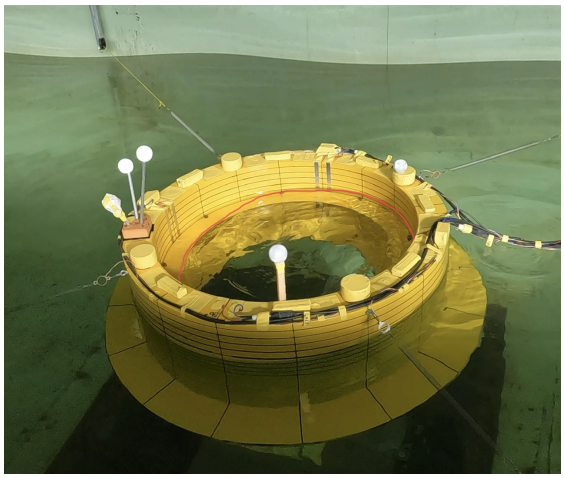

(d) Wave trough at 0° for the solid plate at N1, T = 0.8 s

Figure 6.6: Photos showing the 1^{st} transverse sloshing modes, where (a) and (b) shows the wave crest and wave through for the model without any plates, and (c) and (d) for the case with the solid baffle at N1. The wave crest and trough are visibly smaller for the case with the plate at N1. The photos are taken from the wave tests with $\epsilon = 1/30$

In Fig. 6.7 what appears to be secondary resonance excited by the 1^{st} transverse sloshing mode at T = 0.7 s, Sec. 2.8, have been attempted visualised by the red marks. The non-linear liquid motion is only present at the centre of the moonpool, and are occurring at the same times as the transverse sloshing mode occurs. The pictures are included to show how the non-linear effects can affect the motions, and amplify the importance of experiments where these effects can be seen and studied.

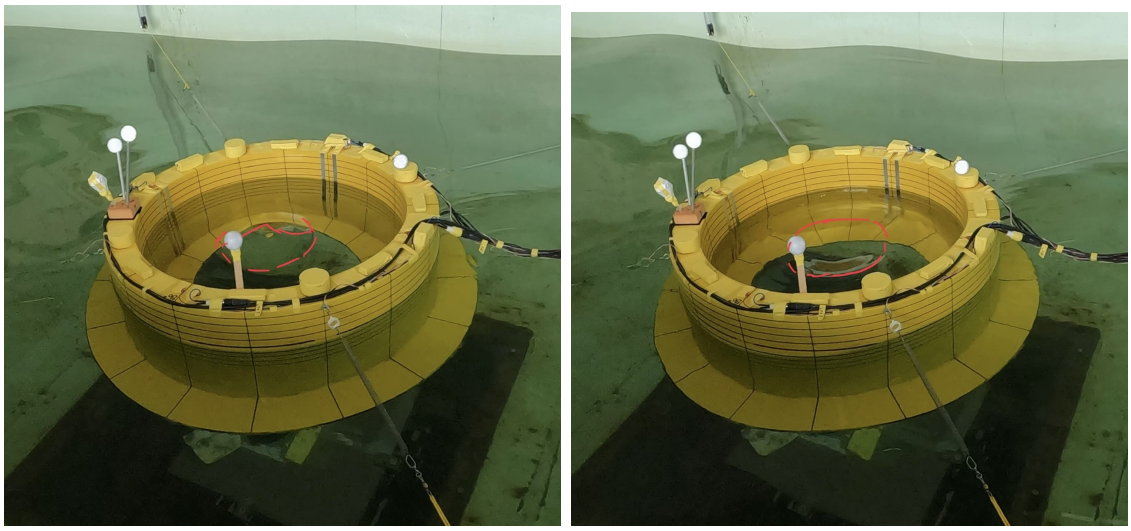

(a) Non-linear peak (b) Non-linear dip

Figure 6.7: Photos showing what appear to be non-linear secondary resonance, excited by the 1^{st} transverse sloshing mode at T = 0.7 s for the model without any plates. The small peak (a) and dip (b) are tried illustrated by the red marks.

6.2 Irregular sea states

The irregular sea states executed were presented in Sec. 4.3, and in this section the RAOs for some of the sea states have been included. For each sea state the different cases are plotted together to investigate the effects from the baffles at the tested positions.

6.2.1 RAOs

The RAOs have been shown here for the three most extreme sea states tested, where Fig. 6.8 shows the surge, heave and pitch response for a sea state with $Hs = 0.07$ and $Tp = 1.0$. In Fig. 6.9 the results from the sea state with $Hs = 0.08$ and $Tp = 1.2$ are presented, and in Fig. 6.10 the responses are given for the sea state with $Hs = 0.09$ and $Tp = 1.4$, all given by the model scale. In App. C.1 the results from the other sea states specified in Sec. 4.3 are given.

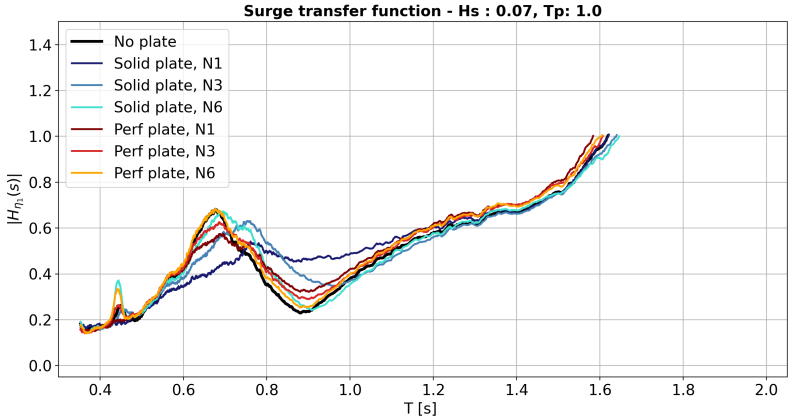

(a) $|H_{\eta 1}(s)|$

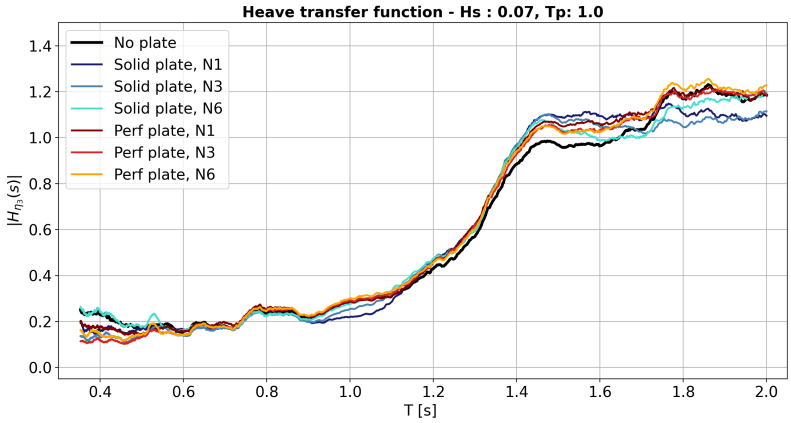

(b) $|H_{\eta 3}(s)|$

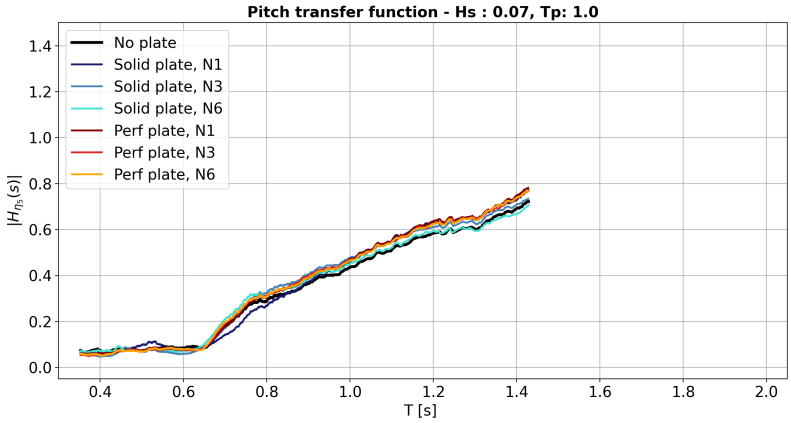

(c) $|H_{\eta 5}(s)|$

Figure 6.8: Computed transfer functions for surge (a), heave (b) and pitch (c) from a sea state with $Hs = 0.07$ and $Tp = 1.0$. The graphs show the results from all the possible baffle configurations tested by the coloured lines, and the model without any baffles are given by the black line.

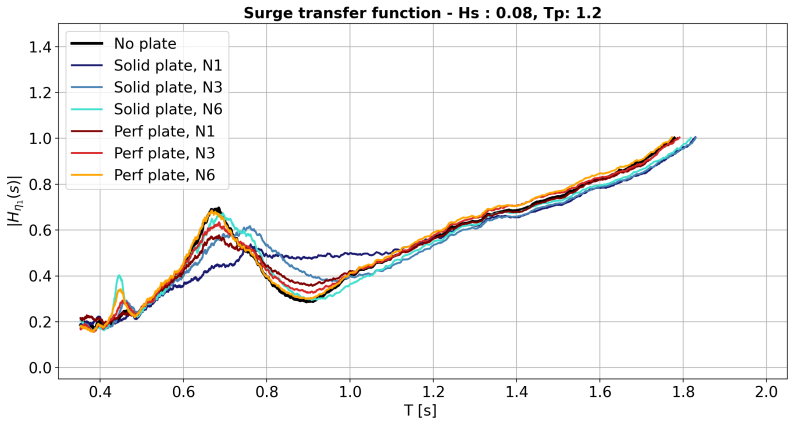

(a) $|H_{\eta 1}(s)|$

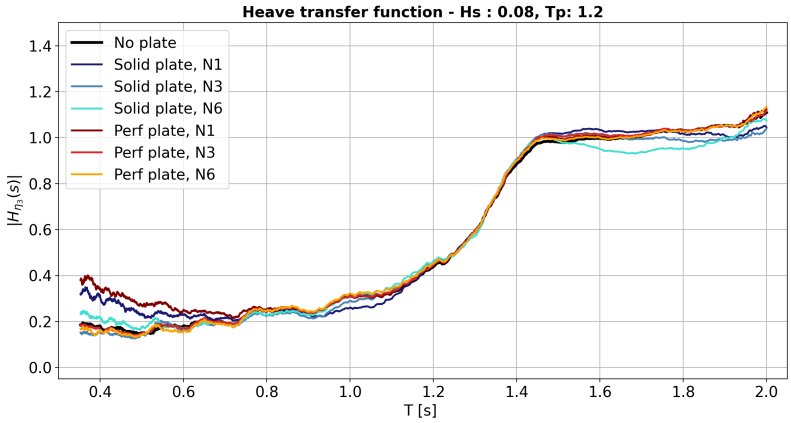

(b) $|H_{\eta 3}(s)|$

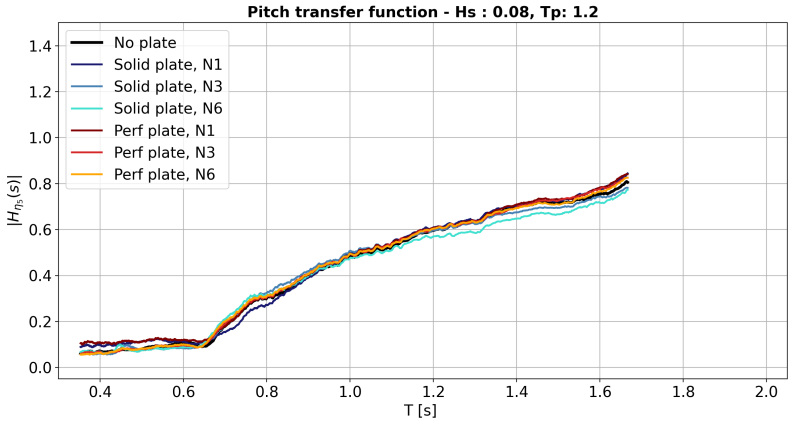

(c) $|H_{\eta 5}(s)|$

Figure 6.9: Computed transfer functions for surge (a), heave (b) and pitch (c) from a sea state with $Hs = 0.08$ and $Tp = 1.2$. The graphs show the results from all the possible baffle configurations tested by the coloured lines, and the model without any baffles are given by the black line.

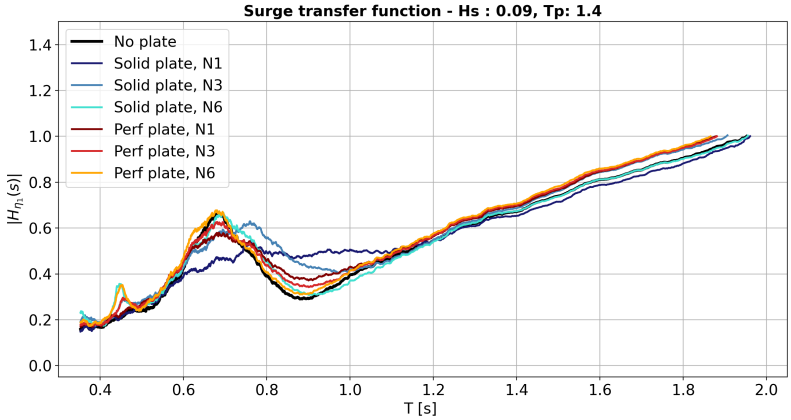

(a) $|H_{\eta 1}(s)|$

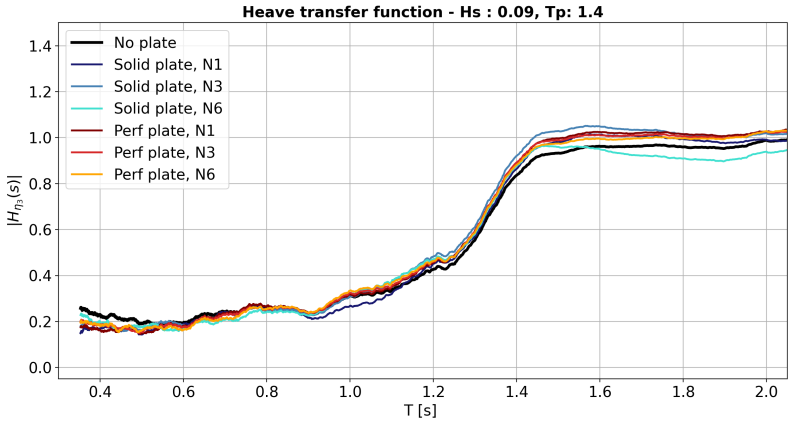

(b) $|H_{\eta 3}(s)|$

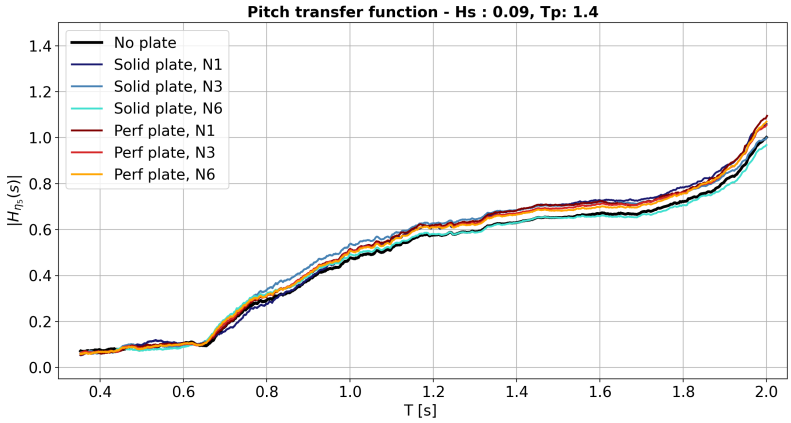

(c) $|H_{\eta 5}(s)|$

Figure 6.10: Computed transfer functions for surge (a), heave (b) and pitch (c) from a sea state with $Hs = 0.09$ and $Tp = 1.4$. The graphs show the results from all the possible baffle configurations tested by the coloured lines, and the model without any baffles are given by the black line.

By looking at the responses from the these sea states, the similarities with the results from the regular wave RAOs are quickly spotted. The irregular responses display the same pattern as found for all the three rigid body motions, and from the

surge responses the change in cancellation and peak periods for the different baffle configurations are recognised here as well. With the irregular sea states, the solid plate at position N1 display the same divergence from the other cases, where the peak and trough values are reduced.

From the heave transfer functions for the various sea states there seem to be some small discrepancies in the response measured for periods below 1.0 s. Afterwards, the response appear to more or less coincide for the different baffle configurations and sea states.

The pitch motion also display the same pattern as shown in the regular RAOs, demonstrating the baffles lack of reducing the pitch response.

Combination RAOs

In this section the irregular RAOs have been plotted together with the regular results for each of the three baffle positions inside the moonpool. The numerical analysis include is a analysis without the channel walls. For the investigation the sea state with $Hs = 0.07$ and $Tp = 1.0$ and $Hs = 0.09$ and $Tp = 1.4$ have been used. In Fig. 6.11 the irregular and regular surge RAOs have been combined, and are given for the two specified sea states and for the three possible baffle positions.

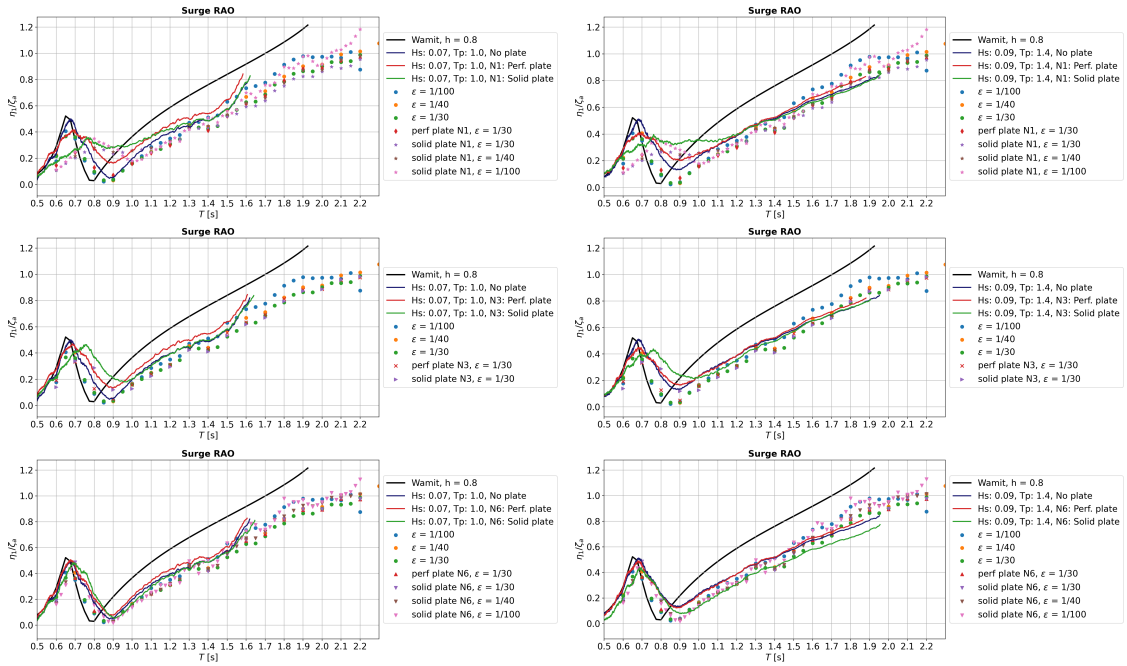

Figure 6.11: Surge RAOs combining the regular and irregular wave results for the sea state with Hs = 0.07 and Tp = 1.0 to the left, and the sea state with Hs = 0.09 and Tp = 1.4 to the right. The RAOs are divided by the baffle positions, with N1, N3 and N6 in descending order, comparing the two baffles at the same position to the case without any baffles.

In Fig. 6.12 the heave RAOs for all the configurations and the two sea states are shown, and in Fig. 6.13 the same results are displayed for pitch.

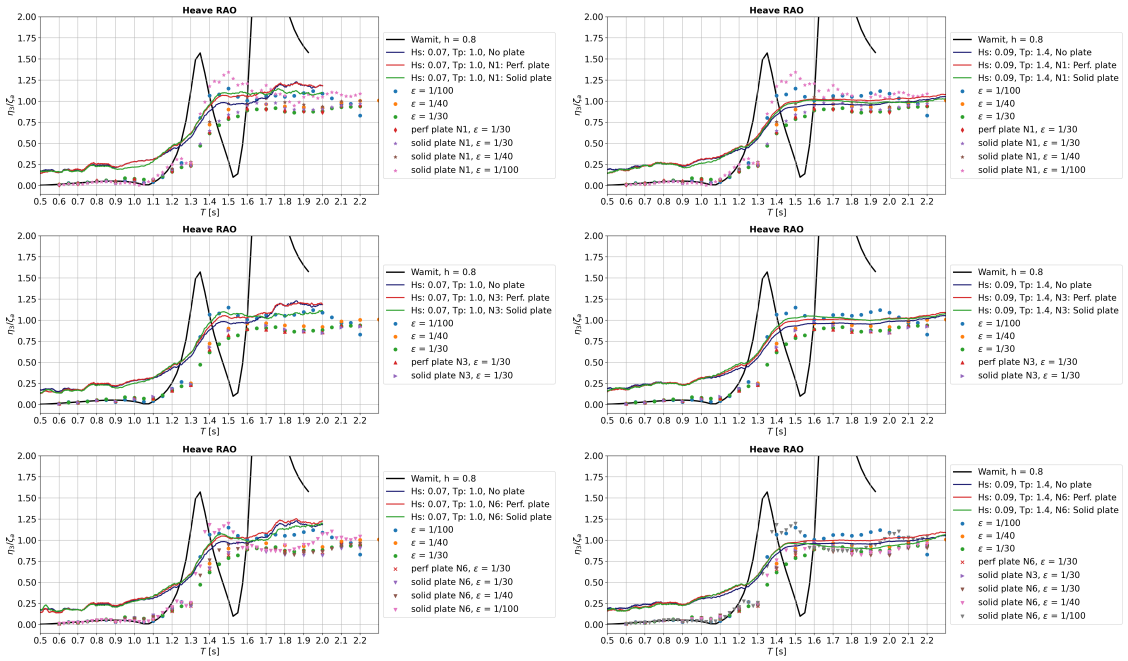

Figure 6.12: Heave RAOs combining the regular and irregular wave results for the sea state with Hs = 0.07 and Tp = 1.0 to the left, and the sea state with Hs = 0.09 and Tp = 1.4 to the right. The RAOs are divided by the baffle positions, with N1, N3 and N6 in descending order, comparing the two baffles at the same position to the case without any baffles.

N1, N3, N6

(a) N1, N3, N6

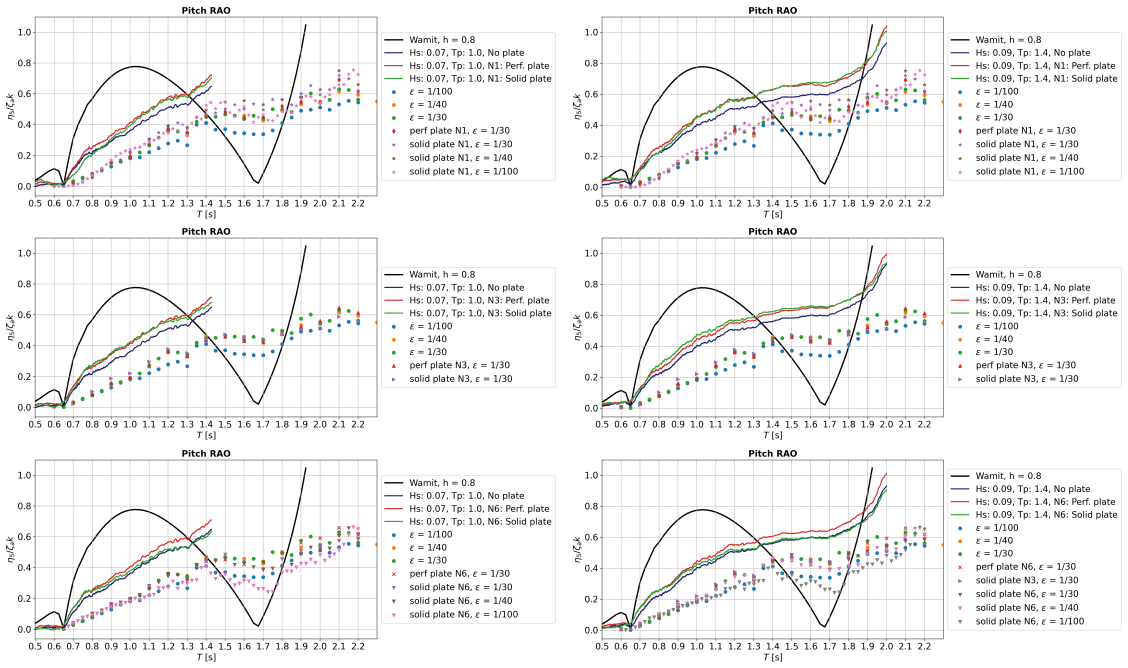

(b) $Hs = 0.07$, $Tp = 1.0$

(c) $Hs = 0.09$, $Tp = 1.4$

Figure 6.13: Pitch RAOs combining the regular and irregular wave results for the sea state with Hs = 0.07 and Tp = 1.0 to the left, and the sea state with Hs = 0.09 and Tp = 1.4 to the right. The RAOs are divided by the baffle positions, with N1, N3 and N6 in descending order, comparing the two baffles at the same position to the case without any baffles.

From these plots a clear correspondence between the regular and irregular RAOs can be seen, where surge and heave motions display the best correspondence. By modifying the surge and pitch RAOs they conformed better with the regular results for the same plate configurations. For heave however, the results agreed better without the modifications for wave periods above 1.4 s, but show an offset compared to the regular RAOs for the periods below.

The discrepancies between the regular and irregular pitch RAOs were greater than expected. However, this difference is likely a result of some non-physical influence such as unfiltered noise from the experiments, some bias error such as the impact from the cable discussed in Sec. 4.4 or some errors in the post-processing that have not been caught. The irregular responses were obtained right before the dead-line, as the process was more time-consuming than first anticipated. Thus, the investigation into these disparities was limited, and a further examination of this is necessary.

Nonetheless, the general trend displayed by both the regular and irregular RAOs is that neither of the two types of baffles alters the response significantly, and that the

effect on the pitch motions were not that consequential as initially hoped.

During the irregular sea state several snap shots and videos were taken of the foundation to evaluate the response. For the sea state with Tp = 1.4 s, the piston mode could be observed several times, and snap shots showing this motion are given in Fig. 6.14. The piston mode can be seen for the tests with the solid plate at N1 (a) and (b), and the perforated plate at N3 in (c) and (d). During the low point of the piston motion in Fig. 6.14 (b), the free surface elevation descend below the plate, showing the magnitude of the motion.

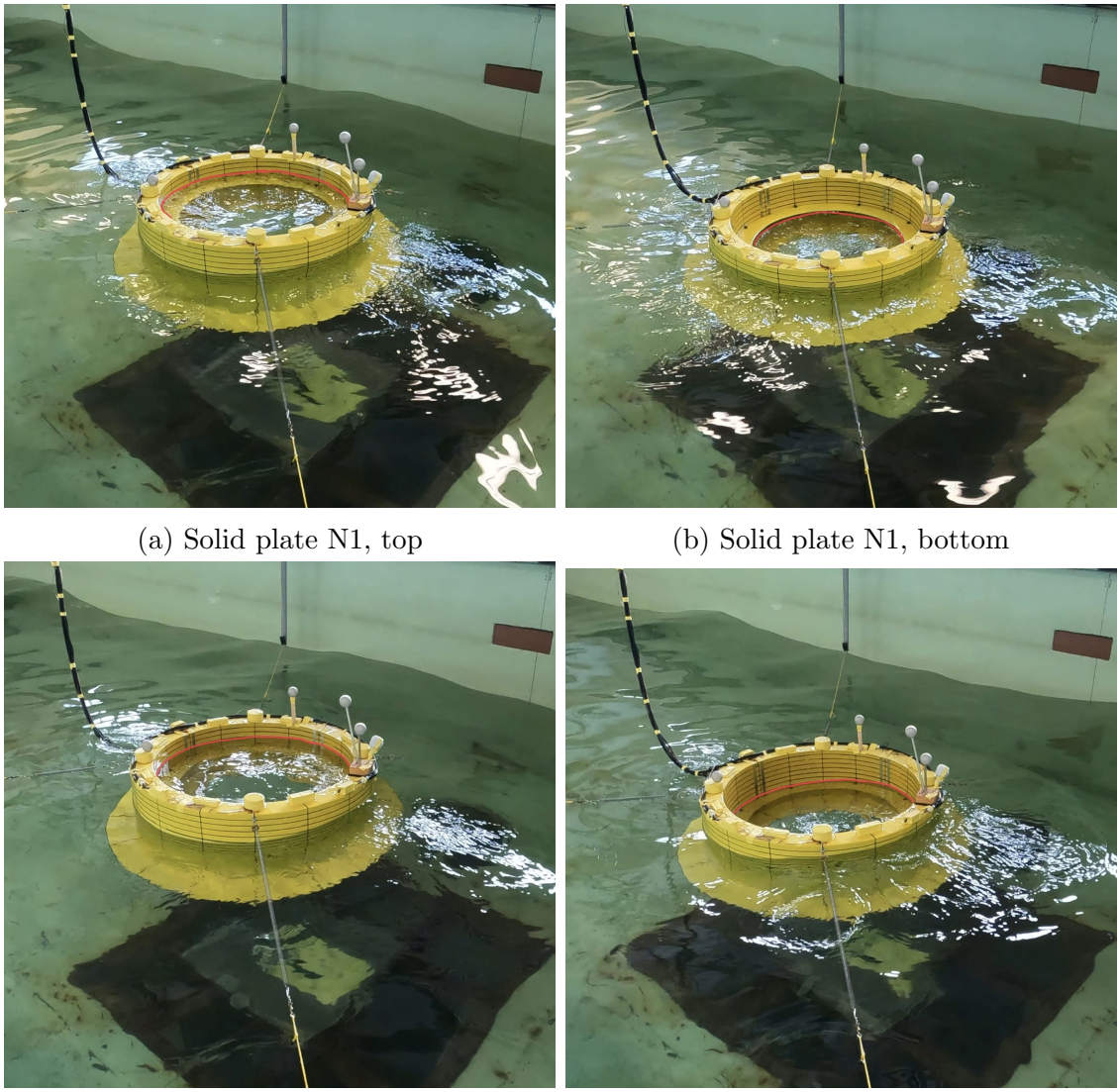

(a) Solid plate N1, top

(b) Solid plate N1, bottom

(c) Perf. plate N3, top

(d) Perf. plate N3, bottom

Figure 6.14: Pictures showing the piston mode, captured from a sea state with $Hs = 0.09m$ and $Tp = 1.4s$. (a) and (b), shows the piston mode for the solid plate at N1, and (c) and (d) the piston mode for the perforated plate at N3.

The disturbances seen in the free surface are results of the flow separations from the

skirts and baffles.

During the harsh sea states with $Hs = 0.09m$ and $Tp = 1.4s$, several waves were of such magnitude that they broke over the structure, shown in Fig. 6.15. These hits were not examined more than visually seeing how the structure handled them, and should be further investigated to see how such breaking waves would impact the wind turbine foundation. The breaking wave results in an internal wave breaking over the rearward end of the moonpool.

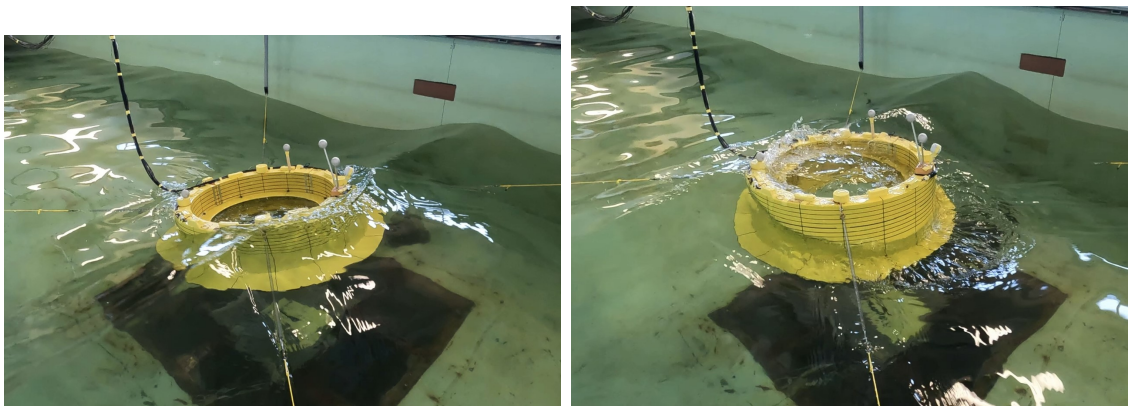

(a) (b)

Figure 6.15: Photos showing a wave breaking over the structure (a), and resulting in an internal wave breaking over the rear of the model.

CHAPTER 7

Conclusions

In this thesis, a floating offshore wind turbine foundation, developed by Sevan SSP, has been investigated. The concept, named SWACH, is a circular cylindrical hull with a moonpool and inner and outer skirts. Both numerical analyses in WAMIT and experiments in the Small Towing Tank (Lilletanken) at NTNU have been conducted. The main goal has been to examine the effects of implementing two different types of baffles on the rigid body motions surge, heave and pitch, where specially a reduction of the pitch motion has been desired. One solid and one perforated baffle, with a perforation ratio of 35 %, have been tested at three different positions within the moonpool. The solid baffles were in addition modelled in WAMIT to capture the added mass effects introduced by the plates, and for comparison to the experimental results. Moreover, both a short investigation into the effects of the skirts and draught were conducted, and the results have been compared to results obtained from Moreau et al. [17] and the work of Larsen, another master student, who has investigated the same concept using a two-dimensional cross-section of the foundation. The comparison to both Moreau et al. and Larsen showed that the experimental results in surge, heave and pitch showed an adequate correlation, and the comparison has been used to validate both the numerical and experimental results presented here.

Sloshing effects can be significant for structure with moonpools, and the first transverse sloshing and piston modes have been identified through the rigid body motions and the free surface elevations inside the moonpool. These periods have also been examined in WAMIT, and even tough they did not coincide exactly, they were found to be around 0.7 s and 1.4 s from both the numerical and experimental results for the model without any plates. The solid baffle at position N1 showed the largest alteration of the 1^{st} sloshing mode, shifting it to approximately 0.85 s, and the al-

teration could be recognised in the surge RAO as well. Moreover, the piston mode could be seen in the heave RAO, showing how the sloshing effects influence the rigid body motions. The regular and irregular transfer functions were also found to concur, and validating the responses obtained. However, some discrepancies were seen, and for pitch, the irregular and regular results showed the largest differences.

Through the comparison, the baffles could be seen to result in some reduction i.e surge, but not without causing an increase in either heave or pitch, or both. Thus, it was concluded that the baffles did not create a substantial decrease in the rigid body motions, specifically in pitch, as hoped.

7.1 Further work

During this thesis, a considerable amount of time has been spent with both the planning and execution of the experiment. In addition, several numerical analyses have been preformed, and not all the aspects initially planned to be examined have been conducted due to the limited time. The post-processing has also been more time-consuming than anticipated, and some of the experimental results desired to investigate have not been actualised. Suggestions for further work have been based on the aspects not investigated now due to the time frame.

No apparent reasons for the discrepancies between WAMIT and the experimental results were found, and for further work a parameter study in WAMIT could be conducted to see if it was possible to make the results coincide. The reason for the offset seen in the irregular results could also be further examined, and the differences between the irregular and regular wave results could be inspected in another experiment.

The implementation of baffles were not as successful as initially hoped, and the effects appeared to be meager. For further work however, more positions closer to the free surface could be interesting to investigate, since the solid baffle at N1 showed an effect on the surge motion and first transverse sloshing mode.

During the experiments a lot of interesting second order effects were witnessed, and were initially planned to investigate further. For further work, the the mean drift motion in surge and the mean drift forces form both model test and WAMIT could be investigated. Lastly, the mooring forces were not examined, and would also have been interesting to inspect.

Bibliography

[1] Paris IEA (2021). *Electricity Market Report - July 2021*. URL: https://www.iea.org/reports/electricity-market-report-july-2021. (accessed: 18.11.2021).

[2] E. Ebbesen and DNV (n.d.). *Floating Offshore Wind - Commercializing with confidence*. URL: https://www.dnv.com/focus-areas/floating-offshore-wind/index.html. (accessed: 10.11.2021).

[3] GWEC - Global Wind Energy Council (n.d.). *Global Offshore Wind Report 2021*. URL: https://gwec.net/global-offshore-wind-report-2021/. (accessed: 02.12.2021).

[4] Sevan SSP (n.d.). *Who we are - Sevan SSP*. URL: https://sevanssp.com/sevan-ssp-who-we-are/. (accessed: 18.11.2021).

[5] — (2021). *Sevan SSP - Master thesis power point*.

[6] B. Molin (2001). 'On the piston and sloshing modes in moonpools'. In: *Journal of Fluid Mechanics* 430, pp. 27–50. DOI: 10.1017/S0022112000002871.

[7] O. M Faltinsen, O. F. Rognebakke and A. N. Timokha (2007). 'Two-dimensional resonant piston-like sloshing in a moonpool'. In: *Journal of Fluid Mechanics* 575, pp. 359–397. DOI: 10.1017/S002211200600440X.

[8] T. Kristiansen and O.M. Faltinsen (2008). 'Application of a vortex tracking method to the piston-like behaviour in a semi-entrained vertical gap'. In: *Applied Ocean Research* 30.1, pp. 1–16. ISSN: 0141-1187. DOI: https://doi.org/10.1016/j.apor.2008.02.003. URL: https://www.sciencedirect.com/science/article/pii/S0141118708000102.

[9] — (2012). 'Gap resonance analyzed by a new domain-decomposition method combining potential and viscous flow DRAFT'. In: *Applied Ocean Research* 34, pp. 198–208. ISSN: 0141-1187. DOI: https://doi.org/10.1016/j.apor.2011.07.001. URL: https://www.sciencedirect.com/science/article/pii/S0141118711000538.

[10] B. Molin (2017). 'On natural modes in moonpools with recesses'. In: *Applied Ocean Research* 67, pp. 1–8. ISSN: 0141-1187. DOI: https://doi.org/10.1016/j.apor.2017.05.010. URL: https://www.sciencedirect.com/science/article/pii/S014111871730202X.

[11] A. G. Fredriksen, T. Kristiansen and O. M. Faltinsen (2015). 'Wave-induced response of a floating two-dimensional body with a moonpool'. In: *Phil. Trans. R. Soc.* 373. ISSN: 2033. DOI: https://doi.org/10.1098/rsta.2014.0109.

[12] S. Ravinthrakumar et al. (2020). 'Coupled vessel and moonpool responses in regular and irregular waves'. In: *Applied Ocean Research* 96, p. 102010. ISSN: 0141-1187. DOI: https://doi.org/10.1016/j.apor.2019.102010. URL: https://www.sciencedirect.com/science/article/pii/S0141118719308132.

[13] L. M. U. Reiersen et al. (2021). 'Investigation of moonpools as pitch motion reducing device'. In: *Applied Ocean Research* 108. ISSN: 0141-1187. DOI: https://doi.org/10.1016/j.apor.2020.102477. URL: https://www.sciencedirect.com/science/article/pii/S0141118720310361.

[14] B. Molin et al. (2018). 'On natural modes in moonpools and gaps in finite depth'. In: *Journal of Fluid Mechanics* 840, pp. 530–554. DOI: 10.1017/jfm.2018.69.

[15] O.M Faltinsen and A. N Timokha (2009). *Sloshing*. Cambridge Ocean Technology series.

[16] W. Wang et al. (2016). 'Liquid sloshing in partly-filled laterally-excited cylindrical tanks equipped with multi baffles'. In: *Applied Ocean Research* 59, pp. 543–563. ISSN: 0141-1187. DOI: https://doi.org/10.1016/j.apor.2016.07.009. URL: https://www.sciencedirect.com/science/article/pii/S0141118716300761.

[17] M. Moreau et al. (2021). 'DRAFT: An upright bottomless vertical cylinder with baffles floating in waves'. PhD thesis.

[18] T. Ikoma et al. (2021). 'Motion characteristics of a barge-type floating vertical-axis wind turbine with moonpools'. In: *Ocean Engineering* 230, p. 109006. ISSN: 0029-8018. DOI: https://doi.org/10.1016/j.oceaneng.2021.109006. URL: https://www.sciencedirect.com/science/article/pii/S0029801821004418.

[19] F. Borisade, T. Choisnet and P. W. Cheng (Sept. 2016). 'Design study and full scale MBS-CFD simulation of the IDEOL floating offshore wind turbine foundation'. In: *Journal of Physics: Conference Series* 753, p. 092002. DOI: 10.1088/1742-6596/753/9/092002.

[20] L. Tan et al. (2021). 'Mean Wave Drift Forces on a Barge-Type Floating Wind Turbine Platform with Moonpools'. In: *Journal of Marine Science and*

Engineering 9.7. ISSN: 2077-1312. DOI: 10.3390/jmse9070709. URL: https://www.mdpi.com/2077-1312/9/7/709.

[21] L. Li et al. (2020). 'Analysis of the coupled dynamic response of an offshore floating multi-purpose platform for the Blue Economy'. In: *Ocean Engineering* 217, p. 107943. ISSN: 0029-8018. DOI: https://doi.org/10.1016/j.oceaneng.2020.107943. URL: https://www.sciencedirect.com/science/article/pii/S0029801820308982.

[22] Z. Jiang et al. (2020). 'Design, modelling, and analysis of a large floating dock for spar floating wind turbine installation'. In: *Marine Structures* 72, p. 102781. ISSN: 0951-8339. DOI: https://doi.org/10.1016/j.marstruc.2020.102781. URL: https://www.sciencedirect.com/science/article/pii/S0951833920300757.

[23] E. E. Bachynski-Polic, T. Kristiansen and D. Myrhaug (2021). *Marine Dynamics Compendium*. Department of Marine Technology, Faculty of Engineering, NTNU.

[24] I. Vries et al. (June 2013). 'Dynamics of Entrapped Water in Large Diameter Turret Moonpools'. In: vol. 1. DOI: 10.1115/OMAE2013-11467.

[25] Inc. Massechusetts Institute of Technology & WAMIT (2020). *WAMIT User Manual, version 7.4*. WAMIT, Inc.

[26] T. Hannasvik (2019). 'Experimental Investigation of Beach Efficiency for Regular Waves'. MA thesis. NTNU.

[27] Qualisys Motion Capture Systems (n.d.). *Applications for motion capture technology*. URL: https://www.qualisys.com/applications/. (accessed: 10.05.2022).

[28] S. Steen (2014). *Compendium: Experimental Methods in Marine Hydrodynamics*. Department of Marine Technology, NTNU.

[29] O.M Faltinsen (1999). *Sea loads on ships and offshore structures*. Cambridge Ocean Technology series.

[30] B. Larsen (2022). 'Motion response analysis of a Sevan FWT moonpool foundation'. unpublished.

APPENDIX A

Experiment

A.1 Decay tests

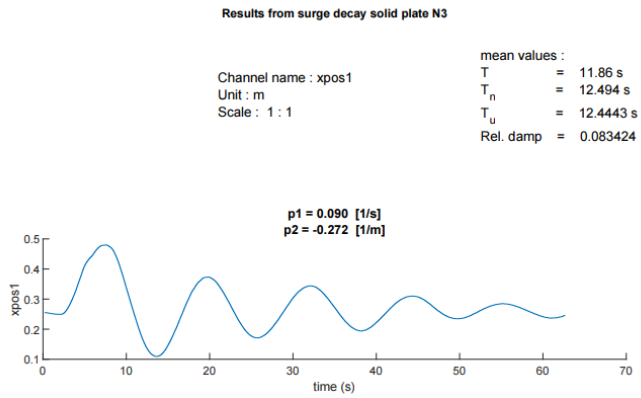

(a) Surge decay test - solid plate N3

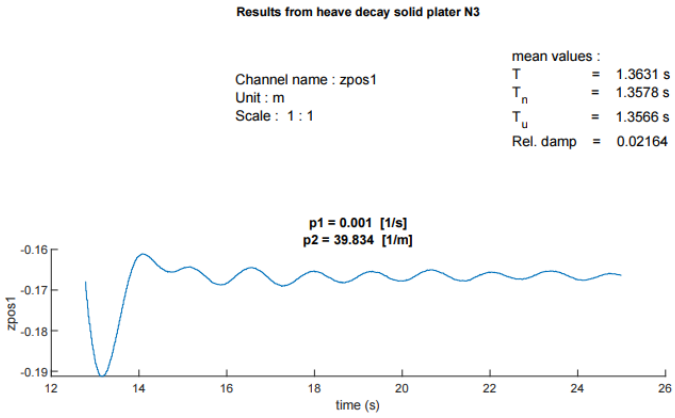

(b) Heave decay test - solid plate N3

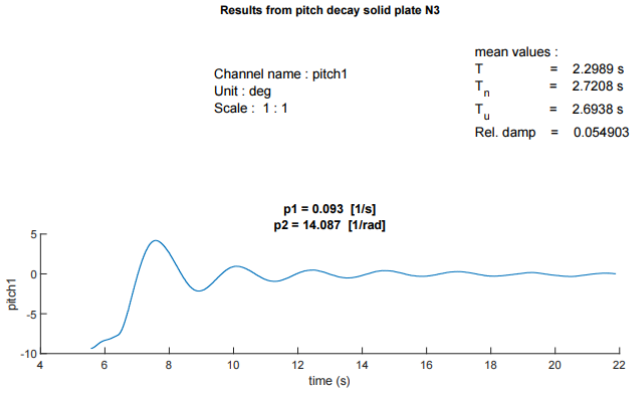

(c) Pitch decay test - solid plate N3

Figure A.1: Decay test results for surge (a), heave (b) and pitch (c) for the model with a solid plate at N3

A.2 Joint frequency table

Table 2.2. *Joint frequency of significant wave height and spectral peak period. Representative data for the northern North Sea*

Significant wave height (m) (upper limit of interval)	Spectral peak period (s)																			
	3	4	5	6	7	8	9	10	11	12	13	14	15	16	17	18	19	21	22	Sum
1	59	403	1061	1569	1634	1362	982	643	395	232	132	74	41	22	12	7	4	2	2	8636
2	9	212	1233	3223	5106	5814	5284	4102	2846	1821	1098	634	355	194	105	56	30	16	17	32 155
3	0	8	146	831	2295	3896	4707	4456	3531	2452	1543	901	497	263	135	67	33	16	15	25 792
4	0	0	6	85	481	1371	2406	2960	2796	2163	1437	849	458	231	110	50	22	10	7	15 442
5	0	0	0	4	57	315	898	1564	1879	1696	1228	748	398	191	84	35	13	5	3	9118
6	0	0	0	0	3	39	207	571	950	1069	885	575	309	142	58	21	7	2	1	4839
7	0	0	0	0	0	2	27	136	347	528	533	387	217	98	37	12	4	1	0	2329
8	0	0	0	0	0	0	2	20	88	197	261	226	138	64	23	7	2	0	0	1028
9	0	0	0	0	0	0	0	2	15	54	101	111	78	39	14	4	1	0	0	419
10	0	0	0	0	0	0	0	0	2	11	30	45	39	22	8	2	1	0	0	160
11	0	0	0	0	0	0	0	0	0	2	7	15	16	11	5	1	0	0	0	57
12	0	0	0	0	0	0	0	0	0	0	1	4	6	5	2	1	0	0	0	19
13	0	0	0	0	0	0	0	0	0	0	0	1	2	2	1	0	0	0	0	6
14	0	0	0	0	0	0	0	0	0	0	0	0	0	1	0	0	0	0	0	1
15	0	0	0	0	0	0	0	0	0	0	0	0	0	0	0	0	0	0	0	0
Sum	68	623	2446	5712	9576	12 799	14 513	14 454	12 849	10 225	7256	4570	2554	1285	594	263	117	52	45	100 001

Figure A.2: "*Joint frequency of significant wave height and spectral peak period, representative data for the northern North Sea* ", from page 31 in *Sea Loads on Ships and Offshore Structures* by O.M. Faltinsen [29]

A.3 Incident Wave measurements

WP3 and WP4

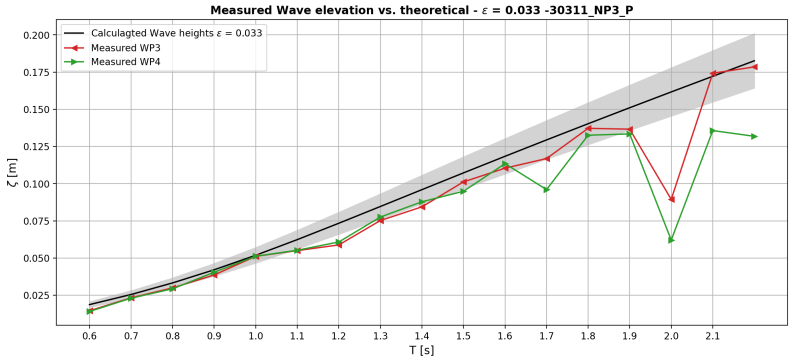

(a) WP3 & WP4, $\epsilon = 1/30, \Delta T = 0.1$

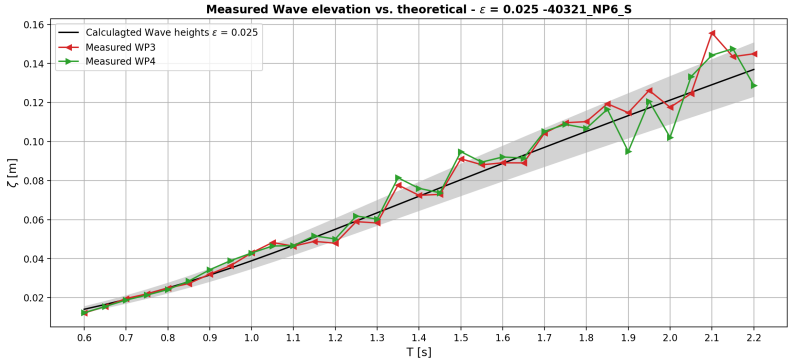

(b) WP3 & WP4, $\epsilon = 1/40, \Delta T = 0.05$

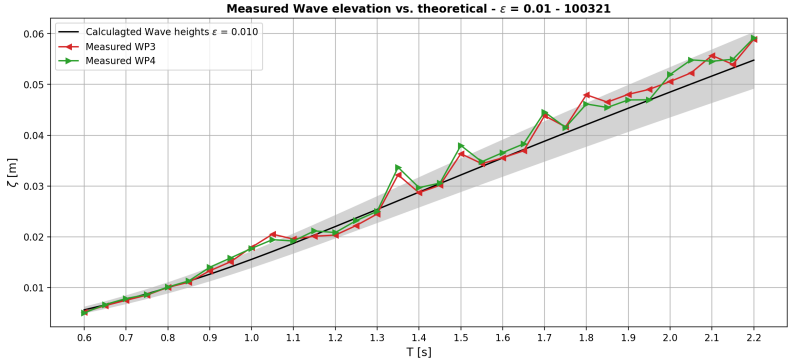

(c) WP3 & WP4, $\epsilon = 1/100 \Delta T = 0.05$

Figure A.3: Measured wave vs. theoretical from WP3 and WP4, resulting in the same trend as WP1 and WP2

WP1 and WP2

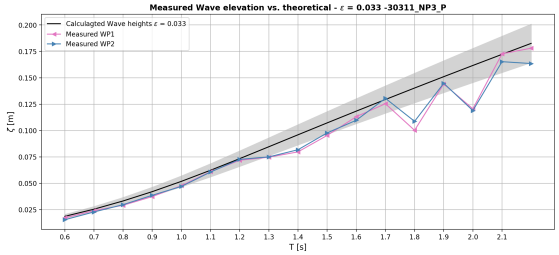

(a) N1

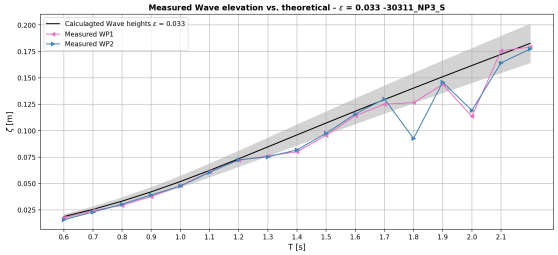

(b) N3

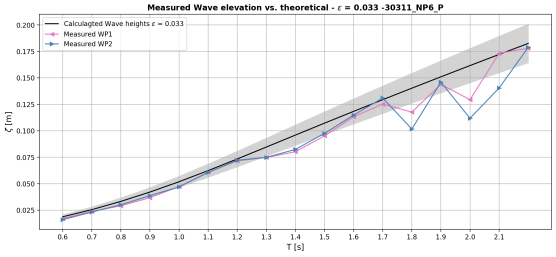

(c) N6

Figure A.4: Measured wave vs. theoretical from WP1 and WP2 for runs with $\epsilon = 1/30, \Delta T = 0.1$

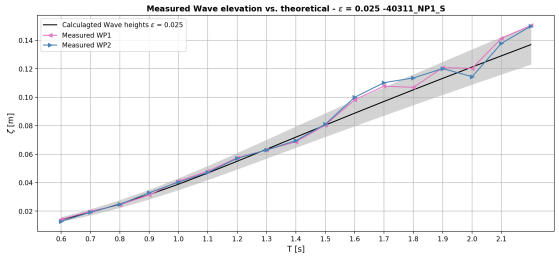

(a)

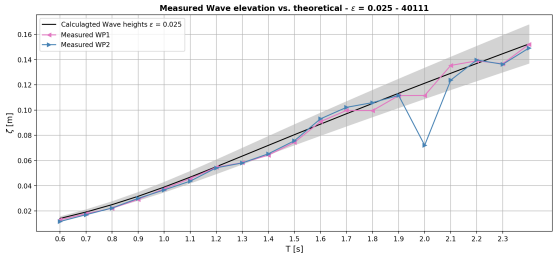

(b)

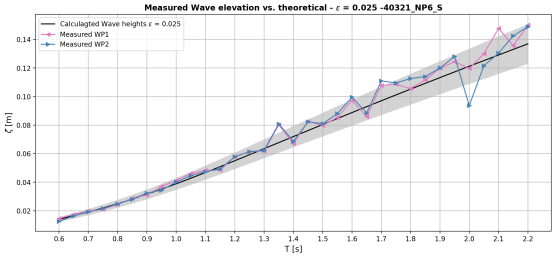

(c)

Figure A.5: Measured wave vs. theoretical WP1 and WP2 for several runs with $\epsilon = 1/40, \Delta T = 0.1/0.05$

A.4 Time series

Filtered time windows and steady state

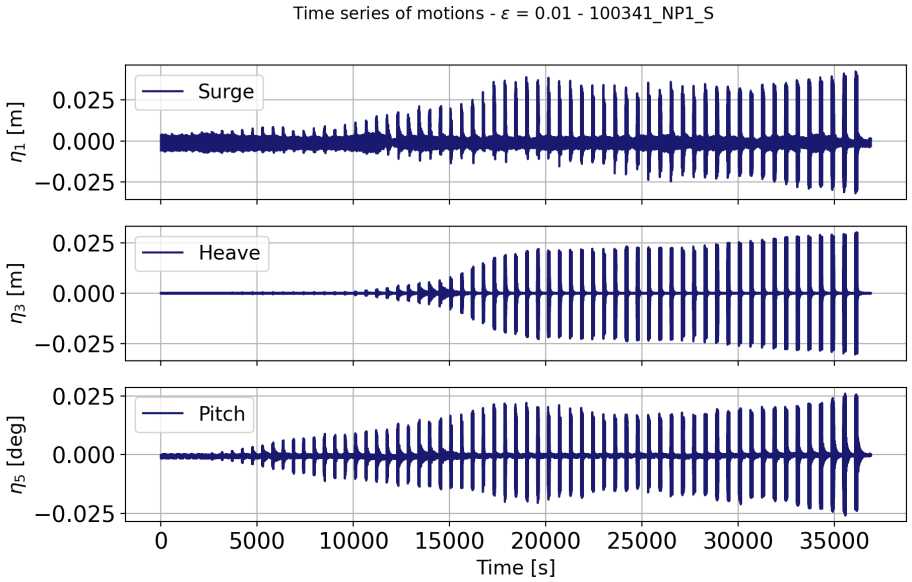

(a) $\epsilon = 1/100, \Delta t = 0.025$

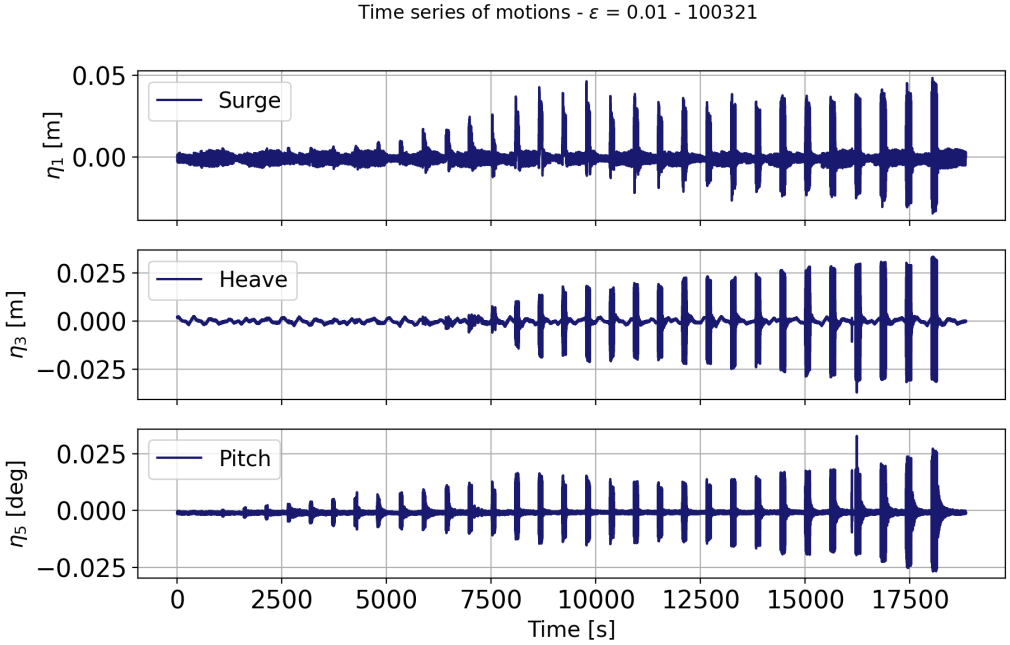

(b) $\epsilon = 1/100, \Delta t = 0.05$

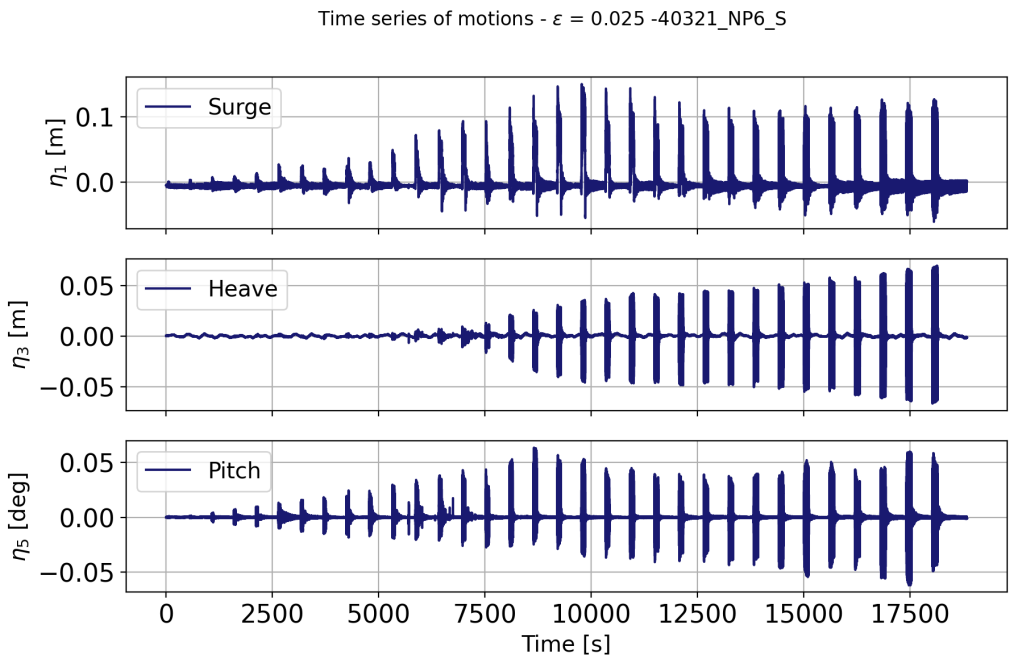

(a) $\epsilon = 1/40, \Delta t = 0.05$

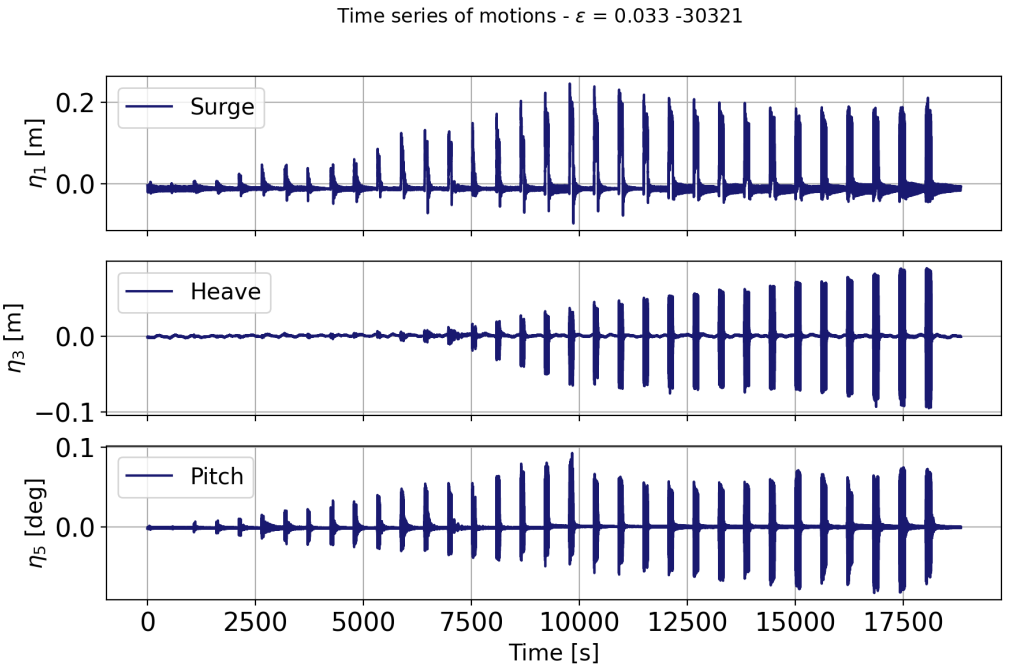

(b) $\epsilon = 1/30, \Delta t = 0.05$

APPENDIX B

Additional results

B.1 RAOS

Surge: plates at N1, N3 and N6

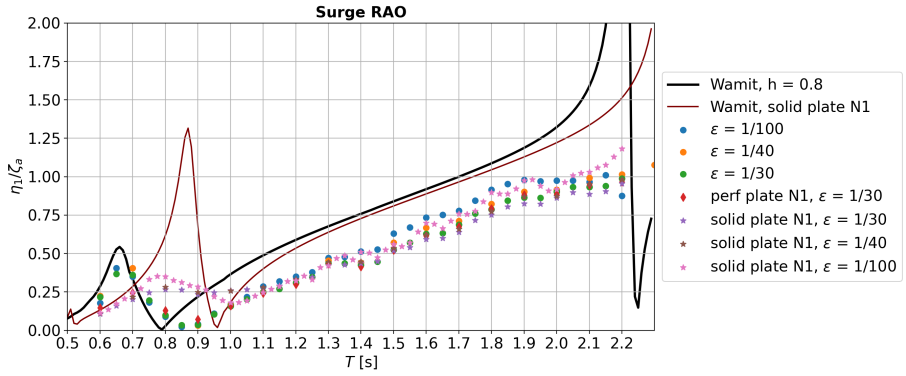

(a) N1

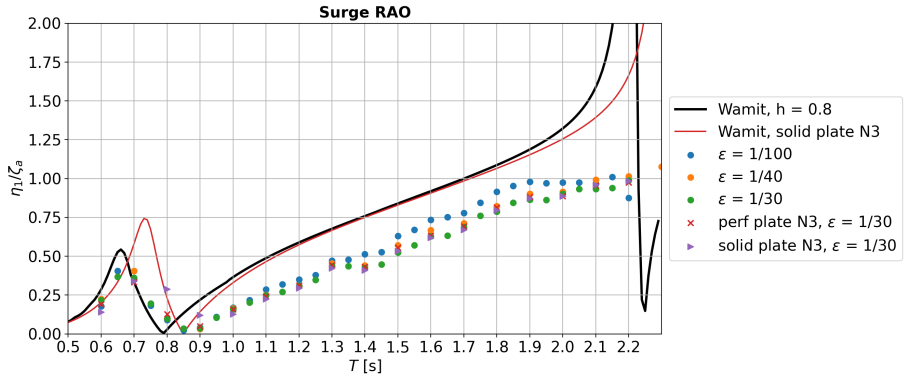

(b) N3

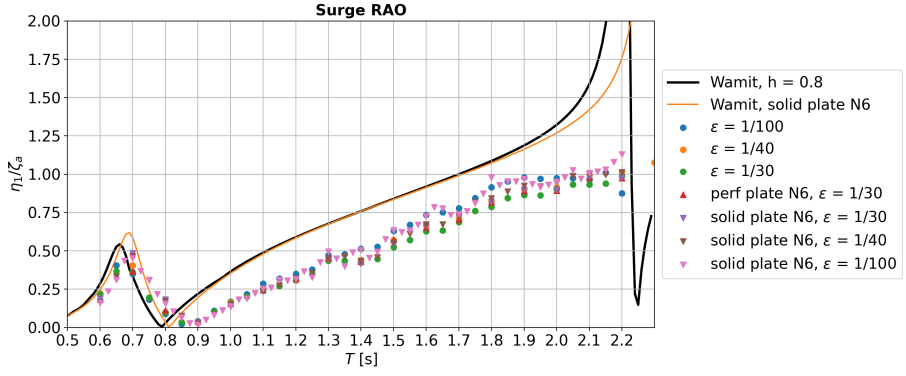

(c) N6

Figure B.1

Heave: plates at N1, N3 and N6

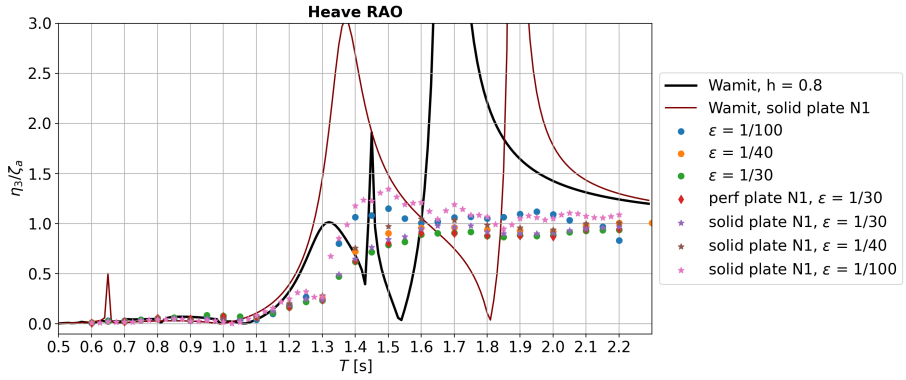

(a) N1

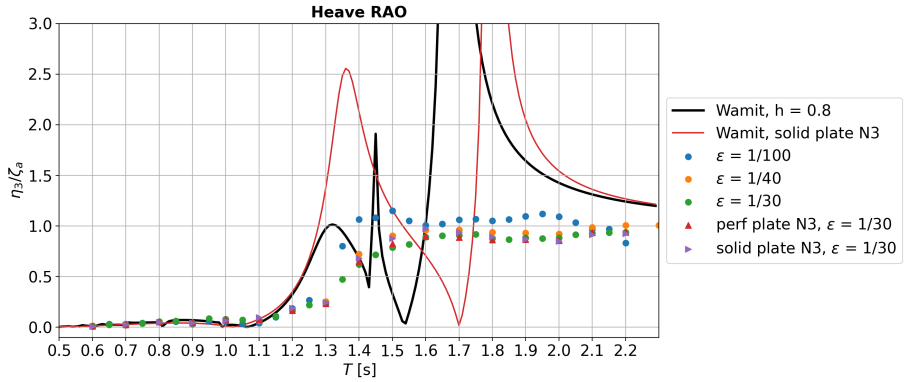

(b) N3

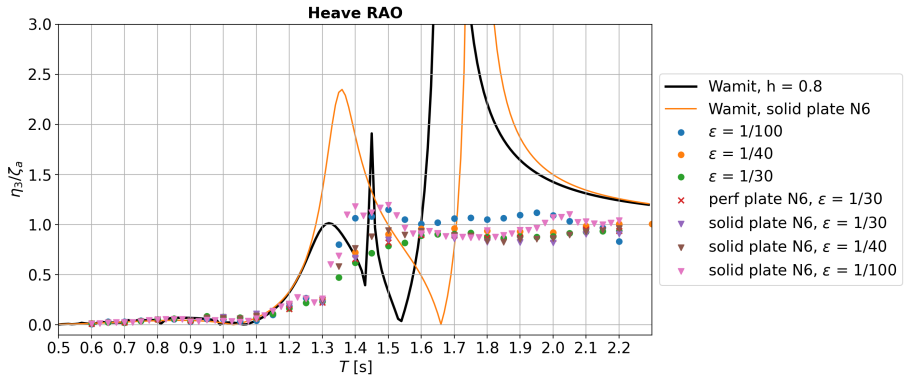

(c) N6

Figure B.2

Pitch, plates at N1, N3 and N6

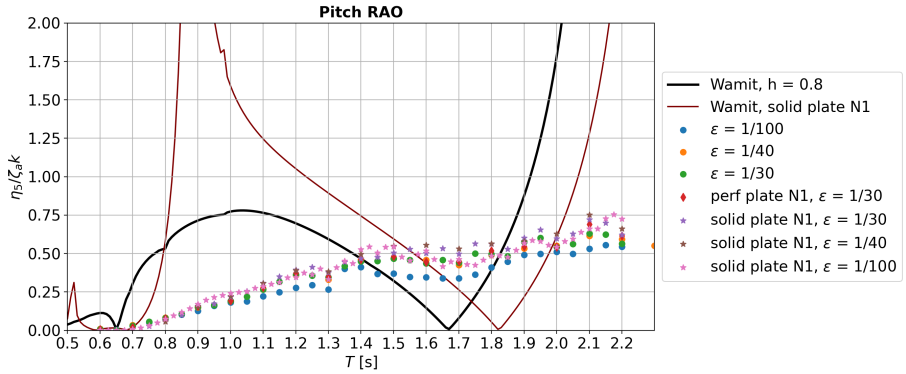

(a) N1

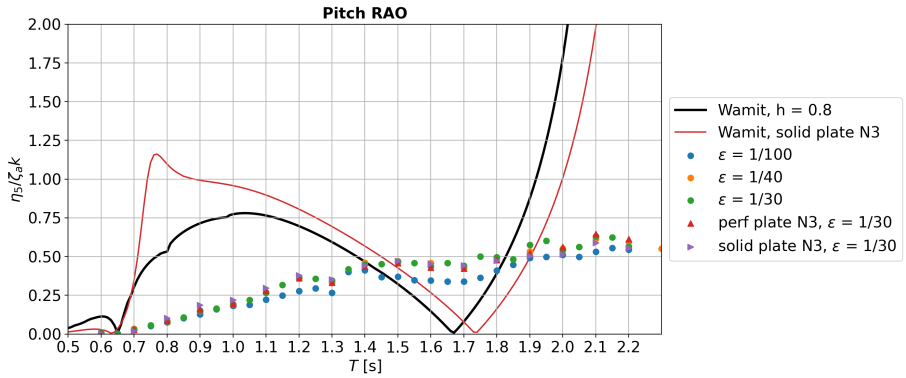

(b) N1

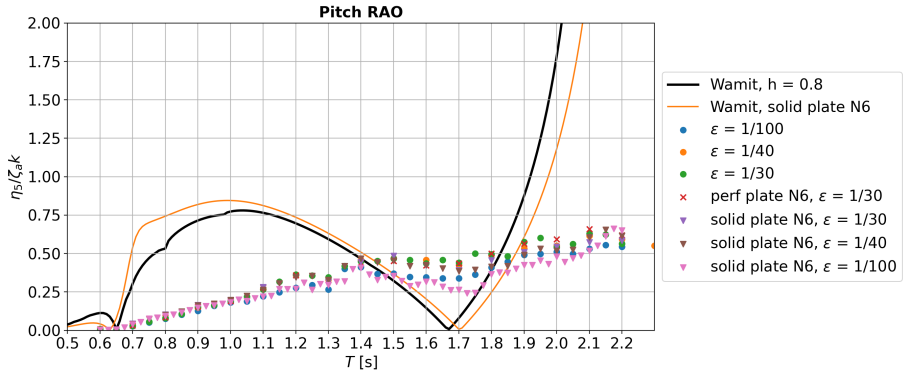

(c) N6

Figure B.3

B.2 Free surface elevation

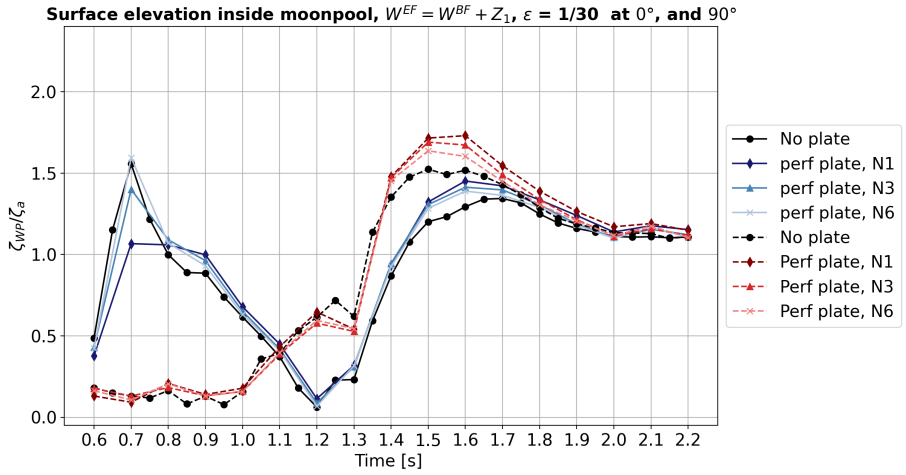

(a)

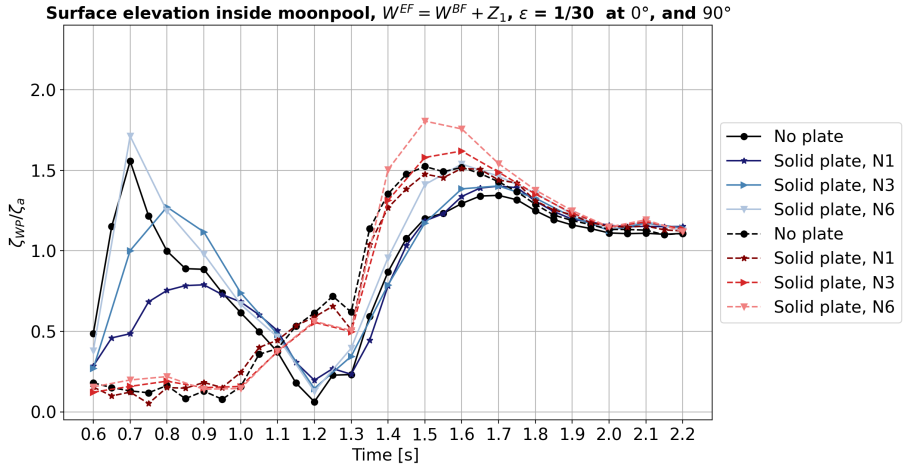

(b)

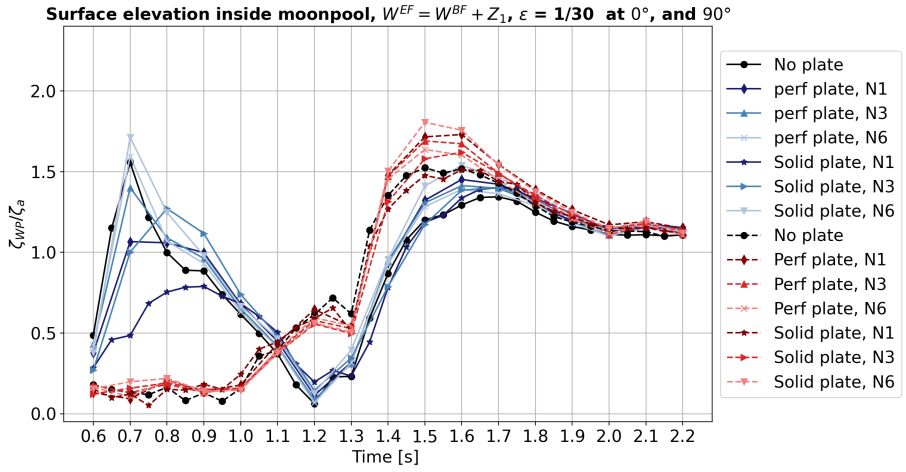

(c)

Figure B.4: Free surface elevation from measurements at 0$*degree* and 90° with (a) perforated plates, (b) solid plates and (c) with both the baffle types, for $\epsilon = 1/30$

APPENDIX C

Irregular wave results

C.1 Transfer functions

Hs = 0.04, Tp = 0.8

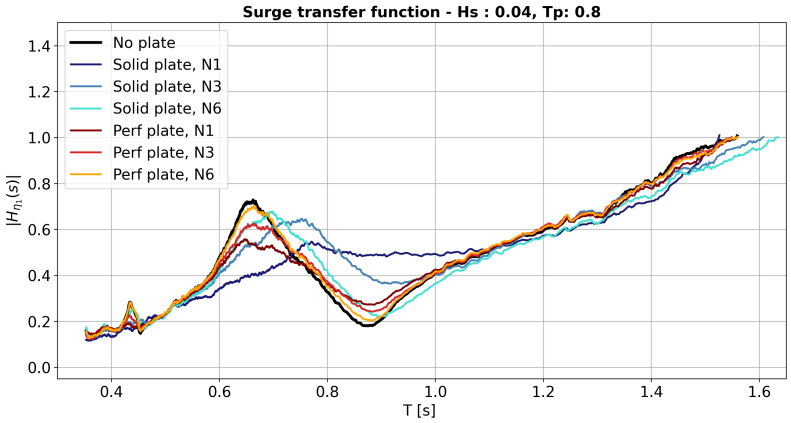

(a) $|H_{\eta 1}(s)|$

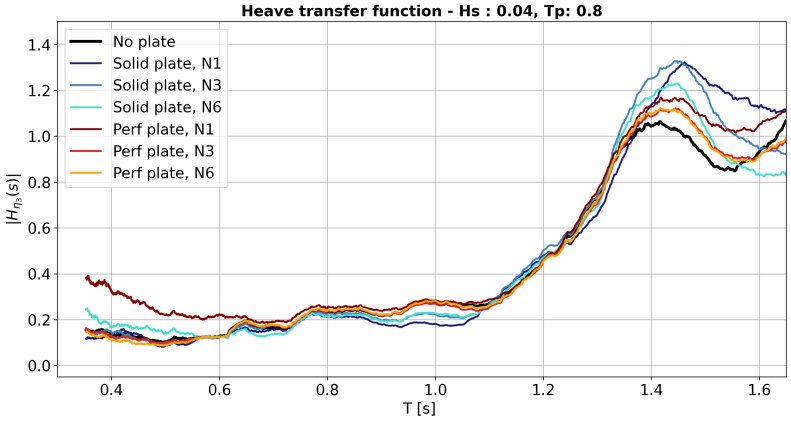

(b) $|H_{\eta 3}(s)|$

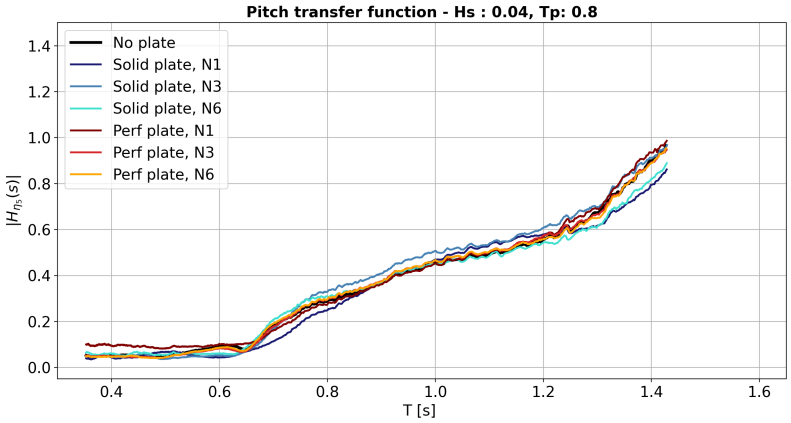

(c) $|H_{\eta 5}(s)|$

Figure C.1

Hs = 0.05, Tp = 1.0

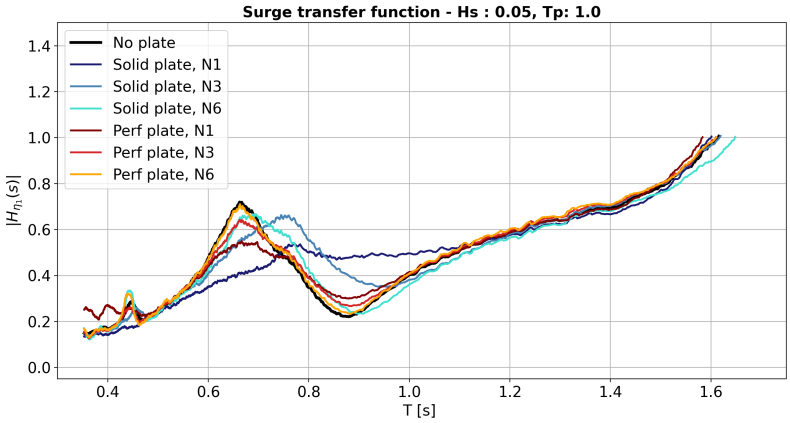

(a) $|H_{\eta 1}(s)|$

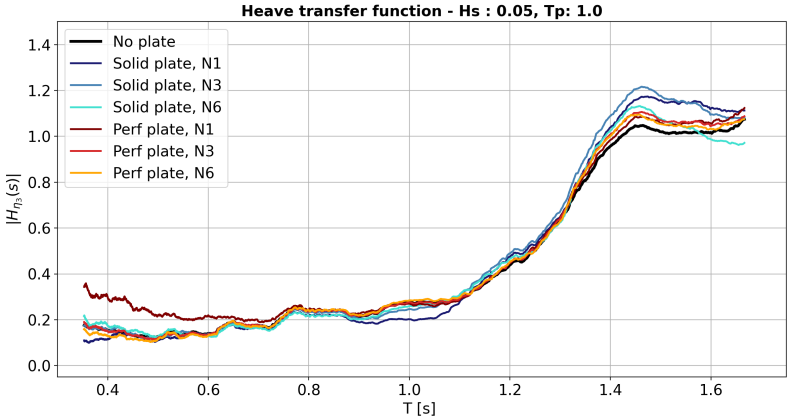

(b) $|H_{\eta 3}(s)|$

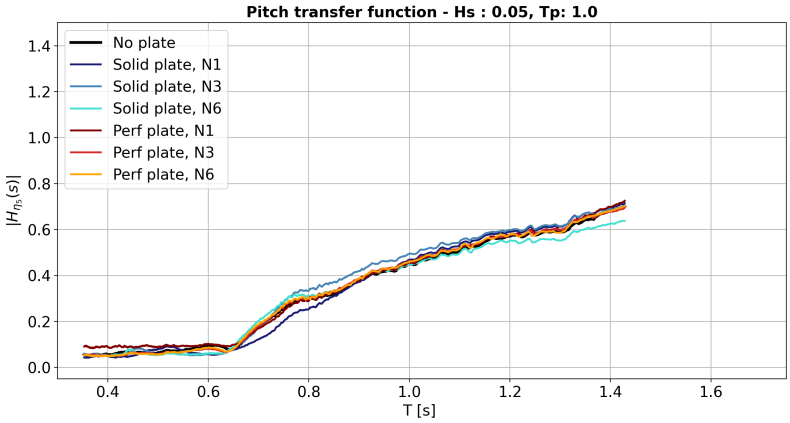

(c) $|H_{\eta 5}(s)|$

Figure C.2

Hs = 0.06, Tp = 1.2

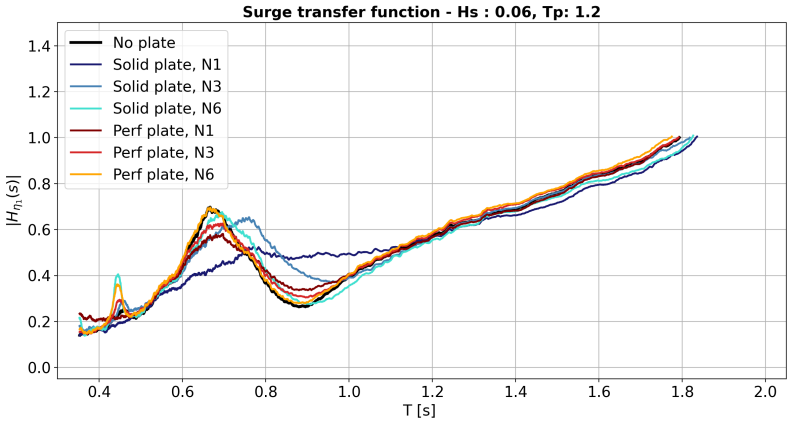

(a) $|H_{\eta 1}(s)|$

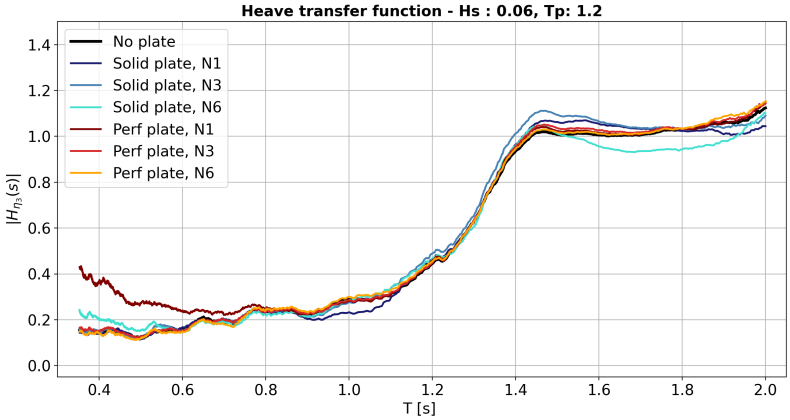

(b) $|H_{\eta 3}(s)|$

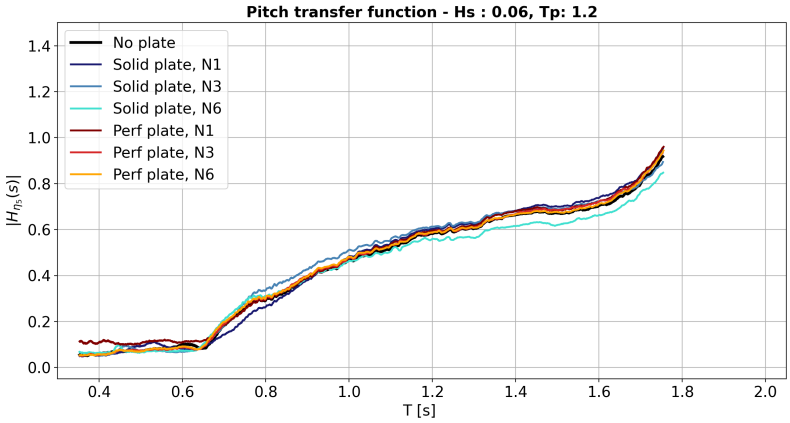

(c) $|H_{\eta 5}(s)|$

Figure C.3: Surge, heave and pitch RAOs for a sea state with

Sofie Helene Råen Wettre

Numerical and experimental investigation of a floating wind turbine foundation

NTNU
Norwegian University of
Science and Technology